INDOEX:

Chemistry of the Indian Ocean atmosphere

Jos de Laat

Cover: © Meteosat-5 image (Visual channel), 14 December 1999, 06:00 UTC.

A tropical cyclone halfway through December is a very rare sight over the northern Arabian Sea. Statistics show that it occurred only once between 1945-1997.

Printed by Ipskamp PrintPartners, Enschede

ISBN 90-393-2572-3

INDOEX

Chemistry of the Indian Ocean atmosphere

INDOEX

Chemie van de Indische Oceaan atmosfeer

(MET EEN SAMENVATTING IN HET NEDERLANDS)

TER VERKRIJGING VAN DE GRAAD VAN DOCTOR AAN DE UNIVERSITEIT UTRECHT, OP GEZAG VAN DE RECTOR MAGNIFICUS PROF. DR. H. O. VOORMA, INGEVOLGE HET BESLUIT VAN HET COLLEGE VOOR PROMOTIES IN HET OPENBAAR TE VERDEDIGEN OP MAANDAG 20 NOVEMBER 2000 DES NAMIDDAGS TE 2:30.

DOOR

Adrianus Theodorus Joseph de Laat

Geboren op 26 juli 1973 te 's Hertogenbosch

Promotor: Prof. Dr. Jos Lelieveld

Faculteit Natuur en Sterrenkunde

The work presented in this dissertation was supported by the Netherlands Earth and Life Science Foundation (ALW) with financial aid from the Netherlands Organization for Scientific Research (NOW).

CONTENTS

Chapter 1

Preface

A main aspect of this thesis involves measurements of atmospheric trace gases over the Indian Ocean. These measurements were performed during the INDian Ocean EXperiment (INDOEX). This was a large observational campaign to address several important issues in atmospheric sciences. The main activities during INDOEX involved measurements of the atmospheric chemical composition, the level of pollution and the properties of small atmospheric particles (aerosols). One specific reason for performing this experiment over the Indian Ocean was that the circulation during the northern hemispheric winter is that it provides excellent conditions for performing these measurements. Pollution and aerosols are abundant over the northern Indian Ocean during this period, and few factors that "complicate" the meteorology, like clouds and convection, are present. An additional benefit of the campaign was that much information was gained about the meteorological processes that play a role in the winter monsoon circulation. Before INDOEX, meteorological studies mostly focussed on the summer monsoon.

A main goal of this thesis is to analyze the INDOEX measurements by means of a global chemistry-climate model. By the so-called "nudging" technique, the model was forced to follow the observed meteorological state of the atmosphere. This enables a detailed observation-model comparison. Such a comparison provides information about the model performance, i.e. how well the model reproduces the observed meteorology and atmospheric chemistry. This is important for the understanding and interpretation of future climate studies based on emission scenarios. In this thesis we will focus mainly on observations of ozone (O_3), carbon monoxide (CO), acetone (CH_3COCH_3) and acetonitrile (CH_3CN). The trace gases O_3 and CO play a key role in the chemistry of the troposphere, whereas acetone and acetonitrile are important tracers for emissions and chemical processes. The observations were performed from three platforms: a Dutch Cessna-Citation aircraft, the American research vessels Malcolm Baldrige and Ronald Brown, and the climate observatory at Kaashidhoo-island on the Maldives. In the introduction we will explain INDOEX, the winter monsoon circulation, the model we used and the nudging technique. Chapters 2-5 consist of observation-model comparisons and interpretation, and in chapter 6 we will also look at the large-scale circulation and how it affects pollution transport. The thesis will end with a summary and final discussion in chapter 7.

Chapter 1

Introduction

1.1 INDOEX

During the last decades, there has been a large increase of the scientific and public interest in atmospheric chemistry. This increasing interest is closely related to topics such as the discovery of the ozone hole, the problems associated with smog-episodes in urban regions, the harmful effects of acid rain and the enhanced greenhouse effect and global warming. Human activity is largely responsible for the aforementioned problems. There is no doubt that human activity affects the global chemical composition of the atmosphere. Changes in the chemical composition of the atmosphere are accompanied by changes in the radiation and energy budgets of our atmosphere. Therefore, human activity also changes earth's climate.

One important issue in atmospheric sciences is to what extent changes in the atmospheric chemical composition affect global climate, and more specific, which atmospheric processes cause warming or cooling of the earth's atmosphere. Increasing atmospheric mixing ratios of trace gases like carbon dioxide (CO_2), ozone (O_3) and methane (CH_4) cause global warming. On the other hand, small particles (aerosols) can cool the atmosphere because they reflect sunlight (the so-called "direct climate effect"). These effects also depend on the extent to which aerosols absorb solar radiation (e.g. soot). Aerosols also affect cloud properties, like the average droplet size and the total amount of droplets, possibly causing additional cooling of the atmosphere ("indirect climate effect"). Since both (human made) emissions of greenhouse gases and aerosols are closely related, global warming by greenhouse gases may partly be counteracted by the cooling effect of aerosols. However, the magnitude of the cooling by aerosols is highly uncertain, therefore causing a large uncertainty in climate studies. Moreover, the formation, removal and transport of aerosols and greenhouse gases and their effects on clouds are linked, and our knowledge about the interaction of these different processes is still limited.

Figure 1.1 is an attempt to visualize the main interactions between different processes in the earth's climate. Although still a simplification, the figure illustrates how, by changing one process in this framework, all other processes will indirectly be affected. There exist numerous "pathways" that link different climate processes. How the interactions between different processes work is not completely understood.

To better understand the effects of changes in the chemical composition of the atmosphere on climate we not only need to know which atmospheric compounds cause warming or cooling, we also need to know where those compounds are "made", and how they are distributed around the globe. Emissions of greenhouse gases and aerosols do not occur uniformly around the globe, but have a high spatial and temporal variability. Transport processes redistribute the pollution around the globe, so that emissions of pollution not only affect the chemical composition of the atmosphere close to the sources, but also remote from the source regions. How the global chemical composition of the

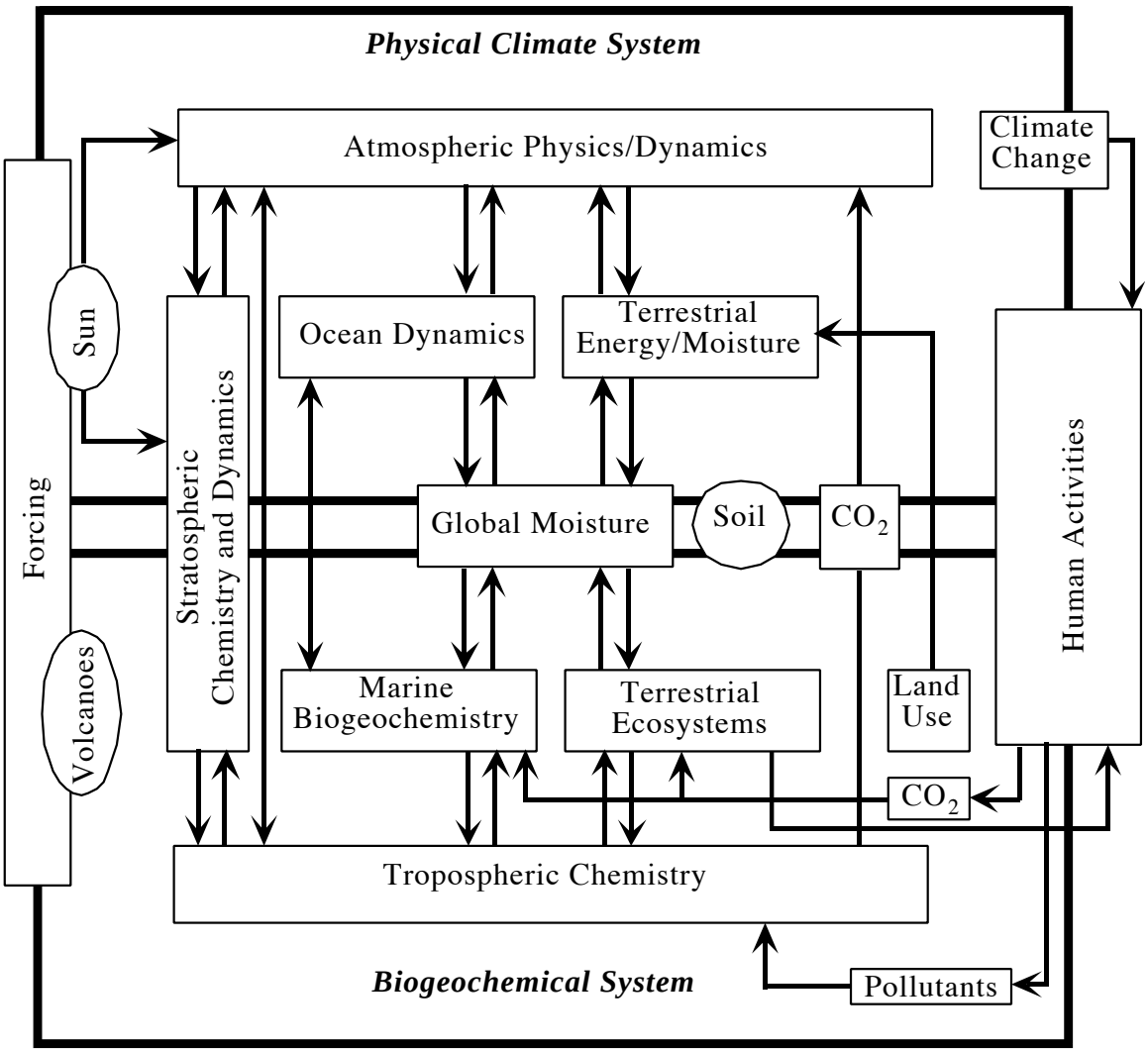

Figure 1.1 Diagram showing the important interactions amont different components of the Earth system with emphasis on the phsical climate and biogeochemical cycles. After Brasseur et al, [1995, Figure 1.4]

atmosphere is precisely affected by local emissions is still uncertain. The most important source regions of human made emissions were, until recently, Europe, Northern America, China and Japan. Pollutants emitted in these regions remain mostly in the northern hemisphere. Therefore, the southern hemisphere remained a fairly clean environment. The recognition of the potential dangers of pollution has recently led to political actions to decrease emissions in Europe, Northern America and eastern Asia. At the same time, there has been a large increase in pollutant emissions from developing countries, especially India and South East Asia. This has led to a current situation where the amount of pollution in the developing regions is comparable to those over Europe, North America and eastern Asia. As it is expected that the developing countries continue to expand their economic activities, it can also be expected that their pollutant emissions

will continue to increase. The developing countries in Asia are located close to the equator, increasing the possibility that a substantial amount of pollution from those regions might reach the southern hemisphere. However, at the moment the knowledge about the amount of pollutants from India and South East Asia reaching the southern hemisphere is limited. In general our knowledge about cross-hemispheric transport, as well as the global redistribution of pollution, is limited. To increase our knowledge about the direct and indirect aerosol cooling effect and the transport of south east Asian pollution, INDOEX has been established. During the Indian winter monsoon period (Nov-Apr) pollutants and aerosols are transported from the continent to the tropical Indian Ocean. Because of the meteorological conditions in this region during this time of the year (see paragraph 1.2), few complicating factors like clouds and convection are present over the northern Indian Ocean. This makes the northern Indian Ocean during the winter monsoon an "*excellent natural laboratory to perform combined chemistry and climate studies*" [J. Lelieveld, 1997, after V. Ramanathan and P. Crutzen].

In a cooperation between American, European and Indian scientists, a large number of atmospheric observations were performed between 1995 and 1999 over the Indian Ocean, with an emphasis on aerosols and atmospheric trace gases. The measurements were performed from different platforms (ships, aircrafts, satellites and surface stations).

From 1995 to 1998 pre-INDOEX campaigns were performed to obtain preliminary information about processes occurring over the Indian Ocean. With the use of these measurements the organization of the major campaign (the Intensive Field Phase, IFP) could be supported and adjusted. The IFP took place in February and March 1999, with the central coordination of the campaign situated in the Maldives, on the airport Island Hulule, close to Male, the capital of the Maldives. At the peak of the activities more than 150 scientist were present on the Maldives.

An additional benefit of INDOEX was that it increased our knowledge about the meteorological processes over the Indian Ocean, which until that moment was rather limited. Historically there has not been much interest for this season, because the impact on the hydrology, agriculture and life in general in southern Asian is much more strongly influence by the wet summer monsoon. Additionally, the Indian Ocean is a region with only a few observational sites. Our knowledge about the temporal and spatial variability of the Indian Ocean region during this period was rather limited, apart from the general circulation pattern.

1.2 The Indian winter monsoon

The Indian Ocean is the smallest of the three big oceans of our world. The ocean is bordered at three sides by landmasses. To the west lies Africa, to the north Asia and at the eastern rim Indonesia and Australia. The southern part of the Indian Ocean is connected to the Atlantic and Pacific Oceans. The weather over the Indian Ocean is dominated by the monsoon circulation. During the course of a year, strong convection shifts between India and Australia, following the annual cycle of maximum solar radiation and the heating of land surfaces. The monsoon seasons over India and Australia are characterized by a long dry season and a short wet season, with the wet season occurring during the

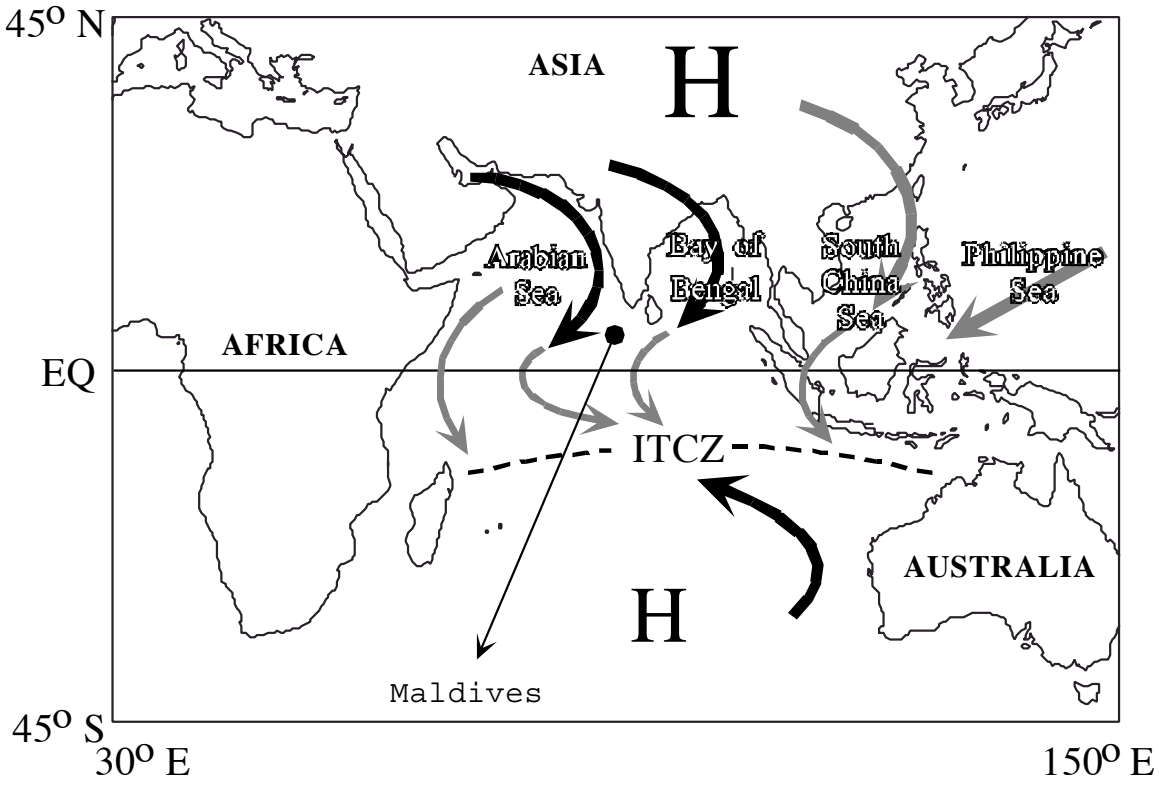

Figure 1.2 Schematic overview of the winter monsoon circulation over the Indian Ocean

(local) summer period. The countries between India and Australia mostly have two wet seasons, one when the convection moves toward India and one when it moves towards Australia, although rainfall can occur during the entire year.

The dry season over India (the northeast monsoon or the Indian winter monsoon; note that in India the term "monsoon" is mainly used for the wet summer season) begins when the summer monsoon convection, covering almost the entire Indian subcontinent, withdraws towards the south [Hastenrath, 1985; Martyn, 1987]. The withdrawal starts in northern India in September [Ramage, 1971]. By the end of December, most of the convection over India has vanished, with the exception of the southern tip of India. The start of the dry season is closely related to the buildup of high pressure over central Asia. During boreal autumn, when the solar intensity decreases, the temperatures drop and snow cover starts to build up over Siberia. The snow cover causes additional radiative cooling, temperatures drop even further and surface pressure increases. At the same time the monsoon convection moves south towards the equatorial Indian Ocean, following the maximum in the intensity of the solar radiation. The deep convection causes near surface advection of air masses from the surrounding areas towards the convective areas. Thus, the continental outflow due to the continental high pressure area, in combination with the advection of air masses towards the convection, causes a northeasterly flow over the northern Indian Ocean (Figure 1.2). From January to March the deep convection areas (Interhemispheric Tropical Convergence Zone, ITCZ) over the Indian Ocean can be

located as far south as 15°-20° S.

Meteorological analyses show that the northeasterly flow is rather shallow, extending not higher than 700 hPa (~ 3 km) [McGregor and Nieuwolt, 1998]. This is caused by the large-scale subsidence from the Asian high-pressure area. The subsidence area covers southern Asia and the northern Indian Ocean. A strong temperature inversion is formed at the top of the boundary layer, suppressing the formation of deep convection. In addition, the continental air masses, advected by the northeasterlies toward the Indian Ocean, are very dry during the boreal winter. Hence, very few boundary layer clouds are formed, and therefore large parts of the northern Indian Ocean are devoid of clouds during the winter monsoon period. Clouds are only formed far away from the continent, where the northeasterly flow has picked up enough moisture from the oceans to form cumulus clouds, or in the vicinity of synoptic disturbances that occasionally migrate in an east-west direction north of the equator over the Indian Ocean.

Because India and South East Asia are strong source regions of pollutants, the air masses in the northeasterly flow are very polluted. There is little exchange of air masses between the boundary layer and the free troposphere, and there are few perturbing factors like convection and clouds. Therefore, changes in the chemical composition of the air masses during the transport from the continent to the convection at the ITCZ will be mainly caused by gas-phase photochemistry and deposition. At the ITCZ the polluted northern hemispheric airmasses are mixed with clean southern hemispheric airmasses, and the air is redistributed vertically by the convection. In the outflow regions of the convection at high altitudes the air masses may be distributed toward both hemispheres.

1.3 Chemistry in the INDOEX region.

India and South East Asia are densely populated areas. The presence of so many people is inevitably accompanied by air pollution. Many of the people in the Indian region still live in rural locations where domestic energy consumption largely depends on biofuels such as wood cow dung, whereas in urban areas soft coke, kerosene and other liquid fuels are used, too [Smith *et al.*, 2000]. The increasing development of these regions, accompanied by an increasing demand for power and electricity, as well as an increased use of cars, will cause even higher amounts of pollution. Currently, about one quarter of the energy use depends on biofuels in Asia, whereas in India this fraction is even larger, close to 50% [Streets and Waldhoff, 1998].

A difficulty in estimating biomass burning emissions is that it usually occurs scattered over large rural areas. Moreover, the burning process is not well defined because the fuel type and the combustion phase (flaming, smoldering) strongly affect the smoke composition. It has been estimated that in India firewood contributes approximately two thirds to biofuel consumption, while the burning of dung and agricultural wastes contribute roughly equally to the remaining one third [Sinha *et al.*, 1998; Mahapatra and Mitchell, 1999].

The type of species being emitted by combustion processes is very much dependent on the temperature. At higher temperatures more fuel will be directly converted into Carbon

dioxide (CO_2), while at lower temperatures more carbon monoxide (CO) and other relatively incompletely burned products, will be emitted. Domestic burning takes place at low temperatures, and because it is the main source of pollution over India, it can be expected that CO concentrations are high in Indian air masses. In addition, species that are typical for biomass burning are abundant in Indian air masses. Examples of such species are acetone (CH_3COCH_3), acetonitrile (CH_3CN), methylchloride (CH_3Cl) and potassium (K), although methylchloride and especially acetone have other sources as well.

Although the INDOEX measurements showed that pollution levels over the entire northern Indian Ocean basin were high, photochemical O_3 buildup nevertheless appeared to be limited. The measurements show that ozone levels were only moderately enhanced at greater distance from the Indian coast. As discussed above, most of the gaseous pollutants originated from biomass burning. In particular smoldering fires produce relatively little NO_x, a necessary ingredient for photochemical O_3 formation ($NO_x = NO + NO_2$). Importantly, NO_x is rapidly converted into nitrate (< 1 day) by nighttime heterogeneous reactions on aerosols, and daytime reaction with hydroxyl (OH) radicals, followed by deposition or uptake of HNO_3 by sea salt and dust particles. As a result, NO_x mixing ratios were generally quite low in the marine boundary layer (ECHAM: < 10 pptv, De Laat *et al.* [1999]; Measurements: < 40 pptv (detection limit), Rhoads *et al.* [1997]), favoring chemical O_3 destruction rather than O_3 formation.

Pollutants are transported from the continent to the Indian Ocean. Over the oceans pollutants can be removed from the atmosphere because they dissolve in the seawater and/or they are photochemically destroyed. The hydroxyl radical causes most of the photochemical destruction, and it reacts with many atmospheric pollutants. Species that are not removed by OH generally have a long atmospheric lifetime and can sometimes be removed at higher altitudes (i.e. in the stratosphere), where more energetic shortwave radiation is present than in the troposphere, hence causing photodissociation of those species.

1.4 The European Centre HAmburg Model (ECHAM)

1.4.1 Climate models

The evolution of the atmosphere in space and time can be described by a set of mathematical equations ("primitive equations", see Appendix). These equations are the horizontal and vertical equation of motion, the thermodynamic and moisture equations. They describe how winds, temperature and moisture depend on and interact with each other. Although the derivation of the equations is rather straightforward, solving them in three dimensions turns out to be extremely difficult. However, it is possible, under a number of assumptions, to approximate the equations as a set of algebraic difference equations that can be solved numerically with the use of computers.

The numerical model can be used in different ways. If sufficient observations of the current atmosphere are available, an initial state can be defined that can be used as a starting point for the model to calculate the future development of the atmosphere, resulting in a weather prediction. In principle a prediction can be calculated for any

period of time, but the period for which the prediction is reliable is limited because of a number of reasons. The current state of the atmosphere is not exactly known due to errors in observations, and the lack of observations in certain areas around the globe. Additionally, the model itself is only a simplification of the "real" atmosphere. Certain atmospheric processes are described in a simplified way in the model, resulting in deviations from the "real" state of the atmosphere. The errors and deviations will grow during a model simulation due to the chaotic nature of the atmosphere. Eventually, the modeled state of the atmosphere will be completely different from the "real" state of the atmosphere. Therefore, weather predictions for periods longer than 1-2 weeks are unreliable. However, although the predictions eventually become unreliable as weather predictions, the simulated atmosphere is by no means wrong. For a longer period of time the model will, on average and by approximation, simulate the correct atmospheric behavior. Thus, the "long-term prediction" can provide, on average, information about the possible future atmospheric developments.

For the numerical solution of the primitive equations the atmosphere is divided into grid cells at different vertical levels. For every grid cell the development of the atmosphere can be calculated based on the simulated atmosphere of the previous time step. The actual grid size can be chosen freely, although at very high resolution the approximation of the primitive equations is not completely valid anymore. The model timestep is dependent on the grid size; the smaller the grid size, the shorter the timestep. Thus, at higher resolution the number of grids and timesteps increases and increased computational resources are needed for a simulation. Therefore, the availability of computational resources limits the resolution at which the simulation can be performed. A climate model often will perform simulations for many years, so that the grid size must be larger than for a weather prediction model, typically simulating the weather for a few days ahead.

The numerical model also needs a number of boundary conditions at the surface. In the case of orography, sea surface temperatures, sea-ice cover, surface roughness, vegetation types and the surface albedo, simple databases are sufficient. Processes like the exchange of heat, moisture and momentum between the surface and the atmosphere are much more complex. Simple descriptions of these processes will not be sufficient (i.e. they will cause large errors), hence a more complex description of these processes is required. In models such a description is called a parameterization. Parameterizations can be considered as process approximations within the climate model, describing the more complex processes based on available parameters. For example, to describe surface exchange processes a 5-layer soil model is included in the ECHAM model, describing the moisture and temperature changes within the soil. Other parameterizations describe how solar radiation is transferred into heat at the surface, or how moisture evaporates into the atmosphere.

Parameterizations are not only used for surface processes. There exist a number of atmospheric processes that are important for the changes in the large scale atmospheric circulation, but are not represented by the numerical model, because they take place on scales smaller than the model grid size (sub-grid scale). Examples of such processes are atmospheric turbulence, convection, radiation and microphysics. For example, cloud sizes range from a few hundred meters to several hundreds of kilometers, whereas individual cloud and raindrops are even much smaller. A typical model resolution for a

climate model is 200 to 400 kilometers. The model cannot reproduce single clouds. However, clouds have an impact on the atmosphere because they scatter sunlight, absorb infrared radiation, cause vertical motions in the atmosphere and produce precipitation. To account for these processes, it is calculated on average how many clouds are approximately present within a grid box, how much sunlight they reflect and how much precipitation they produce. The impact is calculated using the modeled winds, temperature and moisture. Moreover, the extent to which cloud processes within the gridbox depend on the average variables of the grid box is often calculated based on simplified physical processes or on statistics based on large numbers of observations. Parameterizations are generally recognized as a limiting factor in climate studies and lead to misrepresentations of atmospheric processes and eventually to errors. This is one of the main reasons why weather predictions for several days ahead are less reliable, and why different climate models yield different future climate scenarios.

1.4.2 Global atmospheric chemistry models.

Over the last few decades our knowledge about atmospheric processes, including atmospheric chemistry, has increased significantly. This is partly the result of the development and the use of numerical models. The philosophy behind the use of numerical models is the following:

> "*Although we can study individual system interactions in detail by laboratory simulations or, under favorable conditions, directly in nature, because of the many possible combinations of system processes, we must use numerical mathematical models when we try to comprehend system behavior as a whole*." [Graedel and Crutzen, 1993].

Numerical models have become a widespread tool in atmospheric sciences to help improve our knowledge about atmospheric processes, to analyze observations and to simulate future scenarios. In atmospheric chemistry a wide variety of numerical models are currently used. They vary from the relatively simple (0-dimensional) box models, used for process studies, to the highly complex 3-dimensional (3-D) global models that simulate the entire atmosphere. For the 3-D global models two types can be distinguished: (global) chemistry general circulation models (GCM) and chemical transport models (CTM). A CTM uses calculated winds, temperature, water vapor and cloud distributions from a weather forecast model as input variables for a 3-D chemistry model. The advantage of this approach is that it simplifies the calculations, allowing more time and computer storage for chemical calculations. An additional benefit is that, if measurements for the modeled period are available, comparisons between the measurements and model results can be made. One disadvantage of CTMs is that only emission, transport and removal process of trace species can be studied. Studying several feedbacks between atmospheric chemistry and other atmospheric processes is not possible (for example, tropospheric O_3 affects the radiation budget). Another disadvantage is that the limited availability of meteorological analyses, typically every 6 hours, restricts the possibility of doing model studies of processes that take place

on shorter time scales. A GCM, on the other hand, calculates its own meteorology. The availability of all kinds of meteorological parameters during each model time step enables a direct two-way coupling between atmospheric physics and atmospheric chemistry. A GCM can simulate possible future and past climates, or perform sensitivity studies of future climates. It is also possible to perform model studies of processes that take place on time scales shorter than the 6 hours from the meteorological analyses.

Disadvantages of GCMs are that they require more computational resources, and that the comparison of model output with observations is not as straightforward as with a CTM. As explained in section 1.4.1, the simulated atmosphere deviates from the actual atmosphere within a few days. This complicates a comparison between a GCM simulation and observations. Using multi-year climatological averages for measured chemical species and comparing them with a modeled climatology can circumvent this problem. Unfortunately, continuous measurements of the chemical atmospheric composition that can be used to make a climatology, are only available for a limited number of surface stations around the globe. In the free troposphere fewer observations are available while the only regular observations involve O_3 soundings and water vapor (H_2O). Satellite observations currently do not provide much additional information because of the limited vertical resolution of satellite data in the earth's troposphere. Almost all other atmospheric chemistry observations are obtained during measurement campaigns, i.e. during a limited period of time in a limited area. In general, atmospheric chemistry measurements in the troposphere are largely scattered in space and time, complicating the evaluation of GCMs.

In order to solve this problem, a technique has been developed in which numerical weather prediction data is assimilated in a GCM. This technique, the "nudging", forces the GCM to follow the "observed" weather. With the use of this technique it is possible to make a direct comparison between observations and GCM output. The nudging technique will be described in more detail in paragraph 1.5.

1.4.3 Chemistry in the ECHAM model

Most of the model results presented in this thesis have been obtained from the ECHAM4 model (European Centre HAmburg Model, version 4). This numerical climate model is based on a version of the ECMWF model (European Centre for Medium Range Weather Forecasts), but it has been adjusted for climate studies (e.g. different parameterizations). The model version used in this thesis has been extended with an atmospheric chemistry scheme. Such a scheme calculates chemical reactions between atmospheric trace gases, photolysis of trace gases, advection, emissions, surface deposition, removal by rain, in-cloud reactions and reactions on particles.

Although a complete description of atmospheric chemistry is highly complex, it can be approximated using a limited set of trace gases and selecting what we believe to be the most important chemical reactions. The basic atmospheric chemistry model is a so-called background CH_4-CO-NO_x-HO_x scheme. It includes photochemistry of the most important atmospheric trace gases: photochemical breakdown of CH_4 to CO_2, the formation and destruction of nitric oxides (notably NO and NO_2), of the production and destruction of O_3 and the production and destruction of the OH and HO_2 radicals. CH_4, CO_2 and O_3 are

important greenhouse gases, and nitric oxides largely control the formation of O_3, whereas O_3 itself is important for the formation of the OH and HO_2 radicals that are important for the photochemical breakdown of a multitude of atmospheric trace gases. This scheme is well suited to describe the chemistry in clean air masses. It is less suitable to describe chemistry in polluted air masses, mainly because a description of non-methane hydrocarbon (NMHC) chemistry is not included. Although NMHCs are not dominant in global atmospheric chemistry, they are important in polluted air masses because they can lead to additional O_3 formation, and the photochemical breakdown of NMHCs ultimately leads to additional formation of CO and CO_2. In low NO_x conditions NMHCs can lead to additional O_3 destruction. It must be mentioned that in the standard background chemistry scheme used in this thesis an additional CO source is included to represent breakdown products of NMHCs.

Moreover, it is possible to extend the standard background scheme with a description of NMHC chemistry. Because of the large number of different NMHCs present in the atmosphere a complete description of NMHC chemistry would become very extensive, making it less useful for the use in climate models because it requires much computational resources. Fortunately, it is possible to approximate NMHC chemistry treating NMHCs that have a similar chemical behavior as one single group rather than calculating all individual NMHC reactions. The NMHC scheme used in some of the chapters of this thesis is the Carbon Bond Mechanism IV (CBM-4) scheme that uses 48 individual chemical species or reactants and 108 reactions [Gery *et al.*, 1989].

Both standard and NMHC versions of the model are used in this thesis. Table 1.1 gives an overview of which model version is used in which chapter, including the period for which the model was nudged. A more detailed description of the ECHAM model and both standard and NMHC chemistry schemes can be found in the appendix.

Chapter	Resolution*	Chemistry scheme	Nudging period
2	T30	Standard	16-3 - 31-4 1995
3	T30	Standard	16-3 - 1-4 1995** February and March 1998
4	T30 + T63	Standard + NMHC	February and March 1999
5	T30	Standard + NMHC	February and March 1999
6	T30	Standard	February and March 1999+1998+1997+1996

Table 1.1 Model versions used in the different chapters of this thesis. Model output was generated every 6 hours,

* T30 (spectral) resolution is approximately 3.75° latitude and longitude, T63 resolution is approximately 1.9° latitude and longitude

** Model run with output every single hour

1.5 Newtonian Relaxation

In this thesis a four-dimensional assimilation technique ("nudging") is used to relax the ECHAM4 model towards an observed state, in this case ECMWF first-guess fields of the observed weather. Originally, this technique was used to improve numerical weather

prediction by nudging the model towards observations during a spinup period, after which a model simulation produced a prediction. However, it can also be used to continuously adjust the climate model towards the analyzed weather. The climate model is forced to follow the analyzed weather, enabling a comparison of atmospheric (chemistry) observations with the model simulation. This technique is called Newtonian relaxation. A more detailed description of the technique is given by Jeuken *et al.* [1996]. The model is nudged toward the observed state by the addition of a non-physical relaxation term to the model equations:

$$\frac{\partial X}{\partial t} = F_m(X) + G(X_{obs}-X) \qquad (1)$$

With X representing a prognostic model variable, F_m is the model forcing, $(X_{obs}-X)$ represents the difference between model state and observed state and G is a relaxation coefficient (s^{-1}). At every time step the model is relaxed towards ECMWF first guess fields. Since the time step of the model does not correspond to the availability of the analyses in the data archive (6 hours), the ECMWF data are interpolated to match the model time step, as proposed by Brill *et al.* [1996].

The divergence, vorticity, temperature, surface pressure and sea-surface temperature are nudged as in Jeuken *et al.* [1996]. The choice of the relaxation coefficient G is rather arbitrary. However, if G is chosen too small the relaxation term will have little effect on the model simulation. On the other hand, if G is too large the model will be nudged too strongly to the analyses and possible imbalances can be amplified. It has been suggested to use a variable G instead of a constant G because the weather analyses are more reliable in certain model domains and less reliable in others [Hoke and Anthes, 1976]. However, it is difficult and very time-consuming to assess the exact reliability of the analyzed weather. Furthermore, the model output is only weakly dependent on the choice of G, particularly in the extratropics [Jeuken *et al.*, 1996; Krishnamurty *et al.*, 1991], so that the relaxation coefficients can be chosen to have a constant value (experiment 5 from Jeuken *et al.* [1996], given in Table 1.2).

Coefficient	G_T	G_D	G_{Vo}	G_{Spr}
value	$1 \bullet 10^{-5}$	$0.5 \bullet 10^{-4}$	$1 \bullet 10^{-4}$	$1 \bullet 10^{-4}$

Table 1.2 Relaxation coefficients applied in the ECHAM4 model. G_T, G_D, G_{Vo} and G_{spr} are the relaxation coefficients (s^{-1}) for temperature, divergence, vorticity and surface pressure, respectively.

The humidity field is not nudged. Using the humidity field from the ECMWF analysis as a nudging variable would require a different approach. The modeled humidity field is strongly dependent on the parameterizations of, for example, clouds, ice, snow and rainfall. The dependence on the parameterizations should be taken into account if the ECMWF humidity fields are used, since errors could be created by the different parameterizations in the ECMWF and ECHAM4 models. A method to nudge the humidity field is proposed by Krishnamurty *et al.* [1988, 1991]. This method uses observed rainfall rates to calculate a corresponding humidity field with the use of an

inverse modeling technique. However, this kind of inverse modeling is currently not available for the ECHAM4 model. The ECMWF data used in this study do account for the effects of the humidity on the circulation in the tropics, so that these effects are indirectly included in the nudging of the ECHAM model. Including the humidity field in the nudging process does not have a large effect on the model output. The aim of the nudging is to reproduce the observed large-scale circulation patterns without affecting the physical properties of the model. To what extent the nudging affects these properties is difficult to say, however, the more model parameters are nudged towards the ECMWF analysis, the more likely it becomes that one is comparing the ECMWF model with the observations instead of the ECHAM model.

1.6 Research questions and outline of the thesis.

This thesis is mainly concerned with INDOEX. In most chapters model results are compared with measurements. The model provides a tool to analyze the measurements, but the measurements also can be used to evaluate the model performance. This combination of measurements and model results is a very powerful tool for increasing our knowledge of atmospheric chemistry.

The main questions that will be dealt with in this thesis are the following:

- How well does the "nudging" technique work? What are the spatial and temporal scales that can be reproduced by the nudged ECHAM4 model?

- What is the chemical composition of polluted air masses over the Indian Ocean? Can we derive, from the measurements, what the sources and source regions are? How well are the sources and sinks represented in the ECHAM4 model?

- How well is the nudged ECHAM4 model capable of reproducing INDOEX measurements? Can we understand the spatial and temporal variability as seen in the measurements?

At the start of the research that resulted in this thesis, the nudging technique had just been developed, and it had only been evaluated by comparing meteorological data (precipitation) with output of the climate version of ECHAM [Jeuken *et al.*, 1996]. Whether this technique could be useful for comparing model output with in situ chemistry measurements still had to be tested. In chapter 2 measurements from the first pre-INDOEX campaign in 1995 are compared with model output from the nudged ECHAM4 model. It will be shown that the nudged ECHAM4 model is capable of reproducing the larger scale features of most of the measurements. It will also be explained why the model cannot reproduce some of the measured features.

Chapter 3 provides an example of how a model-measurement comparison can lead to new ideas and/or new insights about atmospheric chemistry processes. A comparison between O_3 measurements on an island station on the Maldives and model results shows that the model is capable of reproducing the measured diurnal O_3 cycle, including the nighttime O_3 increase. It is discussed that the mechanism behind the nighttime increase as presented in previous publications does not explain why the model shows a similar behavior as seen in the measurements. Moreover, it is shown that there are conceptual problems with the traditional explanation. An alternative approach is presented, and it is shown that this provides a better explanation for most observations. The chapter is concluded with a discussion about the implications of this new approach.

In chapter 4 a comparison is made between measured and modeled CO during the IFP of INDOEX. It is shown what the model is reasonably capable of reproducing the observations, although some discrepancies between measurements and model results exist. Possible explanations for the discrepancies are discussed. In an additional analysis the important sources and source regions for CO over the Indian Ocean are discussed, referring to both the boundary layer and in the free troposphere.

In chapter 5 hydrocarbon measurements from the IFP of INDOEX are compared with model results. It is shown which parts of the acetone measurements are reproduced by the model, and where discrepancies exist. It is also shown that the model is capable of reproducing most of the hydrocarbon mixing ratios as derived from air samples taken during measurement flights. Measurements of acetonitrile are compared with results in an attempt to model this trace gas for the first time. Discrepancies between measured and modeled acetone and acetonitrile are discussed, and possible explanations are given.

Chapter 6 provides some insight in the different physical processes that control the Indian winter monsoon, and how variations in the processes are related to variations in the circulation. During the IFP of INDOEX the question whether we could understand the spatial and temporal variability as seen in the measurements was raised on many occasions. We will show how the different atmospheric processes over the Indian Ocean affect the transports of trace gases, and provide a dynamical explanation for the observed interannual variability.

In chapter 7 a summary of the thesis is given along with a discussion of the most important model weaknesses and recommendations for future work.

Chapter 2

Tropospheric O_3 distribution over the Indian Ocean during spring 1995 evaluated with a chemistry-climate model

Abstract

An analysis of tropospheric O_3 over the Indian Ocean during spring 1995 is presented based on O_3 soundings and results from the chemistry-general circulation model ECHAM4 (European Centre Hamburg Model). The ECHAM4 model is nudged towards actual meteorology using ECMWF analyses, to enable a direct comparison between model results and in situ observations. The model reproduces observed CO levels in different air mass categories. The model also reproduces the general tendencies and the diurnal variation in the observed surface pressure, although the amplitude of the diurnal variation is underestimated. The model simulates the general O_3 tendencies as seen in the sonde observations. Tropospheric O_3 profiles were characterized by low surface mixing ratios (< 10 ppbv), mid-tropospheric maxima (60-100 ppbv, between 700-250 hPa) and upper-tropospheric minima (< 20 ppbv, between 250-100 hPa). Large-scale upper tropospheric O_3 minima were caused by convective transport of O_3-depleted boundary layer air in the Inter Tropical Convergence Zone (ITCZ). Similarly, an upper tropospheric O_3 minimum was caused by cyclone Marlene south of the ITCZ. The mid-tropospheric O_3 maxima were caused by transport of polluted African air. The ECHAM4 model appears to overestimate surface O_3 levels, and does not reproduce the diurnal variations very well This could be related to unaccounted multiphase O_3 destruction mechanisms involving low level clouds and aerosols, and missing halogen chemistry

This chapter has been adapted from: Tropospheric O_3 distribution over the Indian Ocean during spring 1995 evaluated with a chemistry-climate model, published in *Journal of Geophysical Researc*h, 1998, 104, 13881-13893, with co-authors M. Zachariasse, G.J. Roelofs, P. Van Velthoven, R.R. Dickerson, K.P. Rhoads, S.J. Oltmans and J. Lelieveld.

2.1 Introduction

During the Northern Hemisphere winter large scale cooling of the Tibetan Plateau is associated with the development of a high-pressure area over the Asian continent. In the boundary layer northeasterly outflow from this high-pressure area transports polluted air masses from Asia to the Indian Ocean and further towards the ITCZ (Inter Tropical Convergence Zone). The air masses can reach the central and south Indian Ocean, and the important question is to what extent the growing south-Asian pollutant emissions impact the composition of this relatively pristine atmosphere and the local radiation balance [Moorthy *et al.*, 1997; Rhoads *et al.*, 1997; Krishnamurty *et al.*, 1997; Lal *et al.*, 1998; Jayaraman *et al.*, 1998; Krishnamurti *et al.*, 1998].

During transport in the marine boundary layer south of India the air masses encounter different cloud regimes, from low-level stratus to shallow convection and, ultimately, the deep convective clouds of the ITCZ. These different cloud regimes likely affect the chemical composition of the air masses and vise versa. Furthermore, the deep convective clouds in the ITCZ may penetrate the tropopause and inject pollutants directly into the stratosphere. Stratospheric air can also enter the troposphere, for example, near the subtropical jet stream. This large variety of meteorological and chemical processes makes the Indian Ocean a complex and interesting region to study. Unfortunately, to date there have been few measurements of chemical species over the Indian Ocean [Savoie *et al.*, 1987; Johnson *et al.*, 1990; Chester *et al.*, 1991; Baldy *et al.*, 1996]. To investigate these processes over the Indian Ocean in more detail a major measurement campaign, INDOEX (INDian Ocean EXperiment), will take place during the 1999 Indian winter monsoon.

As a preparation to INDOEX several pre-INDOEX ship cruises have been carried out. In this paper some results from the pre-INDOEX cruise of the NOAA R/V Malcolm-Baldrige are discussed. This cruise took place from March 21 (Day of year (DOY) 80) to April 22 (DOY 112), 1995, when the ship sailed from Durban, South Africa (29.8° S, 26.1° E) to Colombo, Sri Lanka (6.7° N, 79.6° E). During this cruise, near-surface measurements of chemical species were made continuously and O_3 sondes were launched approximately once per day. For a detailed discussion, the reader is referred to Rhoads *et al.* [1997] and Dickerson *et al.* [1998] for the surface data. In this chapter an ECHAM4 model simulation for this period with the standard chemistry is presented and a comparison with the observations is made. A brief summary of the measurements is presented in section 2.2, and a description of the trajectory model follows in section 2.3. The results are presented in section 2.4, starting with the discussion of the surface data, followed by the O_3 sonde results. The chapter ends with the conclusions in section 2.5.

2.2 Measurements

On March 21, 1995, the R/V Malcolm-Baldrige departed from Durban, sailing toward Sri Lanka following the cruise track shown in Figure 2.1. During this voyage near-surface measurements of trace gases, e.g. CO, O_3, NO_x, aerosols and of meteorological variables were made. For a detailed description of these measurements see Rhoads *et al*. [1997] and Dickerson *et al*. [1998]. Rhoads *et al*. [1997] show that along the cruise track from south to north four distinct meteorological air masses or regimes were encountered, i.e. southern hemisphere marine extratropical air (SHmX), southern hemisphere marine equatorial air (SHmE), northern hemisphere marine equatorial air (NHmE) and northern hemisphere continental tropical air (NHcT). These different regimes are distinguished by sharp changes in the surface trace gas and aerosol mixing ratios measured on days 91, 101, and 107 [Figure 2.2, Rhoads *et al*., 1997].

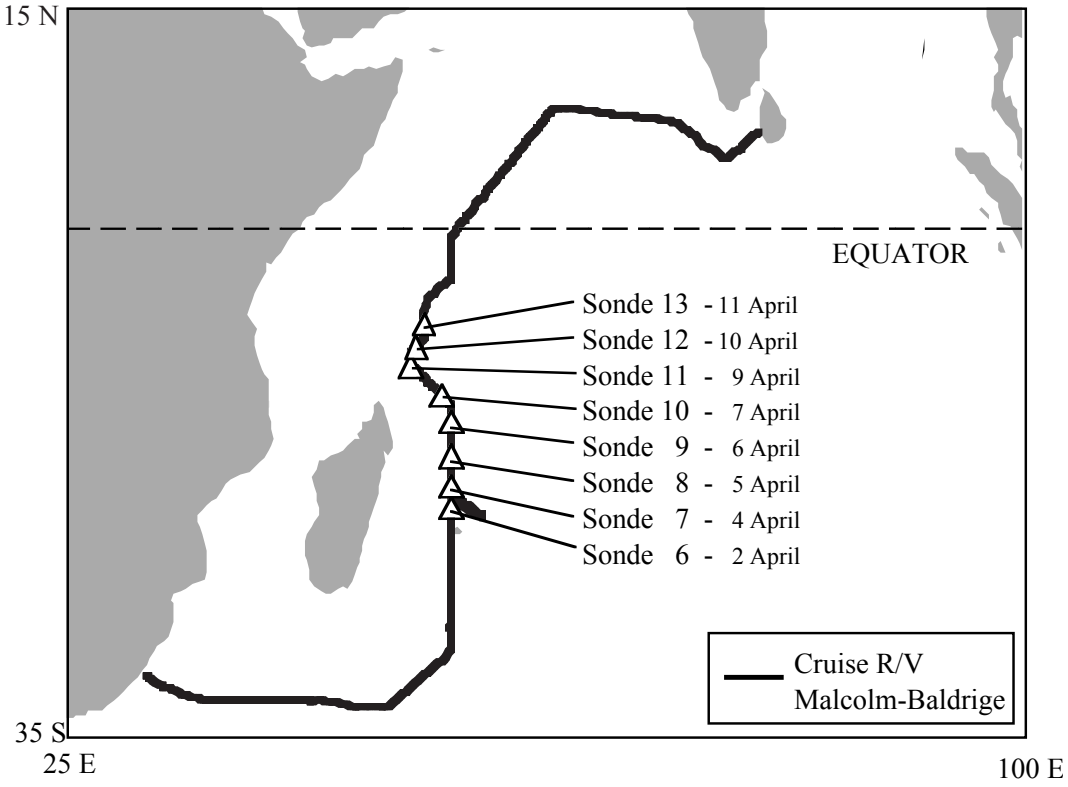

Figure 2.1 The track of the research vessel Malcolm-Baldrige. The triangles show the sites and dates were the sondes were launched. The campaign started on March 12, 1995, in Durban, South Africa, and ended on April 22, 1995, in Colombo, Sri Lanka.

O_3, humidity and temperature measurements aloft were obtained using balloon-borne electrochemical mixing ratio cell (ECC) O_3 sondes (Model 1z, En-Sci Corp., Boulder, Colorado) coupled to Väisälä radiosondes (Model RS80, Väisälä USA, Woburn, Massachusetts). The Väisälä sensors for temperature, pressure and humidity measurements were factory calibrated and have reported accuracies of 0.3°C, 0.5 hPa and 2 % respectively.

The O_3 sensor has an accuracy of ± 7 % in the troposphere, with a detection limit of 1-2 ppbv [Komhyr *et al.*, 1995]. The uncertainty at mixing ratios less than 10 ppbv is of the order of 10 %. The reported accuracies assume a constant background current correction determined on deck prior to launch. The sondes were typically launched in the early afternoon at intervals of approximately 2° of latitude. The sondes and an UV absorption instrument made simultaneous measurements for a few minutes prior to most launches. During these periods the signals tracked well together with the sonde measurements averaging 2.3 ppbv higher than the UV absorption instrument. The observed differences between the two signals are within the combined uncertainty of the two detectors.

2.3 Trajectory model

Trajectory analyses were performed in order to determine the origin of the air masses of interest. The trajectory model used in this study is the KNMI (Royal Netherlands Meteorological Institute) trajectory model [Scheele *et al.*, 1996]. Three-dimensional ECMWF first-guess (6 hour forecast) wind fields are used to calculate the displacement of an air parcel for each model time step of the trajectory model. The use of first-guess data instead of analyses ensures that the wind fields and mass distribution fields are in physical balance. The first-guess wind data are available at 31, hybrid σ-p, model levels and at a horizontal resolution of T213 (approximately 0.5°x0.5°).

Since the gridpoints and times of these wind data generally do not coincide with those of the points for which the back trajectories are determined, interpolation in space and time is required. The spatial interpolation is linear in the horizontal direction and linear with log(p) in the vertical direction. A quadratic interpolation in time is applied to convert the 6-hour wind field data to 1-hour data, matching the time step of the trajectory integration. The calculation of a new trajectory position is performed iteratively until the difference between subsequent estimated end points is less than 300 m in the horizontal and less than 0.0001 times the pressure in the vertical direction.

2.4 Results

2.4.1 Surface data

A comparison is made between model and measurements for CO, O_3 and the surface pressure. Since the location and time of the observations generally do not coincide with those of the ECHAM4 model, interpolation of the model output in space and time is performed for both sonde and surface observations. Tables 2 and 3 list the average CO and O_3 mixing ratios for the four different air mass regimes as indicated in section 4.

	SHmX	*SHmE*	*NHmE*	*NHcT*
CO measured	54.1 (± 4.0)	59.3 (± 3.7)	89.0 (± 3.3)	120.4 (± 9.8)
CO ECHAM4	55.0 (± 2.7)	58.7 (± 0.9)	96.3 (± 7.6)	110.7 (± 12.5)

Table 2.2 Average measured and modeled CO mixing ratios (ppbv) at the surface for the four different air mass regimes. Standard deviations are shown in brackets. Measurements are from Rhoads *et al.* [1997].

	SHmX	*SHmE*	*NHmE*	*NHcT*
O_3 measured	17.0 (± 1.8)	11.5 (±2.5)	7.5 (± 1.2)	15.7 (± 2.9)
O_3 ECHAM4	20.8 (± 3.2)	16.9 (± 2.0)	14.1 (± 1.0)	24.6 (± 4.7)

Table 2.3 Average measured and modeled O_3 mixing ratios (ppbv) at the surface for the four different air mass regimes. Standard deviations are shown in brackets. Measurements are from Rhoads *et al.* [1997]. Mixing ratios in ppbv.

From Figure 2.2 and Table 2.2 it can be seen that the simulated CO mixing ratios of both the SHmX air mass and the SHmE air mass agree well with the measurements (Julian days 81 to 91.5). The air mass encountered between DOY 92 and DOY 94 is probably affected by local emissions [Rhoads *et al.*, 1997]. The measured CO mixing ratios for the southern hemisphere air masses can be considered to represent background CO mixing ratios as they are far away from major pollution areas. Furthermore, according to Figure 2.2, the model calculates the ITCZ at the right location and time, as indicated by the increase in CO mixing ratio on DOY 102, although the modeled transition is more gradual. On average, the model produces higher mixing ratios for the NHmE air and lower mixing ratios for the NHcT air, but observations and modeled mixing ratios are still within the modeled standard deviation (see Table 2.2). The observations show two distinct maxima in the CO mixing ratios between DOY 107 and 111, with peak values of about 140 ppbv. These maxima are related to the vicinity of the Indian subcontinent [Rhoads *et al.*, 1997]. The model captures only the second maximum, probably related to the relatively low resolution of the model. However, the maximum modeled mixing ratio for the second maximum is the same as the observed one. As for the timing of the change from the NHmE mass to the NHcT air mass, the changes in the model are again at the right location and time (Julian Day 107). This can

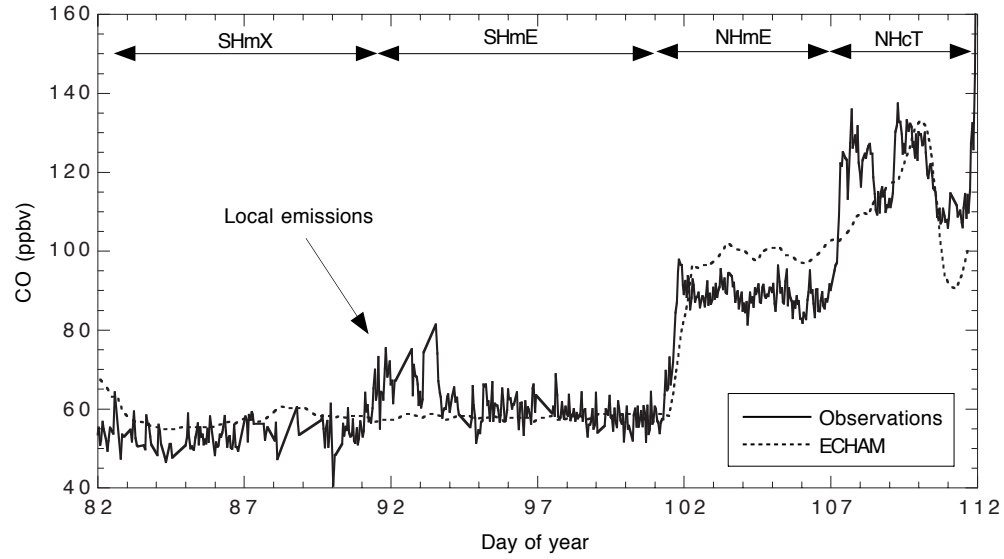

Figure 2.2 Comparison between measured and modeled CO. The observations are shown by the solid line, the model results by the dashed line. The arrows at the top of show the position of the different types of air (see section 4).

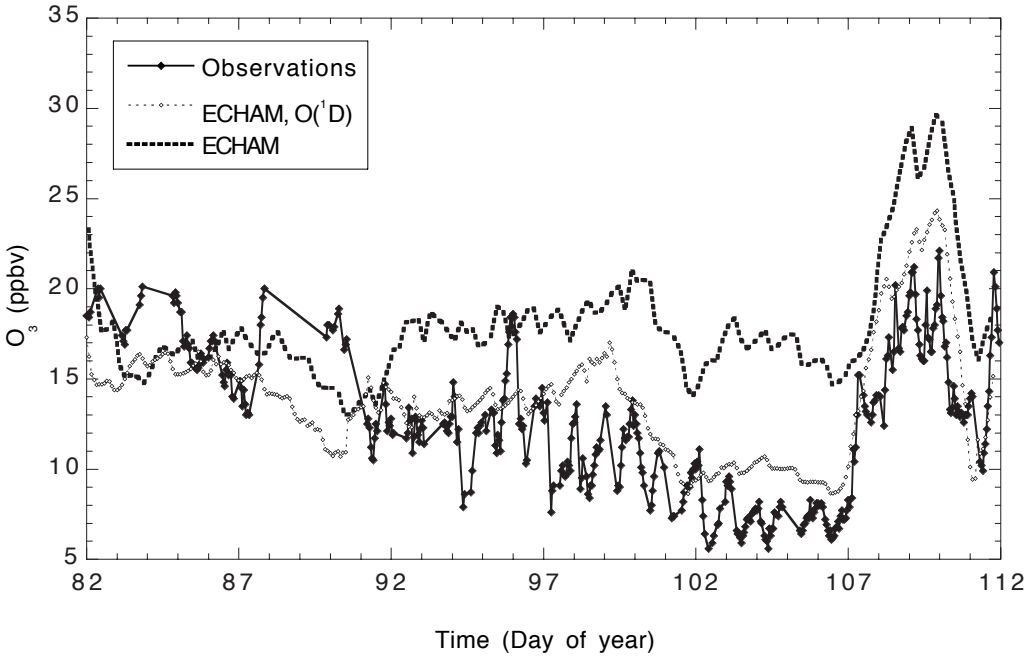

Figure 2.3 As Figure 2.2 but for O_3. The thick dashed line shows the model calculated O_3 for which the O_3 destruction through the reaction $O(^1D) + H_2O$ in the marine boundary layer has been doubled over the Indian Ocean.

be seen even better in Figure 2.3 for O_3. Taking the large standard deviations into account, modeled and observed CO mixing ratios seem to compare well.

The results for O_3 are shown in Figure 2.3 and the average mixing ratios of the different types of air are given in Table 2.3. The most striking feature of Figure 2.3 is the low O_3 mixing ratio (7.5 ppbv on average) for the NHmE air. Similar or even lower mixing ratios have been measured in the equatorial Pacific [Routhier *et al.*, 1980; Fishman *et al.*, 1983; Piotrowicz *et al.*, 1986; Piotrowicz *et al.*, 1991; Singh *et al.*, 1996; Kley *et al.,* 1996]. Such low O_3 mixing ratios appear to be a common feature of remote equatorial marine environments. They are associated with clean, NO_x-depleted O_3 destruction conditions, although the exact mechanisms by which the very low mixing ratios are caused are still a subject of debate [Singh *et al.*, 1996].

Figure 2.3 shows that the model is capable of producing the same observed latitudinal trend, but it produces higher O_3 mixing ratios during most of the period, except for DOY 82-85 and 88-91. Note that for DOY 88-91 only a few observations were available. The mean difference between observed O_3 and modeled O_3 is 6 ppbv (± 3 ppbv). Figure 2.4 shows the observed and modeled NO_x mixing ratios. Observations were only available for the period after DOY 101. The uncertainty in NO_x is 20 pptv while the average NO mixing ratio is 6 pptv. Although the modeled NO_x mixing ratios are generally much lower than observed, mixing ratios in both observations and model indicate that O_3 production is very slow. Therefore, the model overestimation of O_3 in the Indian Ocean boundary layer is not caused by an overestimation of photochemical O_3 production, but rather by some O_3 destruction mechanism that is not well represented by the model. It is not likely that the O_3 mismatch is caused by a problem in the model representation of transport and mixing. In that case a similar problem would arise with CO, not manifest from Figure 2.2. A possible explanation could be the neglect of multiphase chemical processes in low-level clouds of aqueous aerosols.

Cloud and aerosol chemistry could lead to enhanced destruction of peroxy radicals that form O_3, to O_3-loss in the aqueous phase [Lelieveld and Crutzen, 1990], or to the release of reactive halogens from dissolved sea salt and subsequent O_3 destruction [Vogt *et al.*, 1996]. A first estimate has been obtained by increasing the O_3 destruction in the marine boundary layer of the model. The reaction rate of $O(^1D) + H_2O$ is multiplied by a factor of 2. Figure 2.3 shows that this strongly improves the agreement.

A remarkable feature, which can be seen in Figure 2.3, was the strong diurnal cycle present in the O_3 measurements (DOY 93-107). This diurnal cycle could have been caused by photochemical O_3 destruction during the day, and nighttime replenishment by mixing. A diurnal cycle with a minimum during the day is discernible in the model results (DOY 93-107), consistent with the measurements, but the amplitude is smaller then the observed one. The observed amplitude of the diurnal cycle has a value of about 4 ppbv while the amplitude in the model is about 0.5-1.0 ppbv. Rhoads *et al.* [1997] noted that O_3 destruction started after sunrise and that the lowest O_3 levels were found just after solar noon. The model also shows a minimum during daytime caused by daytime photochemical destruction of O_3, mostly through photodissociation of O_3 and the subsequent reactions of $O(^1D)$ with H_2O. Enhanced daytime photochemical O_3 destruction would be consistent with the mechanisms proposed by Lelieveld and Crutzen [1990], Vogt *et al.* [1996] or Dickerson *et al.* [1998], which will be studied in greater detail in future.

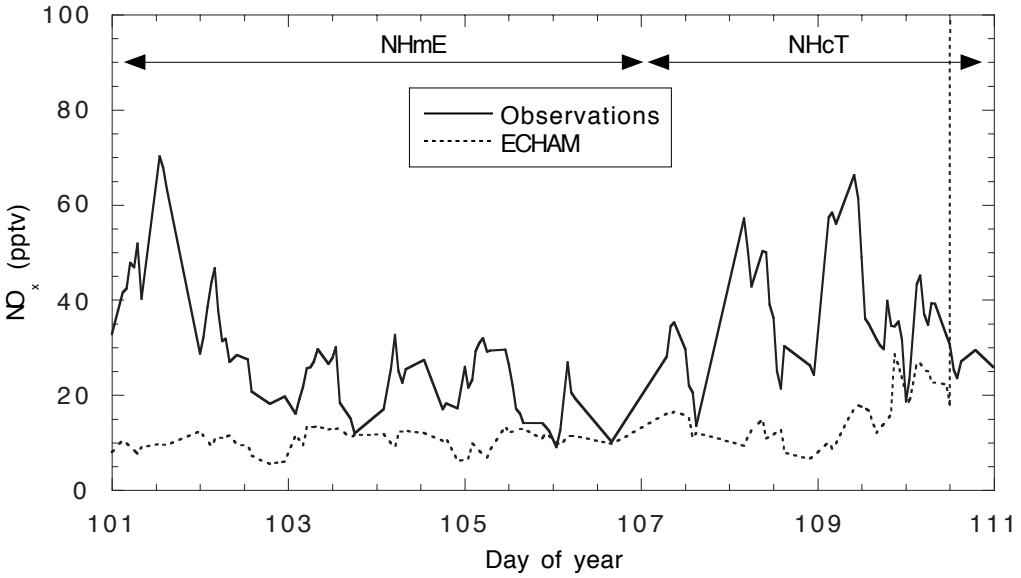

Figure 2.4 Same as Figure 2.2 but for NO_x, for the last ten days of the campaign (Day of year101-111).

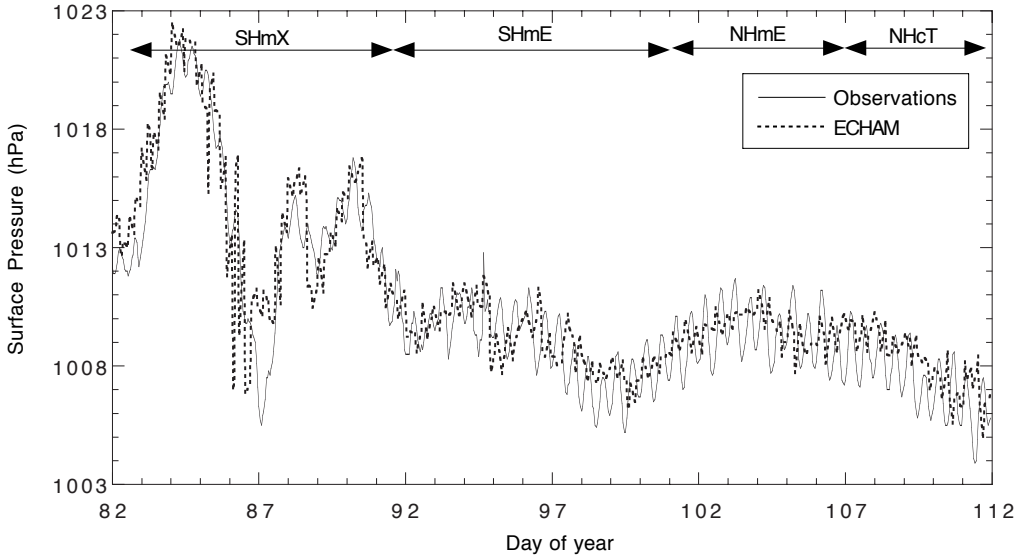

Figure 2.5 As Figure 2.2 but for the surface pressure.

In Figure 2.5 a comparison is made between measured and modeled surface pressure, which on average agree very well. The maxima on Julian Days 84, 88 and 91 and the minima on days 84 and 87 are reproduced by the model, as well as the overall tendency for the period after Julian Day 92. The model also produces the semi-diurnal variability although the modeled amplitude (0.5-1.0 hPa) is smaller than the observed one (1.5 hPa). This is most clearly shown for the period after DOY95. This semi-diurnal cycle of the surface pressure is consistent with the findings of Hsu and Hoskins [1989] who found that such fluctuations in the ECMWF analyses are consistent with tidal movements. Although the surface pressure is a nudged variable, a good agreement between measured and modeled surface pressure is not trivial. The ECMWF analyses in this region are based on only a few observations so that uncertainties in the model performance can be expected. However, according to Figure 2.5 this is not the case for the surface pressure.

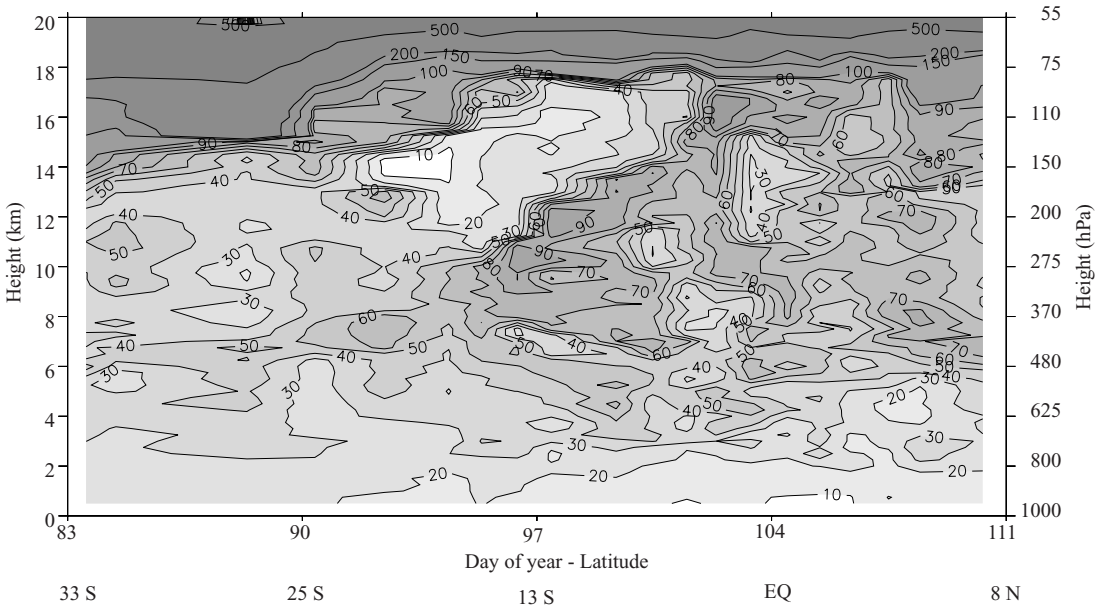

Figure 2.6 Latitude/time versus height contour plot for O_3 for all sonde observations performed during the 1995 campaign. Contour values given in ppbv.

2.4.2 O_3 Sondes

Figure 2.6 shows the O_3 contour plot for all sondes. Two remarkable features in the upper air data are the relative ozone minimum at 175 hPa, near 18S, and O_3 maximum at 300 hPa, around 13S. The minimum was observed over the course of 5 days from four consecutive sondes. These upper tropospheric layers showed ozone levels ranging from 20 to less than 10 ppbv. Although the region of minimum ozone is not associated with high relative humidity, large-scale rising motion may have lifted low ozone air up from the boundary layer and lower free troposphere. Mixing ratios at the minimum are in line with those observed in the lower free troposphere and a more humid layer appears at the

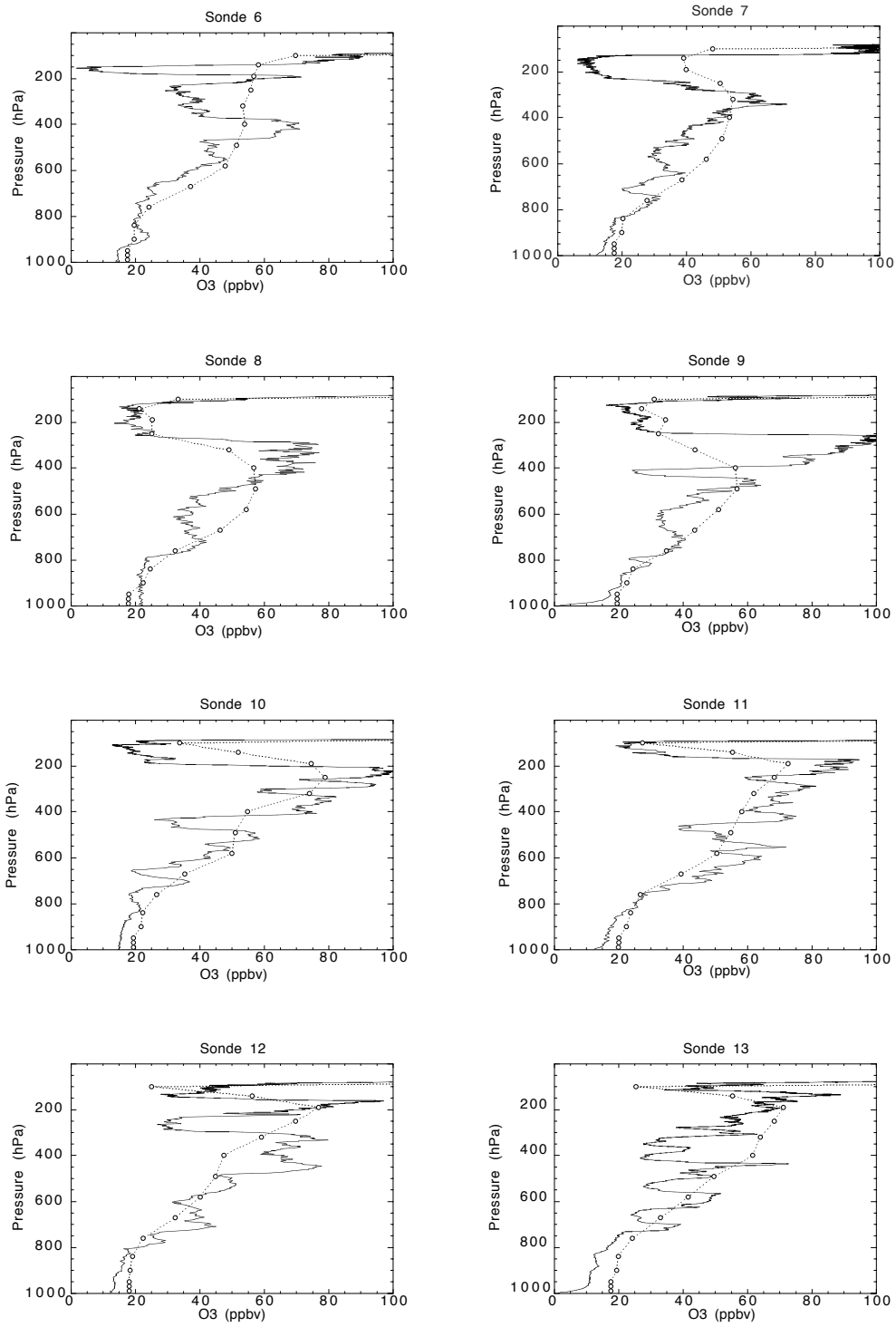

Figure 2.7 Comparison of eight O_3 sondes and the modeled O_3 profiles. Location and time of release of the sondes are given in Figure 2.1. The observations are denoted by the solid lines, the model output by the dashed lines.

bottom of low ozone strata in several of the profiles. The region of high O_3 coincides with quite low relative humidity (~5%), suggesting that the air is stratospheric in origin. Figure 2.7 shows the comparison between eight O_3 soundings and the ECHAM4 model results. The positions of the sondes as well as the dates on which they were released can be seen in Figure 2.1. The 8 sondes show some common features. At the surface the O_3 mixing ratios are relatively low due to photochemical destruction. The O_3 mixing ratios increase with height, and the highest O_3 levels are found between 400 and 200 hPa (7-12 km). Directly above these maxima very distinct minima appear. The ECHAM4 model is capable of capturing most of these general features, i.e. the low surface mixing ratios, the gradual increase of O_3 mixing ratios with height and the upper tropospheric minimum. The model also captures the tropopause height, indicated by the sharp increase in O_3 mixing ratios above 100 hPa.

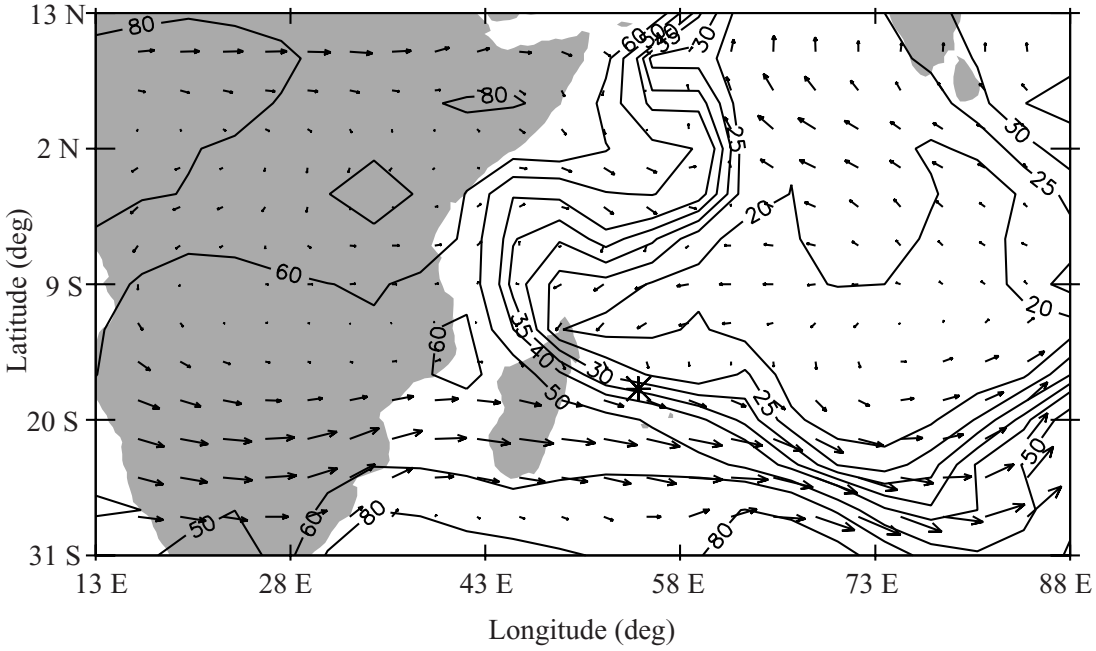

Figure 2.8 Simulated O_3 mixing ratios (ppbv) for April 4 at 05:00 UTC at an altitude of 190 hPa. Also shown are the wind fields (arrow length in arbitrary units). The asterisk at 55E, 18 S denotes the position of the ship.

The upper tropospheric minimum is the result of the ITCZ outflow at this height. The convective cells at the ITCZ ventilate boundary layer air all the way up to the tropopause. The boundary layer air has O_3 mixing ratios of about 20 ppbv or less, and in some cases the upper tropospheric minima also approach 20 ppbv. Figure 2.8 shows the model results at the 190 hPa level on April 4. A distinct minimum covers the entire Indian Ocean. To the west, the O_3 depleted air is bordered by O_3 rich continental African air. To the south the minimum is delimited by the subtropical jet, which transports O_3 rich African air eastward. The subtropical jet is also associated with transport of stratospheric air into the troposphere. This is illustrated in Figure 2.9, which shows the ECMWF analysis at 61° E on April 3. Between 300 and 100 hPa (10-18 km, near 30° S)

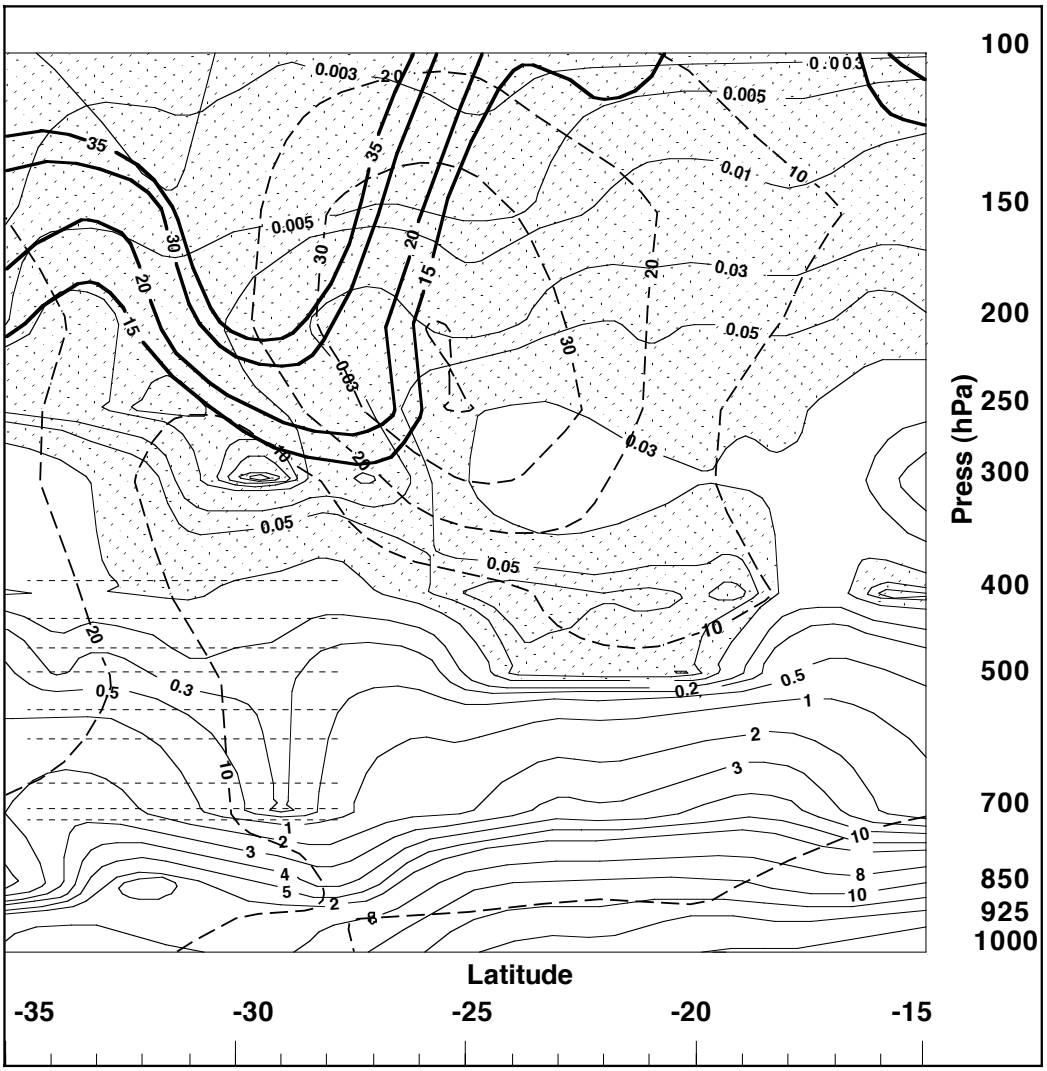

Figure 2.9 ECMWF analyses at 61°E on April 3 (18:00 UTC). *Thin solid line*: specific humidity (g/kg), with shaded regions showing air dryer than 0.1 g/kg. *Thick dashed line*: zonal wind velocity (m/s). *Thick solid line*: potential vorticity (0.1PVU).

a tongue of high potential vorticity descends into the troposphere. At this location stratospheric O_3 was transported into the troposphere. At the locations where the O_3 depleted marine air and O_3 rich continental air meet, sharp gradients occur (Figure 2.8) Figure 2.10 shows that the mid-troposphere is generally O_3-richer than the marine boundary layer and the upper troposphere. Relatively low O_3 levels occur in a relative small corridor at about 75° E. It appears that this area is affected by cyclone Marlene which was present at 65° E, 15 S°.

To investigate the origin of the upper-tropospheric O_3 minimum observed in sonde 7 (April 4), a trajectory study was performed. Figure 2.11 shows 5-day back trajectories starting at 150, 180 and 210 hPa, representing the air in the O_3 minimum, and at 305,

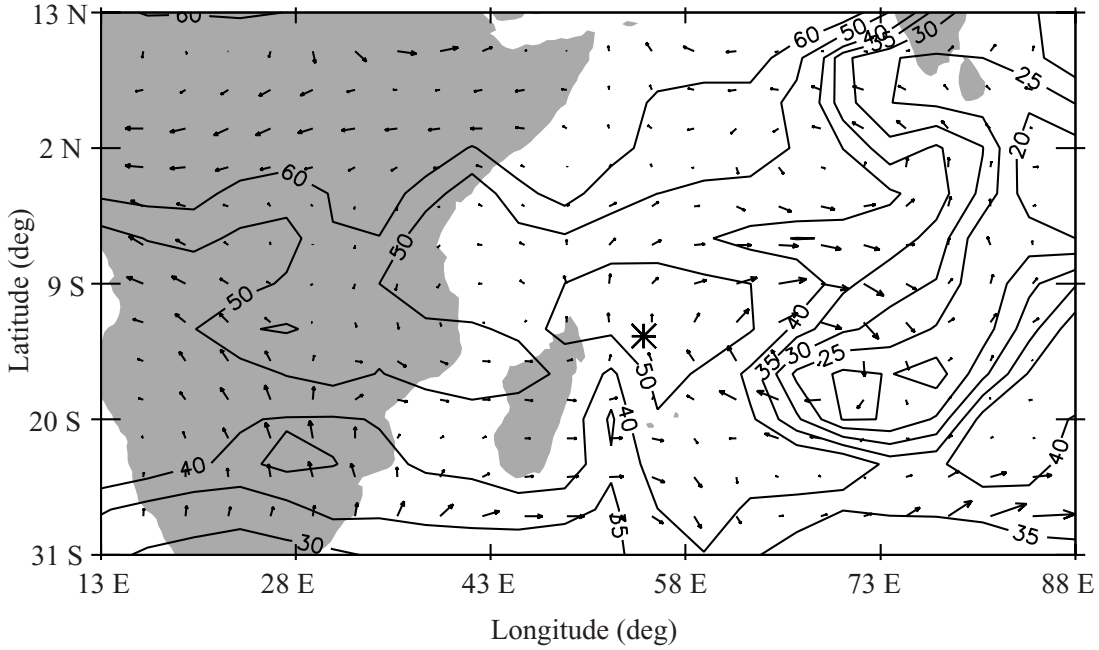

Figure 2.10 As Figure 2.8 but for April 6 at 07:00 UTC at an altitude of 580 hPa.

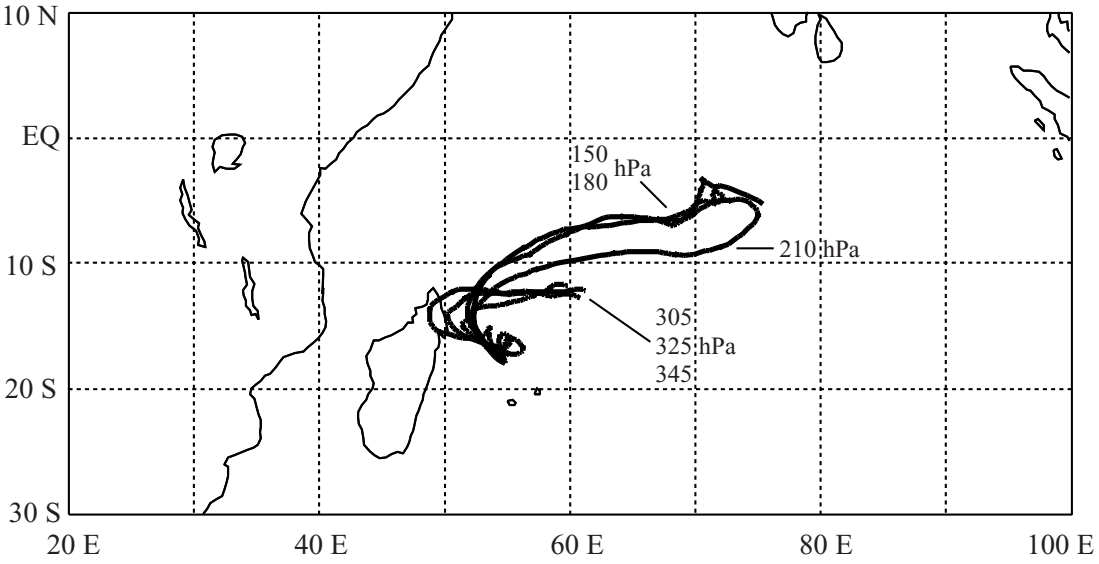

Figure 2.11 Back trajectories from April 4 (10:00 UTC) to March 30 (10:00 UTC), starting at 55E, 18.02S. The trajectories are marked by their starting pressure, i.e. 150, 180, 210, 305, 325 and 345 hPa.

325 and 345 hPa, representing the air mass below the minimum. The air in the minimum clearly originates from the northeast, where O_3-depleted air is present according to the model (Figure 2.8). Figure 2.12 shows the vertical displacement of the trajectories. As the trajectory model does not capture individual convective cells, the trajectories mainly remain in the upper troposphere. The trajectory at 210 hPa, however, originates from the boundary layer. This can be traced back to the tropical cyclone Marlene. The strong vertical motion is caused by organized upward flow in cyclone Marlene.

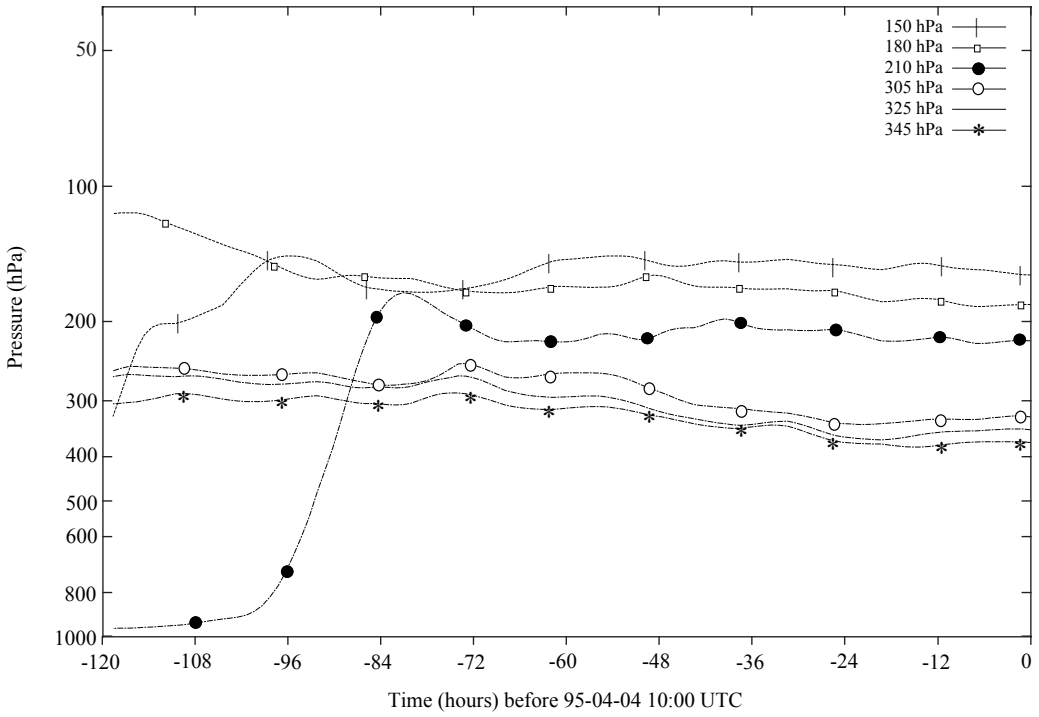

Figure 2.12 Pressure evolution with time of back trajectories from April 4 (10:00 UTC) to March 30 (10:00 UTC). On April 4 the trajectories started at the following pressure levels: 150, 180, 210, 305, 315 and 345 hPa.

The model is generally capable of matching the observed O_3 minimum in the upper troposphere. However, for sonde 6 the model cannot capture the minimum. The reason is probably that the vertical extent of the minimum is comparable to the size of a gridbox, which makes it difficult to model. For sonde 7 the model does produce a minimum, but the modeled O_3 mixing ratios are too high. According to Figure 2.8, the location of the sonde at that moment is within a sharp O_3 gradient. A relatively small shift within this gradient can strongly influence calculated O_3 mixing ratios, especially considering the size of the model grid cells.

Due to the coarse vertical resolution the model cannot capture most of the small-scale features apparent in the observations. The model does reproduce the general shape of the O_3 profiles although it somewhat underestimates the mid-tropospheric O_3 maximum. This might be related to the absence of higher hydrocarbon chemistry, which can cause

an increase in the O_3 mixing ratios of 10-20 ppbv in air that is affected by pollution emissions [Roelofs *et al.*, 1997a]. The model does not reproduce the O_3 maximum at 300 hPa observed from sonde 9. Back trajectories calculated for this location (Figure 2.13) show that the air above 160 hPa originates from the east while below 180 hPa the air originates from the west. If the back-trajectories are representative for the meteorological situation, O_3 rich air would be found in the observations of sonde 9 at 180 and 200 hPa. This is definitely not the case at 180 and 200 hPa as can be seen in Figure 2.4. The inconsistency between the observed profile and the back-trajectories (the back-trajectories start close to each other but have a completely different origin) is indicative of the uncertainties involved in reproducing the meteorological situation. The resolution of the ECHAM4 model is much lower than that of the trajectory model, and it cannot be expected that ECHAM4 reproduces such small-scale meteorological features.

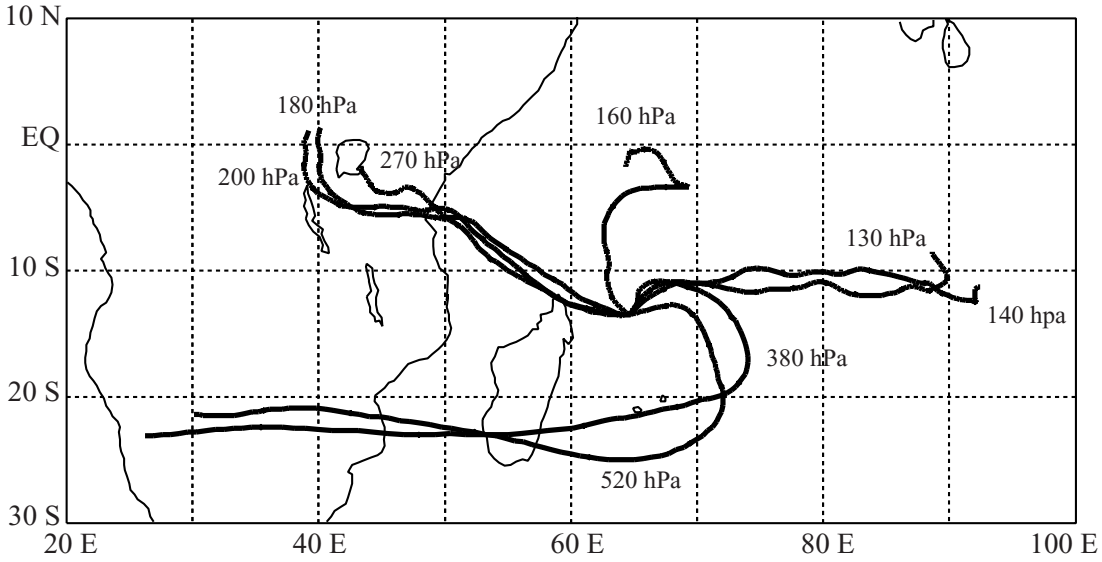

Figure 2.13 Back trajectories from April 6 (10:00 UTC) to April 1 (10:00 UTC), starting at 55E, 13.56S. The trajectories are marked by their starting pressure, i.e. 130, 140, 160, 180, 200, 270, 380 and 520 hPa. The trajectories starting at 380 and 520 hPa are representative for all trajectories starting at pressure levels between 380 and 520 hPa.

At lower levels (520-380 hPa) the trajectories for sonde 9 are very consistent. They all originate from the southern part of Africa. The trajectories move eastward over the southern tip of Madagascar and then curve around to the measurement site. The trajectories suggest transport of O_3 rich African air. This is consistent with the findings of Piketh *et al.* [1996], Tyson *et al.* [1996], Tyson *et al.* [1997] and Bremaud *et al.* [1998], who all reported transport of polluted (O_3 rich) southern African air into the southern Indian Ocean. The ECHAM4 model reproduces the observed O_3 mixing ratios at this altitude, and Figure 2.10 shows south-easterly winds around 60° E, 15 S, consistent with the curved trajectories at this location. In general, stratosphere-troposphere transports are small in the tropics, and stratospheric O_3 contributes only a few ppbv to tropospheric O_3 at low latitudes [Roelofs and Lelieveld, 1997].

Therefore, the model analysis suggest that this mid-tropospheric O_3 maximum is caused by African biomass burning emissions of O_3 precursors, possibly somewhat underestimated by the model due to the neglect of higher hydrocarbon chemistry.

2.5 Conclusions

A description of the tropospheric O_3 distribution over the Indian Ocean during spring 1995 is presented, and compared to the observations with the nudged ECHAM4 model. This is the first (successful) application of the nudging technique in a chemistry GCM. A number of features present in the O_3 distribution stand out:

- Relatively O_3-deficient air occurs in the marine boundary layer due to efficient photochemical O_3 destruction; destruction appears to exceed standard gas phase chemistry.

- Relatively high O_3 levels occur close to the Indian continent (~ 20 ppbv) in low-level outflow of polluted air. This is consistent with relatively high CO levels in these air masses.

- Relatively high O_3 levels (~ 15-20 ppbv) are also found at about 20°-30° S, e.g. much higher than the central Pacific boundary layer, probably influenced by biomass burning effluents from the African continent.

- Convective outflow in the upper troposphere in the ITCZ causes large-scale O_3 minima over the central Indian Ocean. The vertical extent of the outflow and the O_3 minima is fairly narrow, mostly confined to the 250-100 hPa region.

- At mid-tropospheric levels (750-250 hPa) high O_3 mixing ratios are apparent, often in confined layers. These high O_3 levels are likely caused by mid-tropospheric outflow of polluted African air.

The ECHAM4 model reproduces the background CO levels as well as the enhanced CO levels in the NHmE and NHcT air masses. The model reproduces the location of mody of these distinct air masses very well. From the comparison between modeled and observed CO it can be concluded that the ECHAM4 model reproduces the large-scale advection processes and the associated tracer transports.

The model reproduces both the overall tendencies and the diurnal variations of the surface pressure, another indication that it simulates the correct meteorology. Although the model reproduces the spatial O_3 tendencies and relatively low O_3 mixing ratios compared with O_3 mixing ratios in the free troposphere, it overestimates O_3 in the marine boundary layer and it underpredicts the diurnal variation in O_3. Since the model underpredicts NO_x over parts of the Indian Ocean, it can be expected that a model increase of O_3 loss is needed rather than a reduction of O_3 production. It is hypothesized that the discrepancy between the modeled and observed diurnal cycle is caused by the

neglect of multiphase chemistry in clouds or aerosols in the marine boundary layer. Accounting for these processes, e.g. in a future model version, is expected to increase the calculated photochemical O_3 destruction.

The ECHAM4 model reproduces both the upper tropospheric O_3 minima and mid-tropospheric maxima. The model also reproduces the transport of O_3–depleted boundary layer air to the upper troposphere by tropical cyclone Marlene. The upper tropospheric O_3 minimum stretches out over large parts of the Indian Ocean. However, the modeled upper tropospheric O_3 levels are generally too high, consistent with the overestimated surface O_3 levels [see Lawrence *et al.*, 1999]. On the other hand, the mid-tropospheric O_3 maxima are somewhat underestimated, which could be related to missing higher hydrocarbon chemistry. The mid-tropospheric O_3 maxima are likely caused by transport of polluted air from the southern part of Africa. Tropical cyclones (e.g. Marlene) influence vertical trace gas distributions over large areas. Organized convection associated with these cyclones enhances vertical exchange between the boundary layer and the free troposphere. Cyclone Marlene caused extended O_3 minima in the middle troposphere and substantially increased the extent of the upper tropospheric O_3 minima.

Future improvements of the model will include implementation of a higher hydrocarbon chemistry scheme to study the role of pollution chemistry in more detail. The model will also be applied at T63 resolution (~ 2° x 2°) to improve representations of synoptic scale weather systems.

Chapter 3

Diurnal ozone cycle in the tropical and subtropical marine boundary layer

Abstract

A conceptual analysis of diurnal ozone (O_3) changes in the marine boundary layer (MBL) is presented. Such changes are most pronounced downwind of O_3 sources in tropical and subtropical latitudes, and during summer at higher latitudes. Previously, it has been assumed that daytime photochemical O_3 loss, and nighttime replenishment through entrainment from the relatively O_3-rich free troposphere, explains the diurnal O_3 cycle. We show, however, that in a net O_3-destruction environment (low NO_x) this diurnal cycle can be explained by photochemistry and advection, which establish a horizontal O_3 gradient that is typical for the MBL. We support this hypothesis firstly by calculations with a conceptual 1-D advection-diffusion model, and secondly by simulations with an interactive 3-D chemistry-transport model. The results are in good agreement with observations, for example, in the Indian Ocean Experiment (INDOEX).

This chapter has been adapted from: Diurnal ozone cycle in the tropical and subtropical marine boundary layer, published in *Journal of Geophysical Research*, **105**, 11547-11559, 2000, with Jos Lelieveld as co-author

3.1 Introduction

Since the recognition of ozone as an important chemical specie in the troposphere it has been extensively measured and monitored during campaigns and from ground stations. Some of these campaigns have been performed over the remote oceans, and a number of surface stations are situated in remote areas as well. These campaigns and surface stations were established to improve the knowledge about the "background" troposphere, i.e. the chemistry of unpolluted air. From these campaigns and stations it was discovered that the remote marine troposphere, especially in the tropics, is a significant sink region for many chemical species, including O_3 [e.g. Kley *et al.*, 1996]
It has long been recognized that, depending on the NO_x mixing ratios, two distinct O_3 regimes exist (NO_x = NO + NO_2). In areas with relatively high NO_x mixing ratios (NO_x exceeding roughly 50-100 pptv) O_3 production dominates destruction during daytime, while in low-NO_x environments (NO_x less than roughly 50-100 pptv) net O_3 destruction prevails [Crutzen, 1974]. The chemical lifetime of NO_x is only a few days, and both O_3 and NO_x have no oceanic source, so that most of the marine lower troposphere is a net O_3 destruction area. Indications of whether an area is a net O_3 source or a sink can be derived from the diurnal O_3 cycle, because photochemical production and destruction are restricted to daytime. A summary of such effects is given in Table 3.2. It also shows the observed amplitude of the diurnal O_3 cycle, whether the amplitude is calculated from the daytime O_3 depletion rate or averaged over a longer period and the maximum observed O_3 mixing ratio.

The amplitudes of the observed diurnal O_3 cycles have values of the order of a few ppbv. Most campaigns observed that the maximum in the O_3 mixing ratio over the oceans occurs late at night (just before sunrise) and that the minimum mixing ratios occur during the late afternoon (just before sunset). The depletion of O_3 under low-NOx conditions, mostly due to the photolysis of O_3 and the subsequent reaction of $O(^1D)$ with H_2O, causes the daytime O_3 decrease. After sunset O_3 starts increasing until sunrise. The increase in O_3 has been attributed to entrainment of relatively O_3-rich air from the free troposphere into the marine boundary layer (MBL). This has been confirmed by photochemical box models, budget studies and 1-D models in which this exchange was included (Table 3.1).

Reference	**Model type**	**Entrainment rate (mm s^{-1})**	**Amplitude of diurnal O_3 cycle (ppbv)**
Thompson and Lenschow (1984)	1-D	3	1
Paluch *et al.* (1995)	Box		0.75-2.25
Noone *et al.* (1996)	Budget	7	1
Heikes *et al.* (1996)	Budget	7	1
Ayers *et al.* (1997)	Box	3	0.5
Bremaud *et al.* (1998)	Box	1 (day) 14 (night)	< 0.5 2

Table 3.1 Diurnal O_3 cycle computations from several studies and inferred entrainment rates

Reference	**Type of measure-ment**	**Location**	**Amplitude of diurnal O_3 cycle (ppbv)**	**Maximum O_3 mixing ratio measured (ppbv)**	**Type of measure-ment data[a]**
Oltmans (1981)	Surface Stations	Mauna Loa Samoa	2 1	25 20	T
Liu *et al*. (1983)	Ship	Eq. Pacific Ocean	1	20	D
Piotrowicz *et al*. (1989)	Ship	Eq. Atlantic Ocean	1.5	50	T
Johnson *et al*. (1990)	Ship	Eq. Indian Ocean Eq. Pacific Ocean	1	30	T
Thompson *et al*. (1993)	Ship	Eq. Pacific Ocean	0-1.15	22	T
Anderson *et al*. (1993)	Aircraft	Eq. Atlantic Ocean	4	50	D
Oltmans and Levy II (1994)	Surface stations	Bermuda Barbados	1 1.5		T
Paluch *et al*. (1994)	Aircraft	Eq. Pacific Ocean	1.5-4	40	D
Paluch *et al*. (1995)	Aircraft	Eq. Atlantic Ocean	2.75	20	D
Ayers *et al*. (1996), Ayers *et al*. (1992), Ayers *et al*. (1997), Monks *et al*. (1998)	Surface station	Cape Grim	1.4 (summer)	35	T
Bremaud *et al*. (1998)	Surface station	Reunion	2	30	T
Lal *et al*. (1998)	Ship	Eq. Indian Ocean	1.5	30[b]	T
This study (see also Dickerson *et al*., 1999)	Surface station	Eq. Indian Ocean	1.5	40	T

Table 3.2: Measurements of the diurnal O_3 cycle in marine locations.

One problem with these models, however, is that the entrainment is parameterized because the models cannot resolve the entrainment process explicitly. A usual procedure is to use a constant entrainment flux, either calculated from flux measurements, or from the entrainment velocity and an O_3 mixing ratio increment across the top of the boundary layer:

$$\textit{Entrainment flux} = w_e \bullet O_3 \qquad (3.1)$$

in which w_e is the entrainment velocity and ΔO_3 is the O_3 increment [Lenschow *et al*., 1982; Thompson and Lenschow, 1984]. In this approach the models are allowed to reach an equilibrium in which the daytime removal equals the nighttime recovery. These two processes then establish the diurnal O_3 cycle.

[a] D is the daytime O_3 depletion rate, and T is the average total over a longer period
[b] Value valid for the oceanic regions. In coastal regions concentrations increased to 70 ppbv

A more extensive expression for the entrainment of O_3 into the boundary layer, derived from thermodynamic equations, is given by Bremaud *et al.* [1997]:

$$\delta O_3 = \alpha \frac{H_0}{\rho C_p} \frac{1}{z_i} \frac{\Delta O_3}{\Delta \theta} \qquad (3.2)$$

in which δO_3 is the enhancement of O_3 throughout the entire boundary layer, ΔO_3 is the O_3 increment at the top of the boundary layer, ρ is the air density, C_p is the heat capacity of air, H_0 is the surface sensible heat flux, $\Delta\theta$ is the strength of the temperature inversion and α is a constant which expresses the ratio between the entrainment sensible heat flux and the surface sensible heat flux. The term δO_3 can be interpreted as the amount of O_3 transported into the boundary layer and distributed throughout the column per unit of time. In Table 3.3 some typical values for the above mentioned variables are summarized.

ΔO_3	-30 to 40 ppbv
H_0	10-100 Wm^{-2}
Z_i	500-1500 m
$\Delta\theta$	0.5-3 K

Table 3.3. Typical ranges of values used in equation (3.2). ΔO_3 is the O_3 increment at the top of the boundary layer, H_0 is the surface sensible heat flux, Z_i is the boundary layer height and $\Delta\theta$ is the strength of the temperature inversion.

With $\rho C_p = 1.3\ 10^3\ Jm^{-3}K^{-1}$ and $\alpha = 0.2$, the value of δO_3 can range between –6.6 and 8.8 ppbv $hour^{-1}$ throughout the boundary layer, assuming ΔO_3 ranges between -30 to 40 ppbv [Kawa and Person, 1989; Paluch *et al.*, 1995; Noone *et al.*, 1996]. The boundary layer air can be replenished by free tropospheric air within a few hours according to this calculation, and O_3 mixing ratio changes can be either positive or negative. The entrainment flux (δO_3) determines to a large extent the amplitude of the diurnal O_3 cycle. The enhancement fluxes derived from equation (3.2) are almost two orders of magnitude larger than what can be derived from Table 3.2. However, the values given in Table 3.2 are averages over longer periods of time, and the amplitude of the diurnal cycle on a given day can be 3 or 4 times larger than the average amplitude (see for example Figures 3.3a and 3.3b). A rather high amplitude of 10 ppbv day^{-1} requires an enhancement flux of about 0.8 ppbv $hour^{-1}$, still an order of magnitude smaller than the values derived above, and an amplitude of 10 ppbv day^{-1} in the diurnal O_3 cycle in the MBL has rarely been observed. It can also be seen from equation (3.2) that the entrainment rate is strongly dependent on the strength of the inversion and the mixing ratio increment over the inversion. It is therefore not very likely that the entrainment flux is constant, especially since numerous campaigns have shown that a wide range of ΔO_3 values can occur, sometimes even in the same area [Kawa and Person, 1989; Paluch *et al.*, 1995; Noone *et al.*, 1996]. The uncertainties involved in these calculations show that the “entrainment” approach, as an explanation for the diurnal O_3 cycle in the MBL, can be questioned.

The "entrainment" approach also provides a conceptual problem. Observations (Table 3.2) and models (Table 3.1) show that the daytime net photochemical destruction is counterbalanced by a nighttime increase. In the "entrainment" approach the O_3 mixing ratio increase is caused by transport of O_3 rich air from the free troposphere. Both observations and model results in Tables 3.1 and 3.2 refer to a fixed "Eulerian" frame. If, however, such an airmass were advected horizontally, and no net O_3 depletion would occur because of the balance between daytime net photochemical destruction and nighttime replenishment, downwind reduction of O_3 mixing ratios and horizontal O_3 gradients could not occur. This disagrees with numerous observations, which clearly indicate that horizontal O_3 gradients do exist in the MBL and that very low O_3 values occur regularly. The entrainment flux as an explanation of the observed diurnal O_3 cycle is therefore not satisfactory.

In this study an alternative explanation for the diurnal O_3 cycle under low NO_x conditions will be presented. This approach can explain why O_3 gradients and low O_3 mixing ratios exist in some parts of the MBL, and in section paragraph 3.2 results from the ECHAM4 model results will be compared with observations from an island site in the Indian Ocean. A conceptual model to explain the diurnal O_3 cycle will be presented in paragraph 3.3. The results from a case study are presented in paragraph 3.4, after which a discussion follows in paragraph 3.5. In addition to the standard model output, output generated on an hourly basis for the period of 16th March to 1st April 1995 will be used in this chapter.

3.2 Measurements

As part of the Indian Ocean Experiment (INDOEX), an observatory was established at the island of Kaashidhoo on the Maldives. This site is situated at 4.965ºN and 73.466ºE, and continuous measurements of several chemical species (e.g. O_3 and CO), aerosols and radiation have been performed since 1998. In this study we will take a closer look at the surface O_3 measurements performed during February-March 1998 when the First Field Phase (FFP) of the INDOEX campaign took place. Figure 3.1 shows the observed surface O_3 mixing ratios at Kaashidhoo and O_3 mixing ratios from the nudged ECHAM4 model at that site. The observations show that the O_3 mixing ratios range between roughly 15 and 30 ppbv with a superimposed diurnal cycle. The ECHAM4 model shows higher O_3 mixing ratios than observed, with an average difference of about 10 ppbv. De Laat *et al.* [1999] have discussed a similar offset over the Indian Ocean, based on shipborne O_3 measurements. The discrepancy is likely explained by (1) overestimation of O_3 formation by "artificial" NO_x transport by instantaneous mixing of emissions in the coarse (3.75º) grid cells of the model, and (2) underestimation of O_3 destruction through heterogeneous activation of reactive halogens from sea salt in the MBL [Vogt *et al.*, 1996; Dickerson *et al.*, 1999]

The model reproduces the general tendencies, e.g. maxima in O_3 mixing ratio around Day of Year (DOY) 53, between DOY 58 and 70 and around DOY 78 and minima around DOY 48, 53 and 72. This is not surprising considering the fact that the modeled and observed surface-wind speeds (Figure 3.2) and wind directions (not shown) agree very well. The discrepancy between the observed temporal O_3 change and the modeled O_3

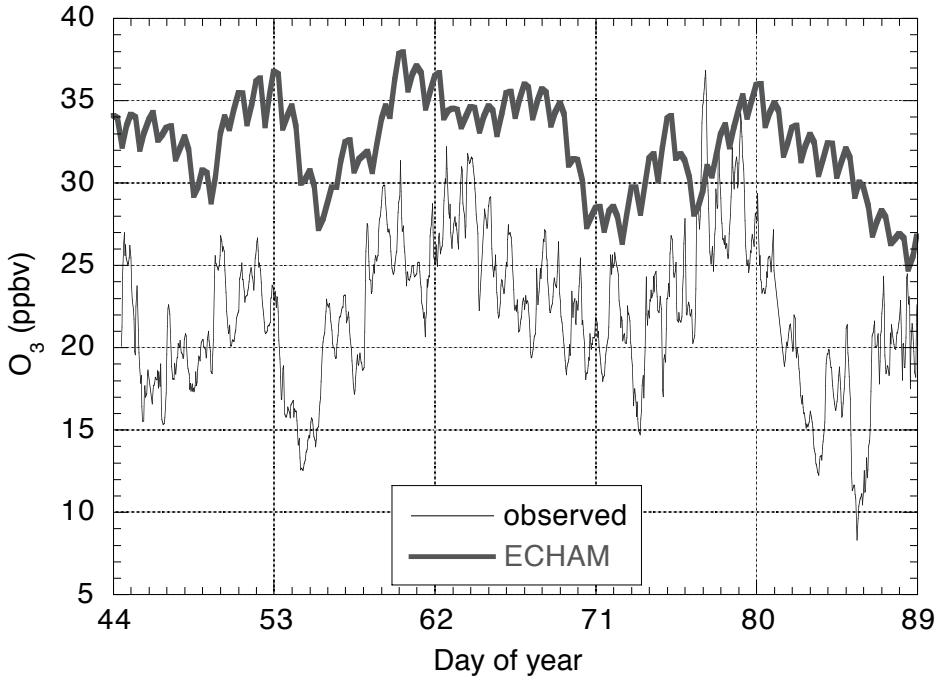

Figure 3.1: Observed and modeled O_3 mixing ratios during February and March 1998 at the Kaashidhoo surface observatory (4.965ºN and 73.466ºE) on the Maldives; O_3 mixing ratios in ppbv, time as Julian Days (DOY 44.5 = February 13, 12:00 UTC).

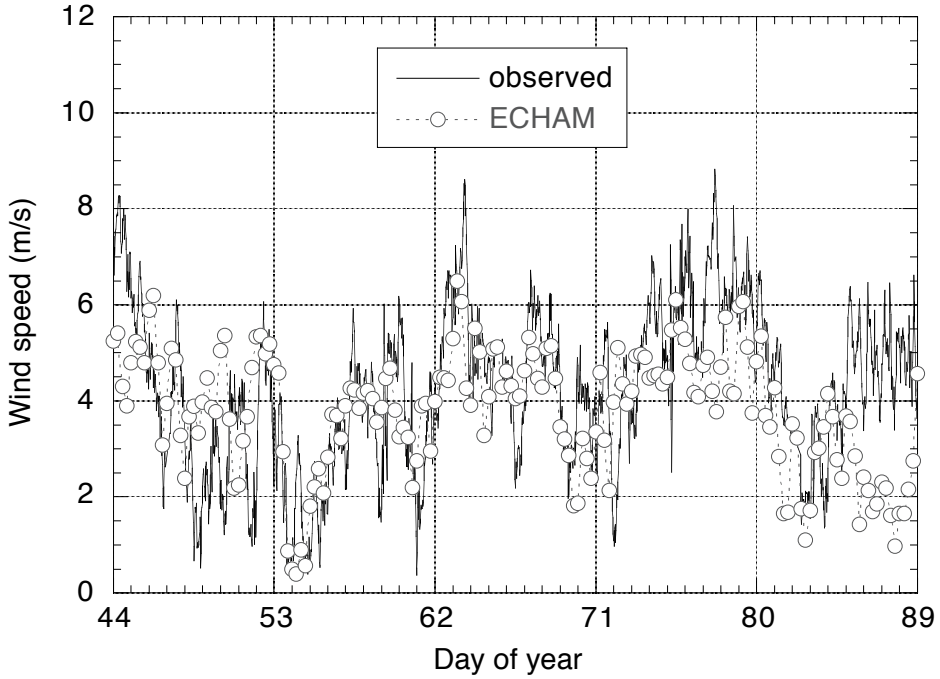

Figure 3.2 As Figure 3.1 but for the surface wind velocity.

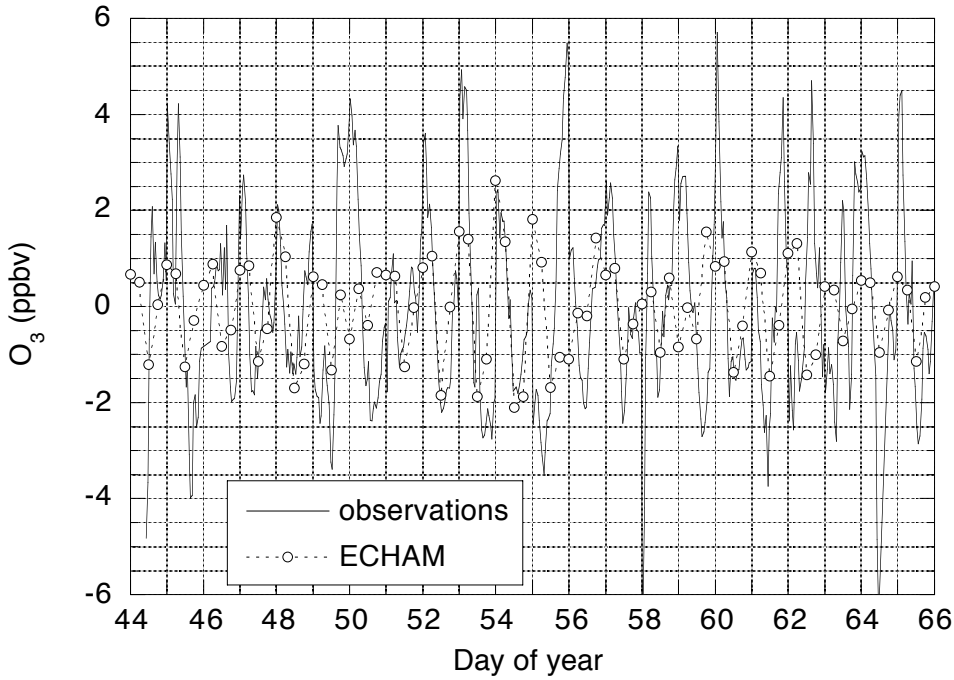

Figure 3.3a Diurnal O_3 cycle as observed at Kaashidhoo and from the ECHAM4 model for the period 13 February to 7 March (DOY 44 - 66) 1998. The Figure shows the difference between the actual mixing ratios and a 24-hour running mean. Mixing ratios in ppbv.

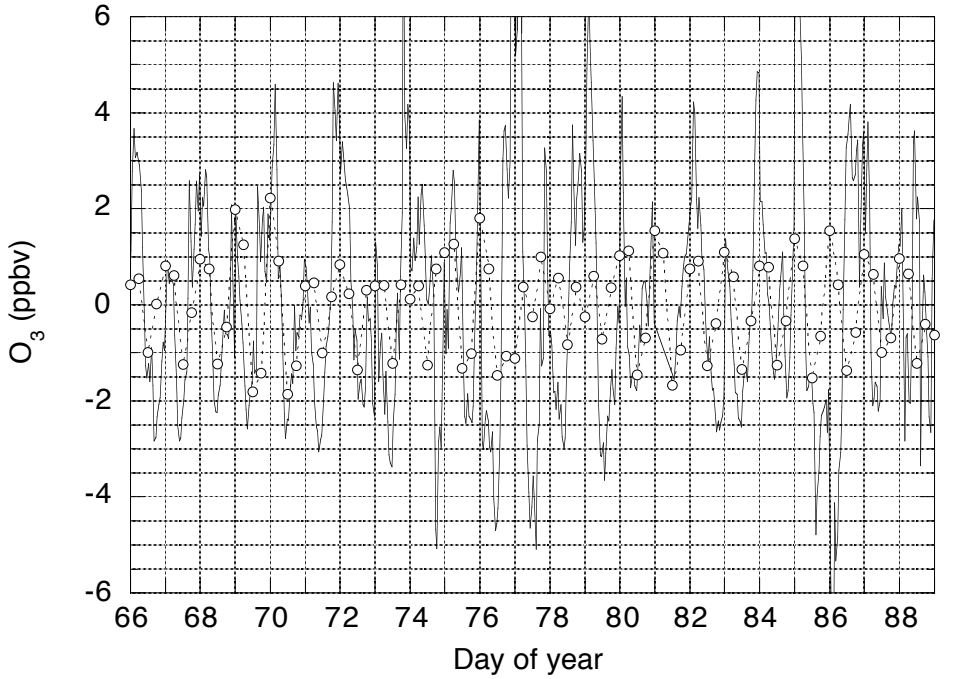

Figure 3. 3b As Figure 3.3a but for 7 March – 1 April (DOY 66 - 89) 1998.

one between DOY 80 and 88 are likely associated with differences between the observed and modeled wind speed and direction. In the model the winter monsoonal winds consistently originate from the northeast so that the airmasses travel over the southern tip of India and Sri Lanka towards Kaashidhoo. These areas are sources of O_3 precursors, thus counteracting the O_3 loss in the MBL. Therefore, the O_3 mixing ratios remain more or less constant. The observations, however, show west-northwesterly winds over this period, indicating a different origin of the airmass and thus a different chemical composition.

The diurnal O_3 cycles from both the observations and the model are shown in Figures 3.3a and 3.3b, where a running mean is calculated for both observations and model. Figures 3.3a and 3.3b show that the model produces a very similar diurnal O_3 cycle as seen in the observations, in spite of the ~ 10 ppbv offset in O_3 levels: a maximum mixing ratio at the end of the night and a minimum mixing ratio in the late afternoon. The model somewhat underestimates the amplitude of the diurnal cycle, although it should be considered that the model output was only available at 0, 6, 12, and 18 UTC, so that it is possible that not all the modeled peaks in O_3 are captured. The agreement between model and observations can be seen even better in Figure 3.4, which shows the daily averaged diurnal cycle from the running mean for both observations and model.

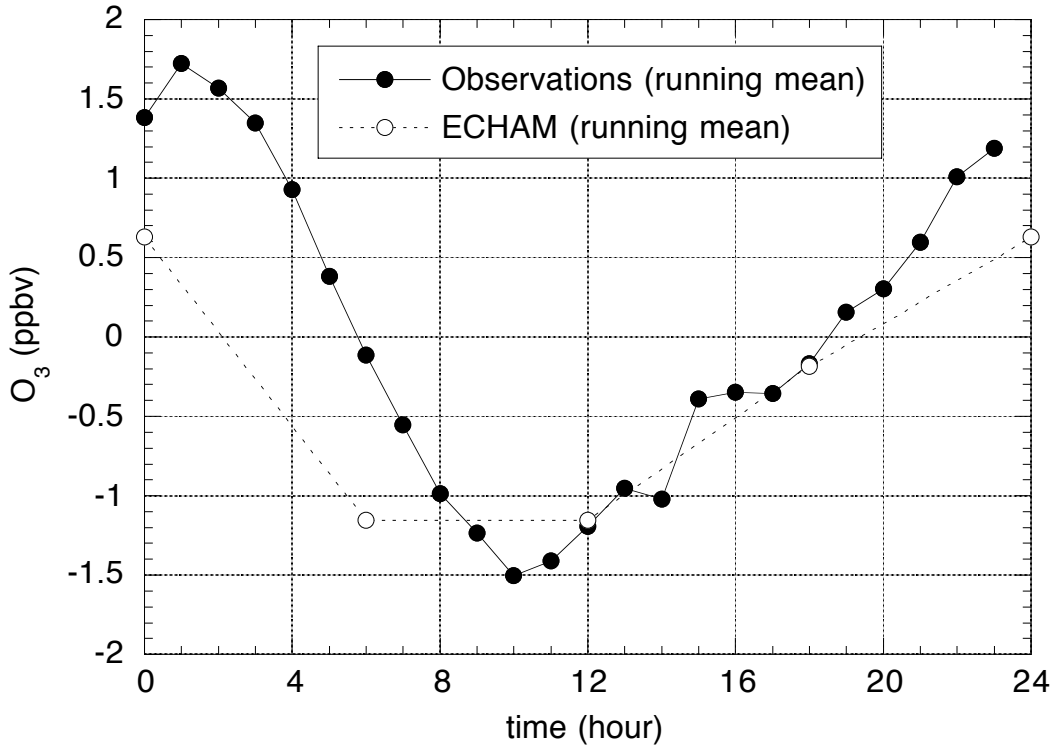

Figure 3.4 The averaged diurnal O_3 cycle for the period of 13 February to 1 April 1998, from the observations at the Kaashidhoo observatory and from the ECHAM4 model. Hours in UTC, local noon is at 07:00 UTC.

Considering that the ECHAM4 model has a vertical resolution of 19 layers, and the MBL is resolved by only 4 (5) layers (~ 30, 140, 380 and 780 (1480) meter altitude), the model is not capable of resolving a small scale process like the entrainment of free tropospheric air into the MBL. The possibility of the vertical diffusion parameterization being responsible for entraining free tropospheric air, and thus the diurnal cycle of O_3 in the model, can be ruled out. Figure 3.5 shows the O_3 mixing ratios at the five lowest ECHAM4 model levels for the period 17-23 March 1995 at 5.559ºN, 61.875ºE. This grid point is situated at the central Arabian Sea, and the temporal O_3 changes are typical for the modeled tropical MBL.

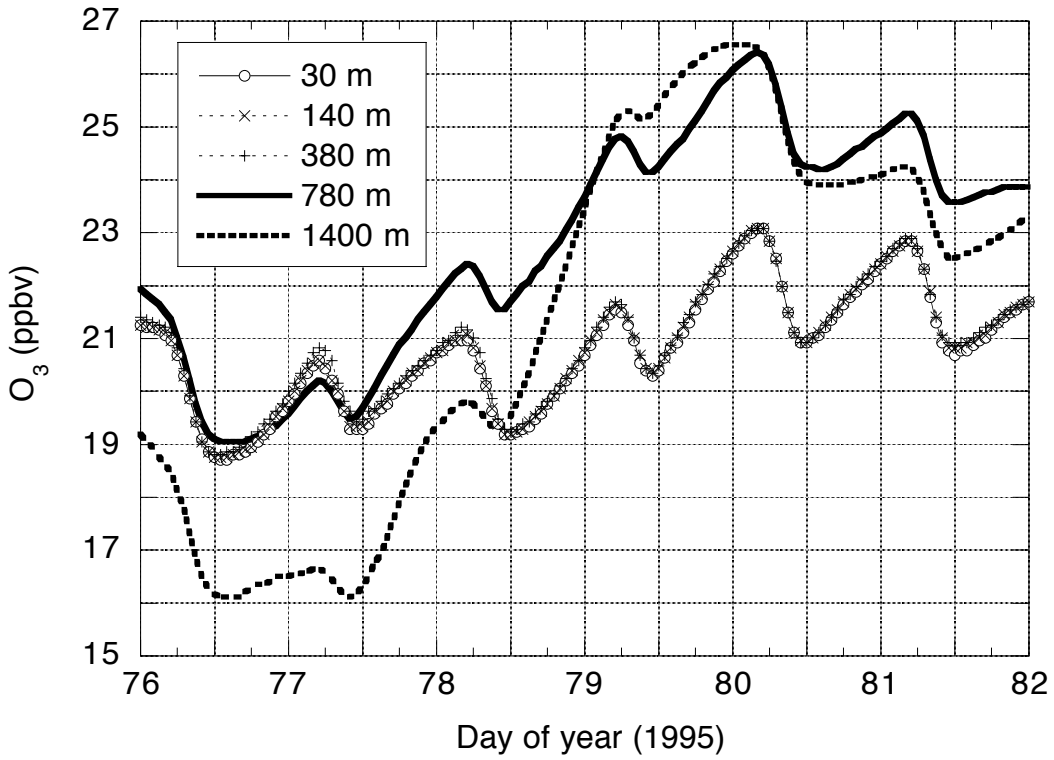

Figure 3.5 The modeled O_3 mixing ratio for the grid point at 5.559ºN, 61.875ºE for the period of 17 – 23 March 1995 (DOY 76 – 82) at the 5 lowest model levels. Hours in UTC, local noon is at 08:00 UTC.

The O_3 mixing ratios in the three lowest layers (up to 380 m) are the same and show a very distinct diurnal cycle (local time of sunrise is approximately 03:00 UTC). These 3 layers represent the MBL in the model. If vertical diffusion would be responsible for the downward transport of O_3, it can be expected that during DOY 76-78.5 a gradual decrease in O_3 would take place. Vertical mixing would bring air with lower O_3 mixing ratios into the boundary layer and O_3 would be photodissociated during daytime as well. Since such a gradual decrease is not discernable, the vertical diffusion can be assumed to be small. In fact, a small exchange between the MBL and the free troposphere is quite realistic. Due to the nearly constant surface temperatures over the ocean, the

dynamics of the MBL are much the same during night and day (contrary to the continental boundary layer, which shows a distinct diurnal cycle). The height of the MBL changes only very slowly in time, it shows no diurnal cycle and has a well-defined inversion [Garratt, 1992]. If vertical transport can be ruled out as an explanation for the diurnal O_3 cycle in the model, the question remains what is responsible. Below we will show that this is solely caused by horizontal transport.

3.3 1-Dimensional advection-diffusion equation

Consider an airmass being transported over sea in a NO_x-poor environment (lagrangian view). In the absence of vertical mixing, O_3 would remain constant during the night. During daytime O_3 would be depleted due to net photochemical destruction. Such a sequence will show up as step-wise changes in time: an O_3 decrease during the day and no change in O_3 mixing ratio during the night [e.g. Sander and Crutzen, 1996]. Turbulence in the boundary layer will moderate the step-wise O_3 decrease to a more gradual profile. This has been observed regularly in the MBL [Johnson *et al.*, 1990; Lal *et al.*, 1998], and a typical meridional O_3 gradient over the Indian Ocean is 1.5 ppbv deg^{-1} [Lal *et al.*, 1998]. Suppose that the airmass is transported with an average wind speed of 4 ms^{-1} (Figure 3.2). The airmass will travel 170-175 km (≈ 1.5°) in 12 hours. With an O_3 gradient of 1.5 ppbv deg^{-1} the O_3 level must be replenished by 2.25 ppbv during the 12 nighttime hours. Net photochemical destruction during daytime will then again lead to the depletion of O_3 so that the amplitude of the diurnal cycle is 1.125 ppbv for this example. According to Table 3.2, the observed amplitudes of the diurnal O_3 cycle agree well with this calculation. For an observer at a fixed point the O_3 changes would thus appear as a nighttime increase (transport) and daytime decrease (net photochemical loss).

The gradient causing the nighttime increase is directly related to the daytime depletion in O_3. A stronger decrease during the day would also lead to a larger horizontal O_3 gradient, and thus a sharper increase during the night. In this approach the daytime decrease will always be counteracted by the same nighttime increase. This hypothesis can be tested numerically by solving the 1-dimensional advection-diffusion equation:

$$\frac{\partial c}{\partial t} + u\frac{\partial c}{\partial x} - D\frac{\partial^2 c}{\partial x^2} = 0 \qquad (3.3)$$

In which c is a tracer mixing ratio, u is the average horizontal velocity and D is the diffusion coefficient. This equation describes the horizontal transport of a substance by the wind in the presence of horizontal diffusion. This is a good analogy for the horizontal transport of O_3, in which case diffusion is equivalent to boundary layer turbulence. The equation is solved with a Crank-Nicholson numerical scheme [Vreughdenhil, 1992]. The daytime depletion rate (amount of tracer depleted per second) is calculated as a $\cos^2$ function of time, and in such a manner that the total daytime depletion is roughly 3 mixing ratio units. At night no depletion is assumed. The model was run with a time step of 600 seconds and during 2000 time steps. The horizontal grid distance was 2500 m and the number of grid points was 1000. The average horizontal velocity was chosen at 4 ms^{-1}

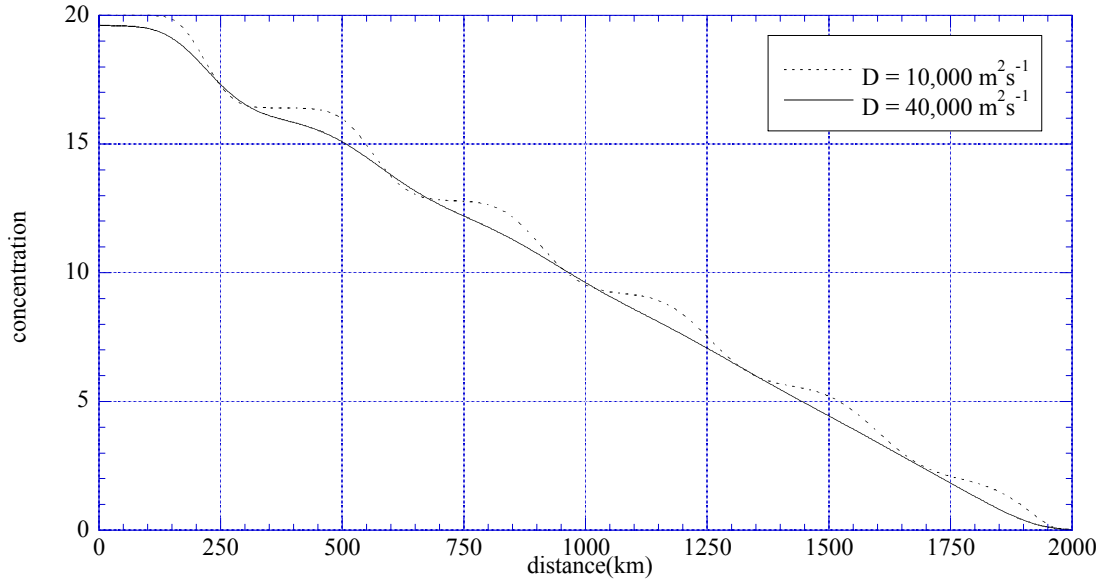

Figure 3.6: Tracer mixing ratio calculated from the 1-dimensional advection-diffusion equation for two different values of the diffusion parameter.

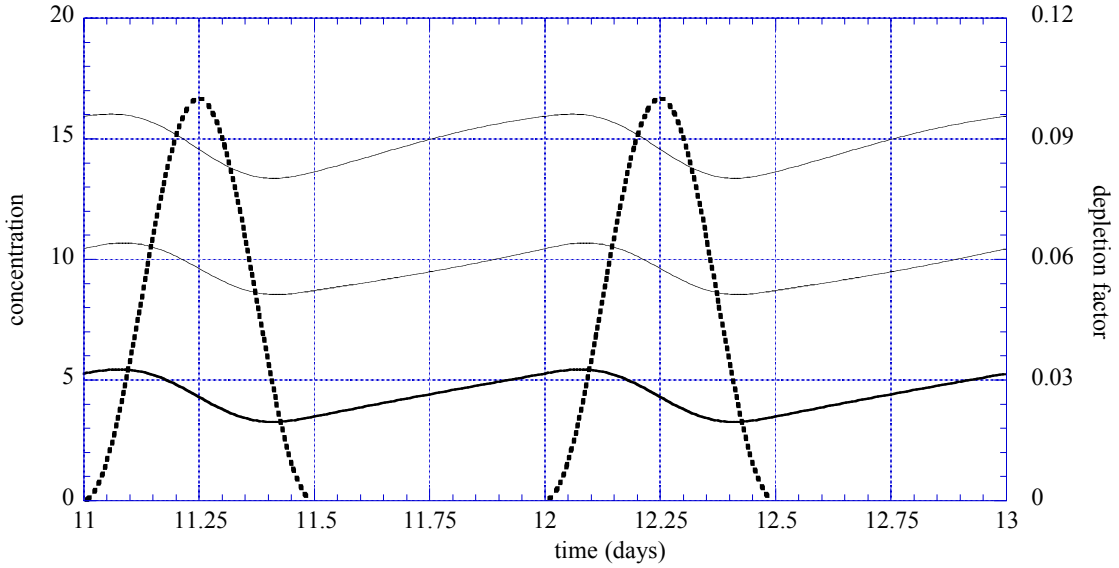

Figure 3.7: Mixing ratio (arbitrary units) as a function of time for the solution of the 1-dimensional advection-diffusion equation with D = 40,000 m^2s^{-1}. From top to bottom the mixing ratios are plotted (solid lines) at distances of 500, 1000 and 1500 km respectively, and the dotted line shows the depletion factor.

and the tracer mixing ratio at the boundary (x=0) was chosen at 20. It appears that the model reaches equilibrium within two days. Figure 3.6 shows the mixing ratio as a function of the distance for two different values of the diffusion coefficient after equilibrium is reached. For a relatively low diffusion coefficient the profile shows the step-wise changes, while for a higher value of the diffusion coefficient the profile shows a constant gradient. Observations show that O_3 gradients are quite smooth [Johnson *et al.*, 1990; Lal *et al.*, 1998], so that a small diffusion coefficient is probably not realistic.

Figure 3.7 shows the temporal mixing ratio changes for D = 40,000 m^2s^{-1} for different fixed points. The lowest mixing ratios appear during late afternoon after the maximum depletion rate, as expected. The mixing ratio at every grid point shows the same temporal behavior and the amplitude of the diurnal cycle is the same, because, in this example, the depletion rate is only a function of time and not of the mixing ratio of the tracer. Figure 3.7 thus shows a sharp daytime decrease and a gradual nighttime increase. This feature has often been observed [Oltmans, 1981; Ayers *et al.*, 1997; Lal *et al.*, 1998] and can also be seen in the ECHAM4 model results (Figure 3.5).

The amount of photochemical destroyed O_3 is, however, dependent on the O_3 mixing ratio itself. Numerical experiments in which the depletion rate is assumed to be dependent on the mixing ratio indeed show that the amplitude of the diurnal cycle decreases with decreasing mixing ratio, but the gradual increase in mixing ratio during the night and the rapid daytime decrease remain unchanged. These experiments also lead to the conclusion that in a lagrangian time frame, i.e. travelling with the airmass, the temporal O_3 profile shows step-wise decreasing values. This can be seen in Figure 3.8, which shows the tracer mixing ratio when travelling with the airmass.

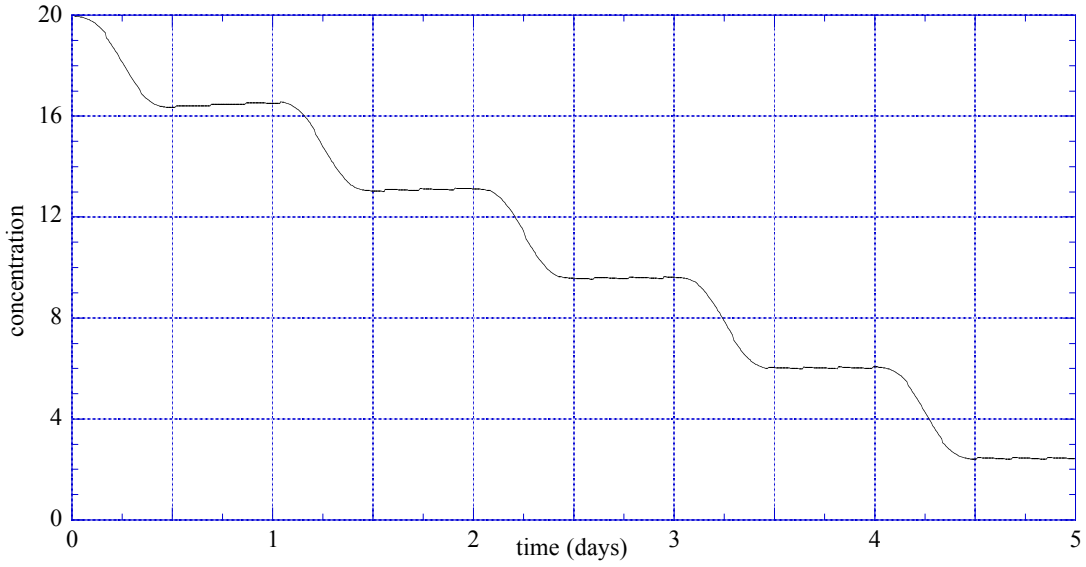

Figure 3.8 Mixing ratio of a tracer calculated from the 1-dimensional advection-diffusion equation when travelling with the airmass (Lagrangian experiment).

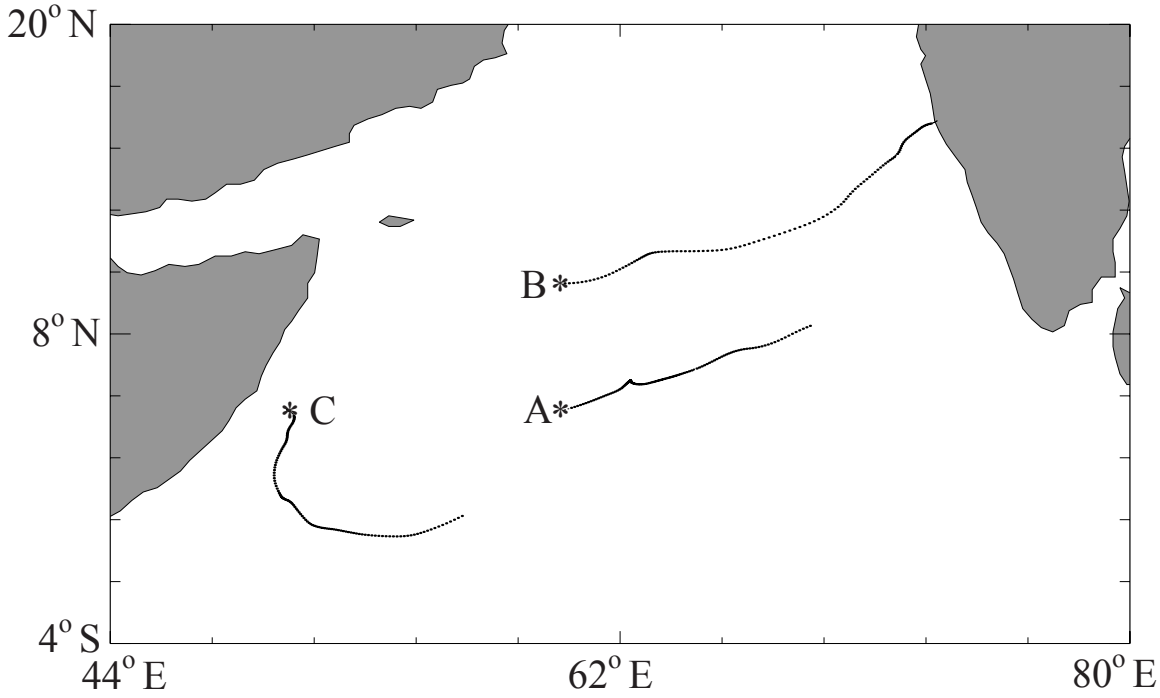

Figure 3.9a Horizontal position of three 5-day back-trajectories calculated from the ECHAM4 model output. Trajectories were started on 25 March 1995 at 12:00 UTC (DOY 84.5), at an altitude of 950 hPa, at 60ºE, 5ºN (trajectory A), 60ºE, 10ºN (trajectory B) and 50ºE, 5ºN (trajectory C).

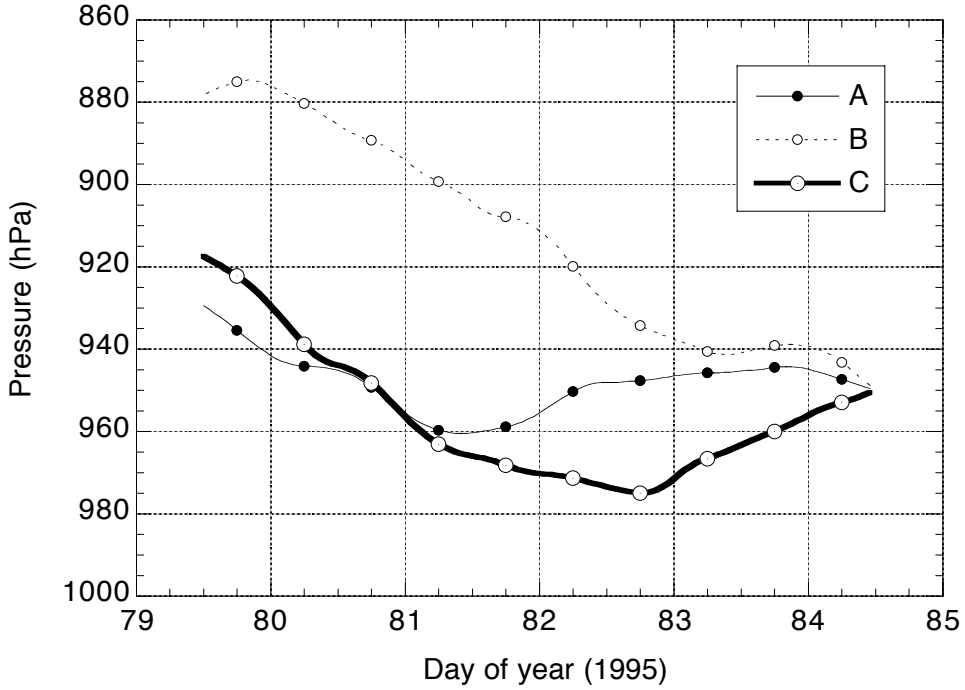

Figure 3.9b Vertical displacements of the back-trajectories shown in Figure 3.9a

3.4 Results from the ECHAM4 model

To compare the lagrangian behavior of O_3 in the ECHAM4 model with the 1-D advection-diffusion concept, a trajectory model was used to monitor the O_3 during transport. The trajectory model was applied to the 3-D ECHAM4 wind fields. The wind fields were updated every 6 hours. A fourth-order Runge-Kutta scheme was used to advect a set of points in 3-D space, and the wind velocities were linearly interpolated for the parcel in both space and time. The time step used for the trajectory calculations was 30 minutes. Time and location of the trajectories were subsequently used to retrieve 1-hourly fields along the trajectories. Figure 3.9a shows the position of three 5-day back-trajectories starting on 25 March 1995 at 12:00 UTC at an altitude of 950 hPa. The trajectories A and B clearly follow the northeasterly flow over the Arabian Sea. Figure 3.9b shows the vertical displacements. The trajectories A and C remain in the lowest levels of the MBL most of the time, while trajectory C originates from a higher altitude, although still close to the top of the MBL.

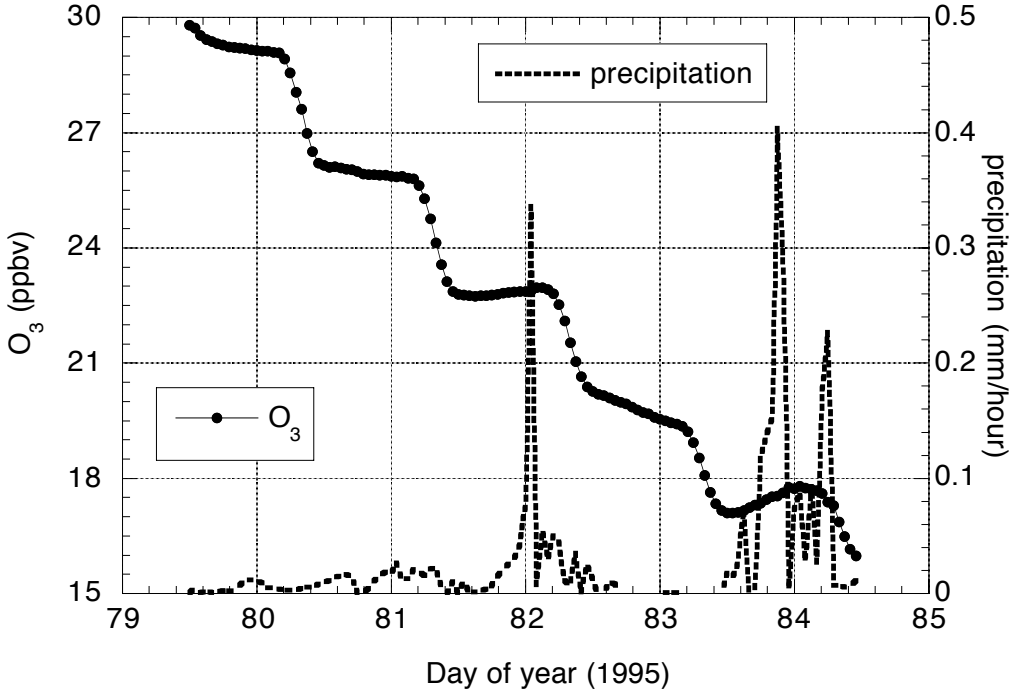

Figure 3.9c: O_3 mixing ratios and the precipitation rates along back-trajectory A, as calculated with the ECHAM4 model.

Figure 3.9c shows O_3 and the precipitation rate along trajectory A. The O_3 mixing ratio shows the step-wise changes as predicted. Calculated NO_x mixing ratios varied between 24 and 40 pptv, in the net O_3 destruction regime. The small increases in O_3 around DOY 82 and DOY 84 are related to convective precipitation in the model. The precipitating clouds in the model are associated with mixing of boundary layer air with

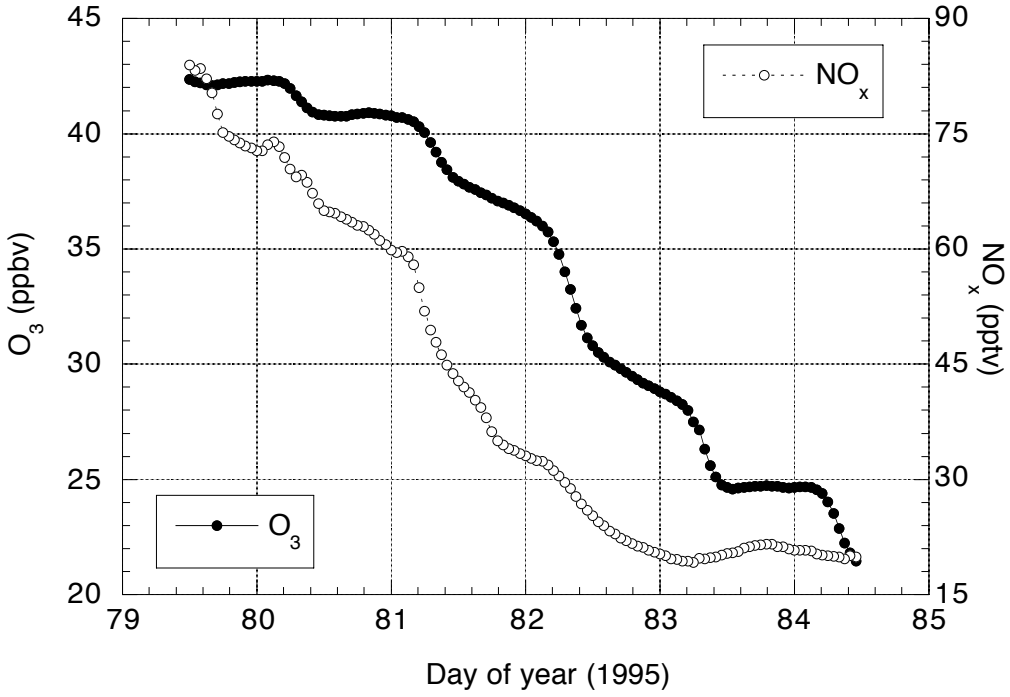

Figure 3.9d O_3 and NO_x mixing ratios along back-trajectory B, as calculated with the ECHAM4 model.

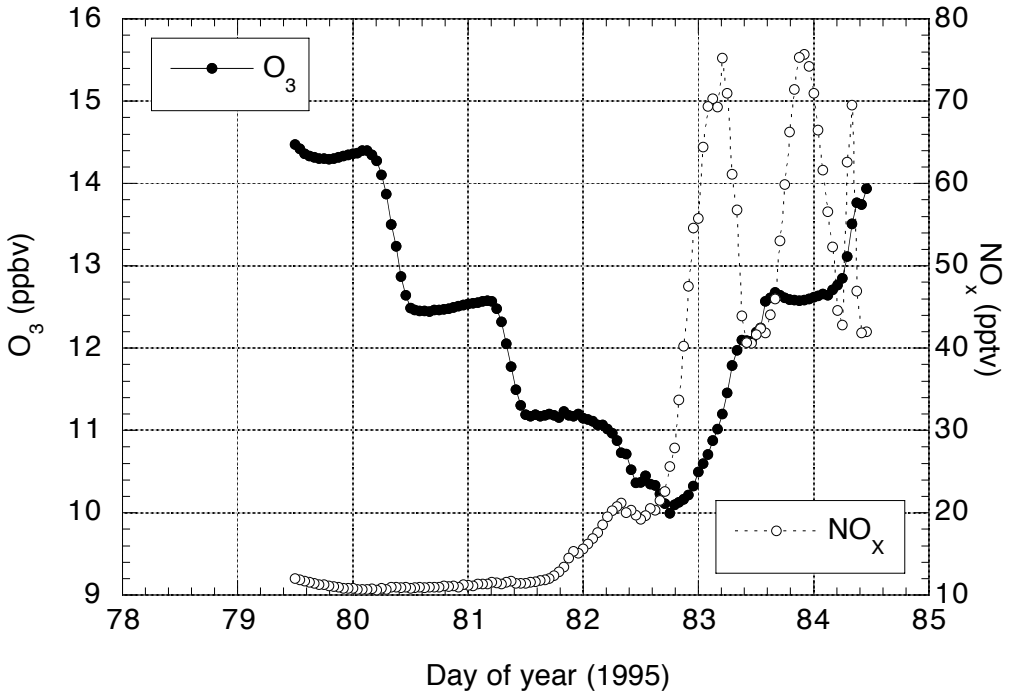

Figure 3.9e: As Figure 3.9d but for back-trajectory C.

air from aloft which, in this case, had a higher O_3 mixing ratio. This step-wise O_3 decrease is typical for model output in areas remote from NO_x sources, so that NO_x mixing ratios are well below the net O_3 production limit and the airmasses are subject to net O_3 loss at least a few days. In such cases almost all the O_3 increases along the trajectories are related to convection in the model [Lelieveld and Crutzen, 1994].

Figure 3.9d shows the mixing ratios of O_3 and NO_x along trajectory B. Again, the step-wise changes in O_3 are evident. As can bee seen in Figure 3.9a, this trajectory starts close to the Indian subcontinent where pollutants are emitted. This explains the relatively high NO_x mixing ratios at the start of the trajectory. The rates of O_3 changes in this case are different compared to trajectory A. Between DOY 79.5 and 81.5 the net O_3 destruction is small. The mixing ratios of NO_x are close to the net O_3 production limit so that relatively little O_3 is lost during daytime compared to the total O_3 mixing ratios.

Between DOY 81.5 and 83.5 the daytime O_3 loss increases as NO_x is depleted to about 16-17 pptv. During this period the O_3 mixing ratio also decreases during the night, caused by the reaction between O_3 and NO_2, heterogeneous removal of N_2O_5 and dry deposition of O_3 and HNO_3. An observer at a fixed point would see a relatively large amplitude in the diurnal O_3 cycle. Note that much of the variability in NO_x removal and net O_3 destruction is associated with (broken) clouds fields that (enhance) reduce photodissociation frequencies.

Figure 3.9e shows the NO_x mixing ratios along trajectory C. In this case the airmass moved from the Arabian Sea towards and along the African east coast. During the first three days the air is still moving away from the Indian O_3 source region. NO_x mixing ratios are low throughout the first three days, and O_3 shows the typical step-wise decrease. After DOY 82 the airmass approaches the African coast and mixes with more polluted air. NO_x mixing ratios increase rapidly, and O_3 increases due to advection and local photochemical formation.

3.5 Summary and discussion

The model calculations show that the combination of horizontal advection, daytime net photochemical O_3 destruction and horizontal mixing cause a distinct diurnal O_3 cycle in the tropical MBL. The mechanisms can be summarized as follows:

1. If NO_x mixing ratios exceed 50-100 pptv, net photochemical O_3 formation takes place, and the diurnal O_3 cycle shows a minimum at the end of the night and a maximum during late afternoon. This agrees, for example, with observations at Cape Grim (Tasmania) by Ayers *et al.* (1997), whose measurements were partially performed in relatively polluted air that was transported towards Cape Grim from the Australian continent.
2. If O_3 and NO_x mixing ratios are relatively high, but NO_x mixing ratios are below the net photochemical O_3 destruction regime, O_3 mixing ratios show a decrease during daytime, whereas during nighttime additional O_3 depletion can occur due heterogeneous removal of O_3 and NO_2 through N_2O_5. This also means that, due to the stronger horizontal O_3 gradient, the amplitude of the observed diurnal O_3 cycle is relatively large. This agrees with observations by Anderson *et al.* [1993] close to the polluted Brazllian coast, who

measured amplitudes in the diurnal cycle between 2.75 and 4 ppbv (associated with a net O_3 destruction rate of about 8 ppbv day^{-1}). The measurements were performed in airmasses affected by biomass burning emissions of O_3 precursors (O_3 mixing ratios between 30 and 70 ppbv), thus showing large amplitudes in the diurnal O_3 cycle. The other campaigns listed in Table 3.2 indicate smaller diurnal O_3 cycles because the measurements were performed remote from pollution sources.

3. If both NO_x and O_3 mixing ratios are relatively low, which is the case for much of the MBL, net photochemical O_3 destruction prevails during daytime. The diurnal O_3 cycle is also related to the intensity of sunlight. Oltmans [1981] showed that in Barrow, northern Canada (~ 70ºN), the diurnal O_3 cycle is much smaller than at Samoa (14ºS), associated with the much lower insolation at Barrow. Ayers *et al.* [1997] showed that at Cape Grim (41ºS) the diurnal O_3 cycle in summer is much larger than in winter. Our hypothesis implicates that a possible difference between the summer and wintertime boundary layer entrainment flux of O_3, as suggested by Ayers *et al.* [1997], is not necessary to explain the observed diurnal O_3 cycles.

Anderson *et al.* [1993] showed that, on average, the nighttime mixing ratios of O_3 in the boundary layer are higher than the daytime mixing ratios, and that the differences are uniformly distributed over the entire boundary layer. This is an important observation because Vilà-Guerau de Arellano and Duynkerke [1999] demonstrated that, if chemical species are entrained from the free troposphere, the mixing ratio differences in time should be higher close to the top of the boundary layer than close to the surface.

To further illustrate the different regimes, Figure 3.10 shows a global view of the diurnal O_3 cycle amplitude at the surface for the latter half of March, derived from the ECHAM4 model. The amplitude is larger and much more variable in the continental boundary layer (not shown) than in the MBL. This is related to the larger NO_x mixing ratios over land, which causes net O_3 production during daytime. The amplitude of the diurnal O_3 cycle over the ocean does not show such high variability, in line with the findings from the different campaigns listed in Table 3.2. Furthermore, over the oceans as well as over land the maximum amplitudes occur in areas with the highest insolation. These "bands" stretch zonally between 20ºN and 20ºS. The maximum amplitudes of the diurnal O_3 cycle in the MBL appear in areas where the average wind direction is offshore, e.g. the Indian west-coast, the Australian and Indonesian west coasts, the African west-coast and the west-coasts of central and southern America. This is related to the relatively high O_3 mixing ratios in net O_3 destruction environments.

Figure 3.11 shows that the largest gradients in O_3 mixing ratio gradients are found in a latitudinal band between the Equator and 15ºN, also the area where the largest diurnal O_3 cycle amplitudes occur. In the ITCZ over the Indian and Pacific Oceans, where O_3 mixing ratios reach minimum values, the diurnal O_3 cycle shows the smallest amplitude. Over the tropical Atlantic Ocean the O_3 mixing ratios do not reach values as low as those over the Indian and Pacific Oceans. Figure 3.12 shows the local time of the maximum in the diurnal O_3 cycle for the same period, as simulated by the ECHAM4 model. The marine regions show a maximum around sunrise, typical for net O_3 destruction regimes, and the local time of the maximum is very uniformly distributed. Over landmasses the maximum occurs during the day and over a wider range of local times, although always during daytime, typical for net O_3 production regimes.

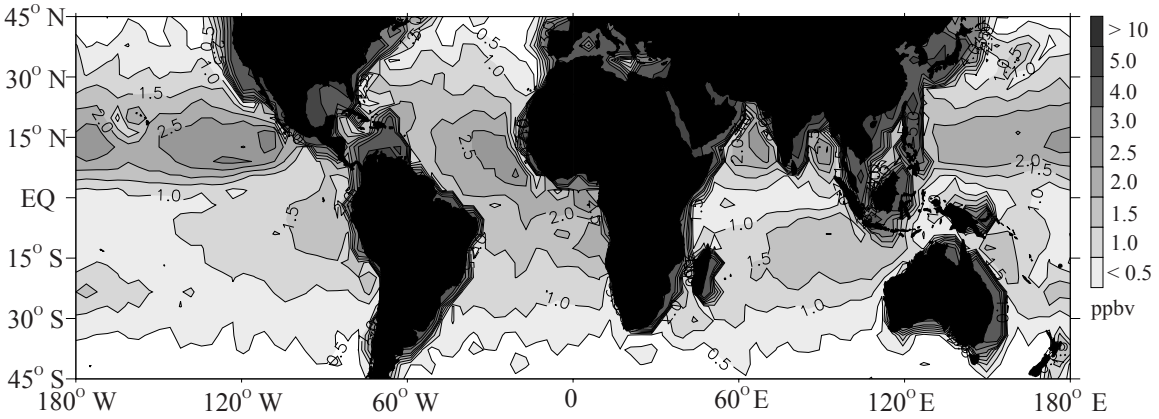

Figure 3.10 The average amplitude of the diurnal O_3 cycle at the surface over the globe, calculated by the ECHAM4 model for the period of 17 – 31 March 1995.

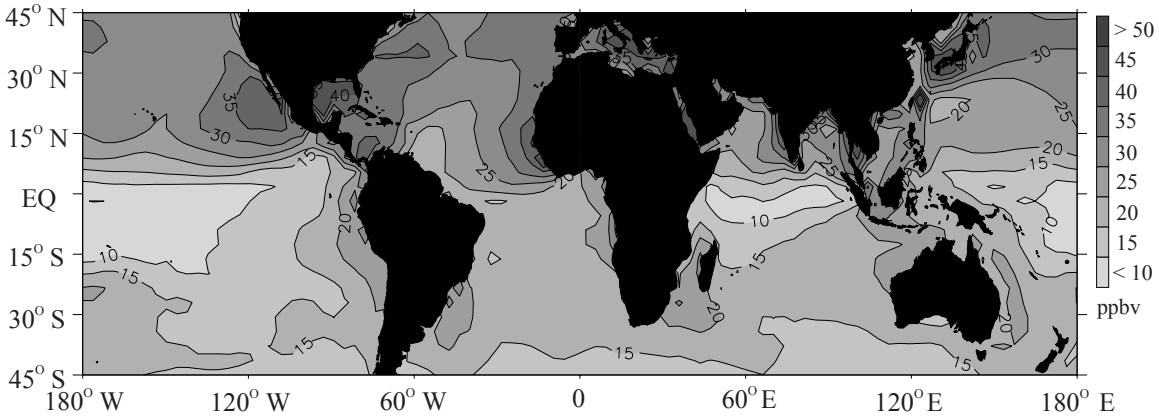

Figure 3.11 The average O_3 mixing ratio at the surface over the globe from the ECHAM4 model, averaged for the period of 17-31 March 1995. For convenience the O_3 mixing ratios over landmasses have not been included.

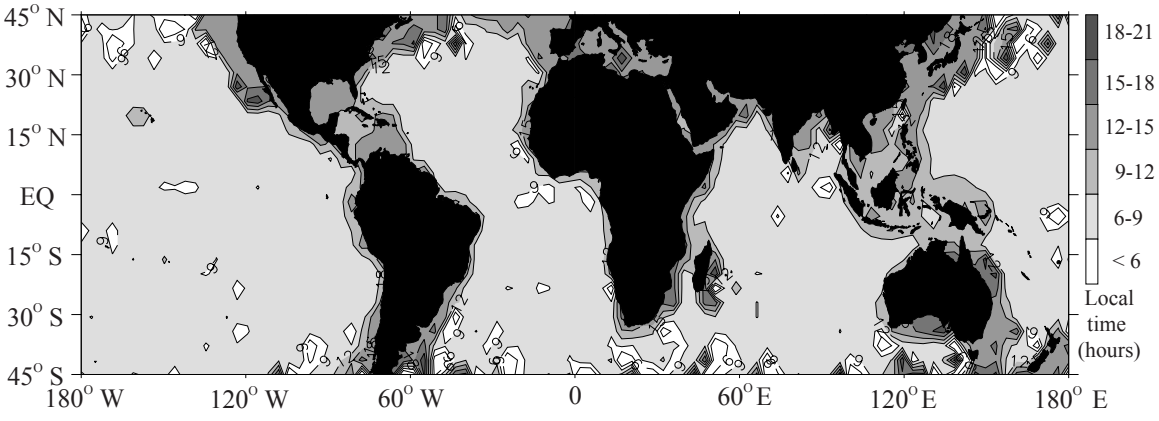

Figure 3.12 The local time at which the maximum amplitude in the diurnal cycle in O_3 appeared in the ECHAM4 model between 45ºN and 45ºS, averaged for the period of 17-31 March 1995.

This conceptual mechanism has several other implications. It explains the diurnal cycle for species, which have a relatively long lifetime (more than a few days) and which do not have an oceanic source. However, it does not describe the diurnal cycle of species with an oceanic source and/or very short lifetimes. This mechanism also implies that the often observed very low O_3 mixing ratios (< 5 ppbv) over marine regions, especially over the Pacific Ocean [Routhier *et al.*, 1980; Johnson *et al.*, 1990; Thompson *et al.*, 1993; Kley *et al.*, 1996], can be the result of airmasses having traveled and aged without interaction with more polluted airmasses from either the continents or from the free troposphere.

Although we propose that the entrainment process is not the main mechanism responsible for the observed diurnal cycle in O_3, entrainment of free tropospheric air into the boundary layer will have additional effects. The exact contribution of entrainment is, however, strongly dependent on the local conditions, for example the strength of the inversion and the O_3 mixing ratios in the free troposphere. Some observations of entrainment velocities in stratocumulus show an increase [de Roode and Duynkerke, 1997]. Other observations, however, do not show such an increase at all [Kawa and Pearson, 1989]. In general, the range of observed entrainment velocities is large and the methodologies used are associated with uncertainties. Entrainment in stratocumulus can lead to the breakup of the cloud layer [Duynkerke, 1993], after which entrainment velocities decrease.

3.6 Conclusions

It is shown that horizontal transport and photochemical processes explain the typical diurnal O_3 cycle in the MBL (nighttime maximum and daytime minimum). In this mechanism the daytime decrease and nighttime increase are closely related. Daytime net photochemical O_3 destruction in combination with horizontal advection and diffusion (due to turbulence) creates a gradual decrease (gradient) in O_3 from the source regions. Such a gradual decrease has been observed regularly, for example, over the Pacific and Indian Oceans [Johnson *et al.*, 1993; Lal *et al.*, 1998]. This gradient causes the nighttime increase because air with higher O_3 mixing ratios is advected to regions with lower O_3 mixing ratios. In this approach the daytime decrease will always be counteracted by the nighttime increase. The daytime depletion rate is thus a measure for the amplitude of the diurnal O_3 cycle. Although the horizontal advection of airmasses with higher O_3 mixing ratios continues during daytime, net photochemical O_3 destruction dominates the daytime O_3 tendency. As the daytime depletion is controlled by insolation, the amplitude of the diurnal O_3 cycle is very similar in most tropical marine regions. This is confirmed by the available observations (Table 3.2). This mechanism also implies that the amplitude of the diurnal O_3 cycle is larger close to NO_x emission regions because the O_3 mixing ratios are higher and net photochemical loss takes place at a higher rate, in agreement with observations [Anderson *et al.*, 1993].

Finally we note that for MBL simulations of O_3 with a box model it is not relevant whether the mechanism that causes the diurnal O_3 cycle is entrainment of free tropospheric air (often assumed previously) or horizontal advection in conditions with

photochemical O_3 loss (posed here). Both approaches have the same result: O_3 is transported from an area with higher O_3 mixing ratios. Conclusion from studies in which box models have been used to explain the chemistry in the MBL are therefore not less valid, however, the physical mechanism behind the O_3 influx is different.

Chapter 4

Source analysis of carbon monoxide pollution during INDOEX 1999

Abstract.

A source analysis of carbon monoxide (CO) over the Indian Ocean is presented using marked tracers in a chemistry general circulation model. The model, which includes a non-methane hydrocarbon (NMHC) chemistry scheme, has been used at two different resolutions (3.75° × 3.75° and 1.9° × 1.9 °). European Centre for Medium-range Weather Forecasts (ECMWF) meteorological analyses have been assimilated into the model to represent actual meteorology during February and March of 1999. A comparison with measurements indicates that the model simulates realistic CO distributions, except towards the Indian coast near the surface. This may be related to a sea breeze circulation at the Indian west coast, not resolved by the model. The sea breeze can act as a barrier for transport of polluted air masses from the continent to the marine boundary layer. Instead, pollution is transported to altitudes directly above the boundary layer. These pollution layers have also been observed in O_3 soundings and aerosol measurements. The marked tracer study suggests that biofuel use and agricultural waste burning in India are major CO sources for the INDOEX-region, with minor contributions from Middle East, China and South East Asia. In the much cleaner boundary layer over the southern Indian Ocean, CO from hydrocarbon oxidation is a dominant source. In general, most of the Asian CO over the Indian Ocean remains north of the Inter-Tropical Convergence Zone (ITCZ), although some of the CO is transported into the southern hemisphere in the free troposphere near the African east coast.

Submitted to *Journal of Geophysical Research, 2000*, with co-authors R. Dickerson, J. Lelieveld, J. Lobert and G.J. Roelofs.

4.1 Introduction.

Carbon monoxide is an important trace gas in global atmospheric chemistry since its oxidation is the main sink of OH radicals [Crutzen, 1988]. However, in the presence of nitrogen oxides (NO_x = NO + NO_2), its oxidation is associated with OH regeneration and O_3 formation. The latter contributes importantly to air quality degradation in photochemical smog and, on a global scale, to a radiative forcing of climate [IPCC, 1994; WMO, 1998]. CO is formed by photochemical breakdown of methane and higher hydrocarbons, and is directly emitted by combustion processes. Fossil fuel combustion is the dominant CO source at middle and high northern latitudes, whereas biofuel use and biomass burning are major sources in tropical areas (see Table 4.1).

No.	Area	Source type	Code	Emission (Tg CO yr^{-1})	Fraction (%)
1	North America	FF	NAM-FF	79.2	8.1
	North America	BB	NAM-BB	32.6	3.4
2	South America	FF	SAM-FF	20.0	2.1
	South America	BB	SAM-BB	122.3	12.6
3	Europe	FF	EUR-FF	64.2	6.6
	Europe	BB	EUR-BB	30.0	3.1
4	Africa	FF	AFR-FF	7.5	.8
	Africa	BB	AFR-BB	227.3	23.3
5	Arabia	FF	ARA-FF	10.4	1.1
	Arabia	BB	ARA-BB	27.2	2.8
6	India	FF	IDA-FF	3.3	.3
	India	BB	IDA-BB	73.0	7.5
7	Russia	FF	GOS-FF	48.6	5.0
	Russia	BB	GOS-BB	35.9	3.7
8	Japan	FF	JAP-FF	17.5	1.8
	Japan	BB	JAP-BB	4.9	.5
9	South-East Asia	FF	SEA-FF	2.5	.2
	South-East Asia	BB	SEA-BB	28.0	2.9
10	China	FF	CHI-FF	32.2	3.3
	China	BB	CHI-BB	59.0	6.1
11	Indonesia	FF	IND-FF	6.5	.7
	Indonesia	BB	IND-BB	34.6	3.6
12	Australia	FF	AUS-FF	4.3	.4
	Australia	BB	AUS-BB	2.4	.2
All	World	FF+BB	TOT	973.8	100.0

Table 4.1 CO source regions and strengths as defined in the model and their fractional contributions to total CO emissions. BB is biofuel use and biomass burning, FF is fossil fuel use. Values derived from the EDGAR v.20 emission inventory [Olivier *et al.*, 1996].

Because of the fairly long lifetime of CO (a few weeks in the boundary layer to several months in the free troposphere), and because CO removal by precipitation and dissolution in the oceans is negligible, CO is an ideal tracer to study the global transport of atmospheric pollution. However, the large number of possible sources in combination with the long photochemical lifetime of CO render it difficult to determine the exact origin of CO when measured. Trajectory analyses only provide limited information because the period for which trajectories are reliable is only a few days, which is much shorter than the average transport and lifetime of CO. To address this problem, model simulations with a chemistry general circulation model (GCM) were performed in which CO has been marked according to several source categories and regions. The model results are used to give an overview of the contribution of the different sources on global and regional scales. They are also compared to in situ CO observations, as obtained from the Indian Ocean Experiment (INDOEX) during February and March 1999, to provide detailed information about the relative contribution of the different sources. This comparison also provides valuable indications about the representation of emissions and atmospheric processes in the model and how these could be improved.

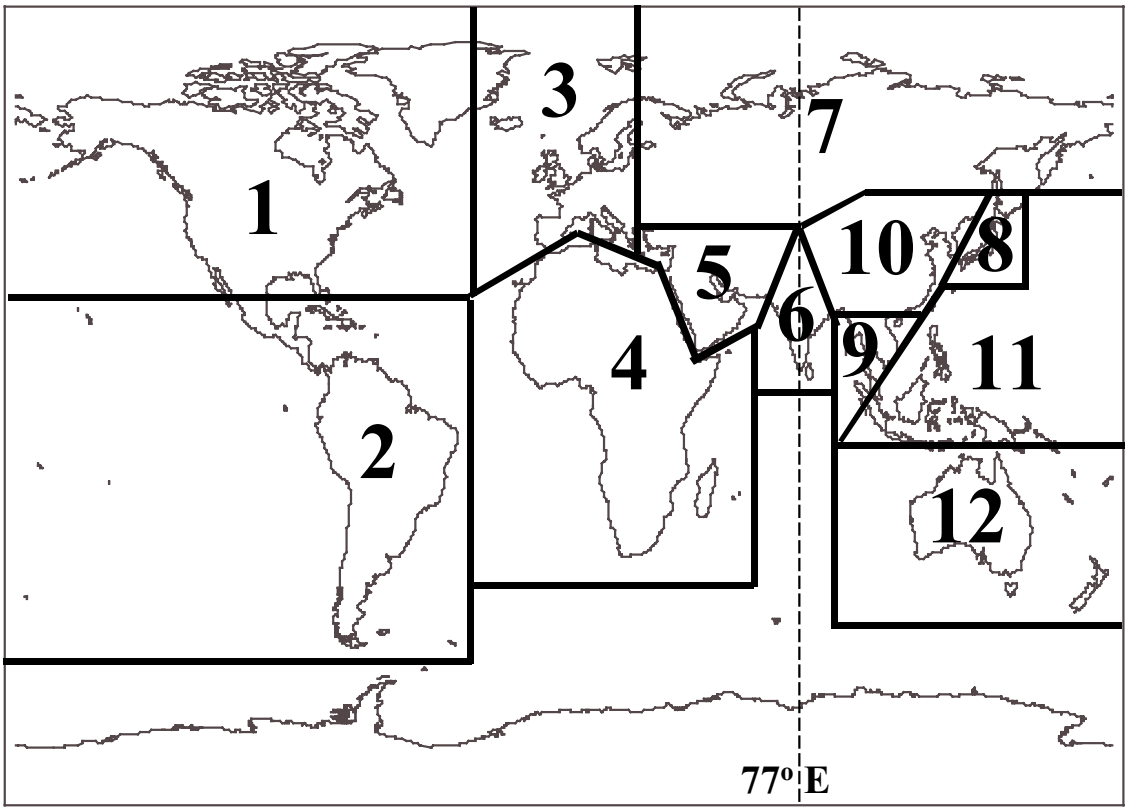

Figure 4.1 Twelve different CO source regions as distinguished in the model.

4.2 Model description

In chapter 2 and 3 the ECHAM4 model was coupled to a background tropospheric chemistry model [Roelofs and Lelieveld, 1995; 1997]. In this chapter the model uses a NMHC chemistry scheme. A more detailed description of this model version can be found in the appendix.

To investigate the effects of different sources on regional and global CO distributions, in particular those over the Indian Ocean during INDOEX, 24 additional tracers were included in the model. The emission of these tracers are derived from the EDGAR v2.0 emission inventory [Olivier, 1996]. Owing to computational constraints this model version was only used at T30 resolution. The CO emissions are subdivided into emissions from fossil fuel use (~ 30 % of the global CO emissions, hereafter referred to as "FF-CO") and from biofuel use and biomass burning (~ 70 % of the global CO emissions, hereafter referred to as "BB-CO"). The global source distribution distinguishes 12 regions, shown in Figure 4.1. The global annual BB-CO and FF-CO emissions for the different regions are given in Table 4.1, as well as the corresponding abbreviations that are used in several figures. One tracer is used for the total global sum of BB-CO+FF-CO. CO from hydrocarbon oxidation will be calculated as the difference between the total global sum of BB-CO+FF-CO and model calculated CO.

4.3 Comparison between observed vertical CO profiles and ECHAM4 model output.

During the Intensive Field Phase (IFP) of INDOEX, a Cessna Citation aircraft obtained vertical profiles of CO over the Indian Ocean [De Gouw *et al.*, 2001]. A comparison of 8 of these profiles with ECHAM4 output at both T30 and T63 resolution is displayed in Figure 4.2. Apart from the horizontal resolution, both model versions are identical. We generally obtained good agreement between observed and modeled CO profiles, and even some of the smaller observed features were reproduced in the model results.

Most tropospheric profiles show a typical "C"-shape with high surface mixing ratios associated with advection of polluted continental air masses, lower mixing ratios between 3 and 8 km altitude and elevated mixing ratios between 8 and 12 km, which are associated with convection, ventilating polluted boundary layer air to higher altitudes [Dickerson *et al.*, 1987]. Profile 2^e is an exception, in which CO mixing ratios in the boundary layer are lower than aloft, representing clean southern hemispheric air in the boundary layer [Williams *et al.*, 2001]. In this case CO increases with increasing altitude, reflecting the longer lifetime of CO at higher altitudes due to lower OH (lower water vapor) and higher insolation.

In general, the modeled CO mixing ratios in the free troposphere are in agreement with the observations. However, the model does not always reproduce the measured CO mixing ratios in the boundary layer, especially at T30 resolution. At the T63

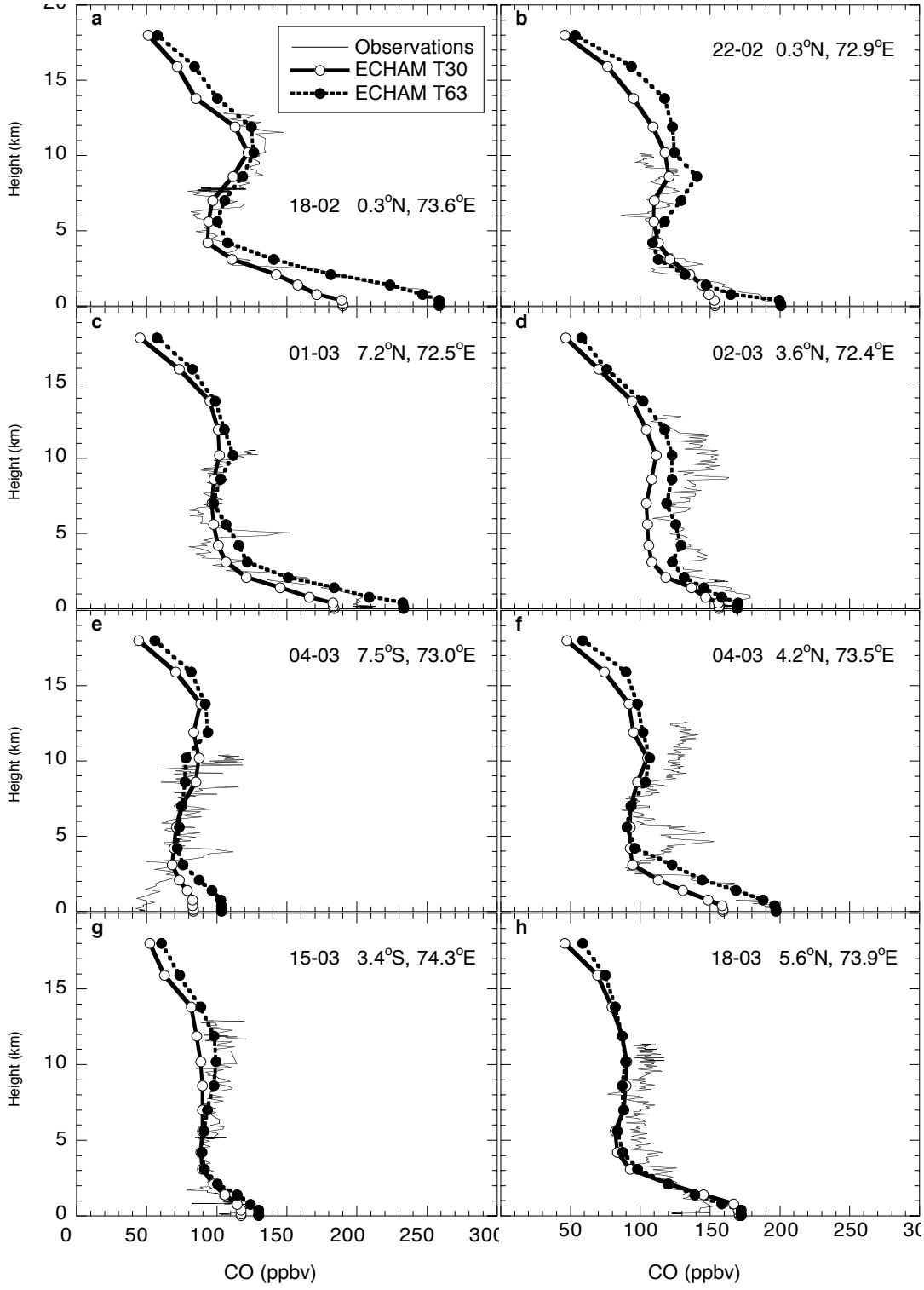

Figure 4.2 Comparison between eight vertical CO profiles observed from the Cessna Citation aircraft and modeled CO profiles. The thin solid line denotes the observations, the thick solid lines/open circles are model results at T30 resolution and the thick dashed lines/black circles are model results at T63 resolution.

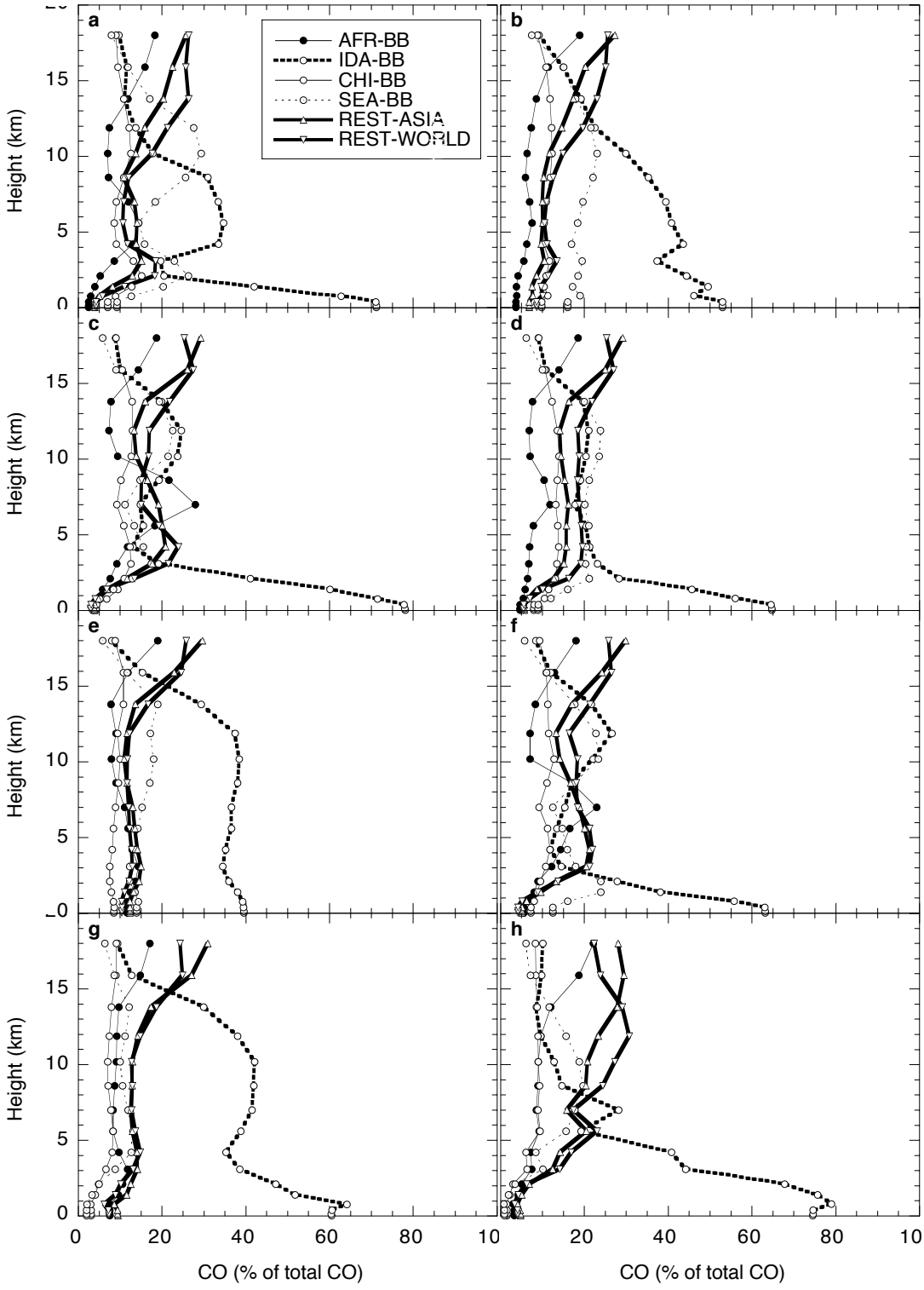

Figure 4.3 Relative contributions (in %) by different source categories and regions to modeled total CO mixing ratios, shown in Figure 4.2. The "Rest Asia" source excludes Indian, Chinese and South East Asian BB-CO sources, the "Rest World" source excludes all Asian sources and African BB-CO sources.

resolution the agreement is much better. Returning to profile 4.2e, the model does not reproduce the southern hemispheric air masses in the boundary layer at both T30 and T63 resolution. This profile was taken close to the ITCZ. The model does not resolve the position of the ITCZ very well, simulating it too far south at this location. At the coarse T30 resolution some southern hemispheric air is artificially mixed over the large grid boxes, so that it appears that the T30 simulation yields better agreement with measurements near the surface.

Figure 4.3 shows the corresponding modeled contribution of different CO source categories and regions for the profiles in Figure 4.2. With the exception of profile 4.2e, the most important CO source in the boundary layer appears to be BB-CO from India.

In the free troposphere, a number of different sources become important. In general, Indian BB-CO is important, but not dominant. In the convective outflow region between 8 and 12 km, enhanced levels of South East Asian BB-CO can also be found (Figure 4.2, profiles a, b, c, d and f).

The other important source regions to the free troposphere (BB-CO from Africa and China, the remaining Asian sources and the remaining global sources) each contribute between 10-30 % to the total CO mixing ratio. Interestingly, several profiles (especially profile f in Figure 4.2) show pronounced CO peaks at about 5 km, which are not captured by the model. However, the source analysis (Figure 4.3) indicates an enhanced contribution of African BB-CO in these profiles. Backward trajectories based on ECHAM4 wind fields (not shown) indicate that this could be associated with convective transport of African BB-CO to the free troposphere and eastward advection along the southern edge of the subtropical jetstream and subsequent descend over northern India.

4.4 Comparison of surface observations with modeled CO.

Next we performed a comparison between observed CO during the Ron Brown ship track [Stehr et al, 2001] and modeled ECHAM4 CO (Figure 4.5). The ship track is shown in Figure 4.4. At DOY 53 the ship entered the Indian Ocean south of the ITCZ, where clean airmasses were present with average CO mixing ratios of 50-60 ppbv. At DOY 58 the ship entered to the northern hemisphere and the CO mixig ratios increased to 180 ppbv. Between DOY 60 and 64 the ship was in Male, the capital of the Maldives. Moddled CO mixing ratios were high during this period. The model captures the transition from southern to northern hemispheric air masses very well, although some "intermediate" air masses at DOY 56 and 57 are present in the model which do not appear in the measurements. As indicated earlier, this is related to the poor model resolution of the ITCZ, often seen in the aircraft and ship CO data as a sharp transition over a few tens of kilometers. The model captures the high CO mixing ratios at DOY 59, although the maximum mixing ratios are underestimated, and at DOY 65, where the maximum modeled CO mixing ratio agrees better with the observations, although the timing of the peak is not fully correct. The fractional contribution of different sources (Figure 4.5b) shows that for the peak around DOY 59 modeled CO originates mostly from India, but there is a significant contribution of the rest of the world,

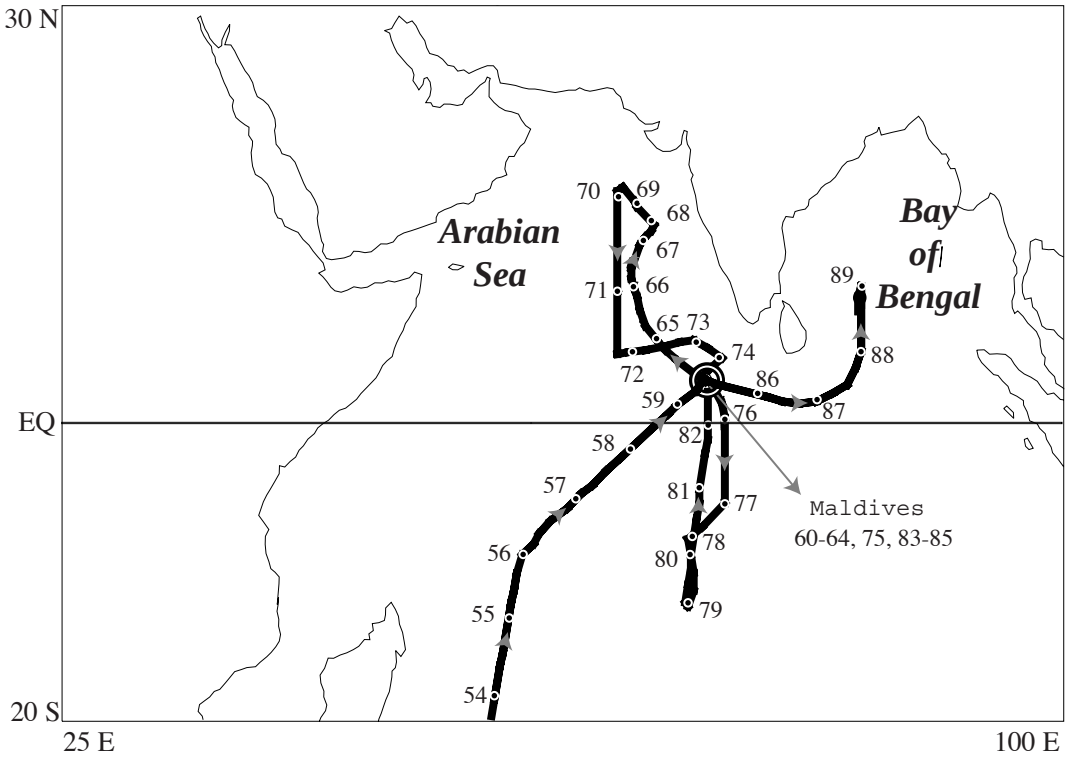

Figure 4.4 The position of the R/V Ron Brown during leg 2 of the Intensive Field Phase of INDOEX. The markers indicate the ship's position at 12 UTC each day between DOY 65 and 83 (DOY=number of days since 1 January, DOY 2 = January 2, 00:00 UTC).

which in this case are mostly air masses originating from South East Asia. At T63 resolution these peaks are captured much better by the model. For the modeled peak at DOY66, India is also the major source region (Figure 4.5b), whereas the South East Asian contribution has diminished considerably.

After an initial high CO mixing ratio on DOY 65, CO quickly decreased to values around 120 ppbv over the entire Arabian Sea. The model reproduces the CO mixing ratios as observed between DOY 66 and JD 72 quite well (Figure 4.5a). The fractional contribution of model sources, shown in Figure 4.5b, suggests that between DOY 67 and 71 Indian BB-CO was only of minor importance. Instead, CO originated from a number of source categories and regions in the northern hemisphere. Also, there is a large residual amount of CO (~ 50 %) which is not accounted for by the direct CO sources, indicating a large fractional contribution by hydrocarbon oxidation.

The modeled CO mixing ratios increased to a maximum at DOY 73 and 74, when the position of the ship was closest to the Indian subcontinent (Figure 4.4). However, such an increase was not observed. Moreover, in the model the mixing ratios started to decrease after DOY 74, whereas in the observations this started later (DOY 76), and measured mixing ratios were lower. The model performance seems worse at T63 resolution, where CO mixing ratios for the peak at DOY 73 are even higher. This is in

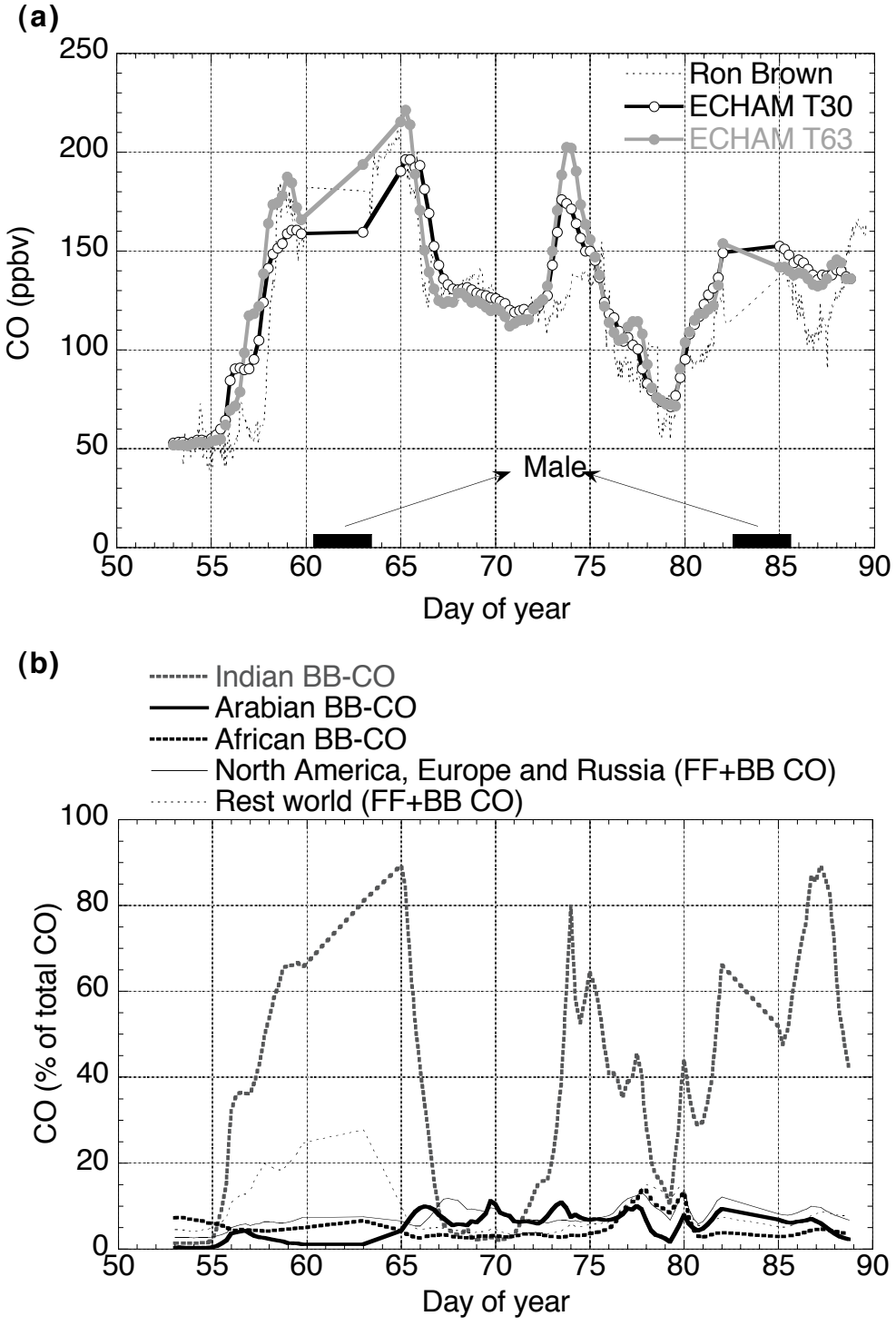

Figure 4.5 Comparison between surface CO mixing ratios (ppbv) measured on the R/V Ron Brown and modeled CO **(a)** along with the corresponding source distribution **(b)**, as % of the total modeled CO. The "Rest World" source excludes the ones explicitly mentioned.

sharp contrast with the comparison of the measured and modeled CO profiles, which clearly shows that the model performance improves at higher resolution (also e.g. for the peaks at DOY 59 and 65 in Figure 4.5a). This indicates that the model does not reproduce the circulation patterns close to the Indian continent very well. We believe that this is associated with sub-grid scale processes, as will be discussed later (section 6). The better agreement of T30 compared to T63 is just fortuitous as the coarser resolution model averages different transport regimes that are not resolved.

Between DOY 76-80 the measured mixing ratios decreased to near background CO mixing ratios, as the ship reached its southernmost position on DOY 79. Modeled CO mixing ratios show a similar tendency, although they are slightly higher than observed. After DOY 80 both modeled and measured CO mixing ratios increased as the ship sailed northward. The model shows an increased contribution by African BB-CO as well as the remaining sources (mostly BB-CO from China and South East Asia) between DOY 78 and 81. This indicates that mixing between northern hemispheric and tropical air masses takes place near the ITCZ.

Between DOY 82 and 85 the ship was at Male again. After DOY 85 the ship sailed to the Bay of Bengal. Initially, CO mixing ratios decreased as the ship moved away from the Indian subcontinent. After DOY 87 the mixing ratios increased as the ship sailed north into the Bay of Bengal, where it encountered more polluted air masses. On average the model reproduces the observed mixing ratios for the period after DOY 85, but the subsequent decrease and increase are not captured. The source analysis (Figure 4.5b) shows a large fraction of Indian BB-CO on DOY 86-87, as the ship observed a CO minimum of about 110 ppbv. Part of this decrease is caused by vertical mixing associated with sub-grid scale convection encountered by the ship during DOY 86 and 87 [R. Dickerson, personal communication]. The convection is not resolved by the model, hence CO mixing ratios do not decrease.

Figure 4.6 shows the comparison between modeled CO and observations at the Kaashidhoo Climate Observatory (KCO) island station in the Maldives [Lobert and Harris, 2000; Lobert *et al.*, 2001]. The model reproduces the mean observed CO mixing ratios, although it misses much of the finer scale details. As shown by the comparison with the observed vertical CO profiles and with the ship measurements, the model sometimes misrepresents the boundary layer structure, especially close to the Indian subcontinent. However, the model accurately simulates the large-scale circulation [De Laat *et al.*, 1999; De Laat and Lelieveld, 2000; De Laat *et al.*, 2001]. Considering that KCO is 500-1000 km downwind of the major CO sources, it seems that the modeled source categories, regions and strengths are quite realistic. In general, biofuel use and other forms of biomass burning constitute the foremost CO source as modeled for KCO with about 50-60 % originating from India. The minimum in the Indian contribution at DOY 54 (Figure 4.6) coincides with easterly winds, associated with cyclonic activity, while the ITCZ had advanced further north, inducing mixing between Indian BB-CO and that from South East Asia with cleaner air masses from the south. Before DOY 68 (7 March) a significant contribution of BB-CO from China and South East Asia is discerned (Figure 4.6). After DOY 68, the influence of China and South East Asian decreased, while the contribution of Arabia increased, mostly due to BB-CO.

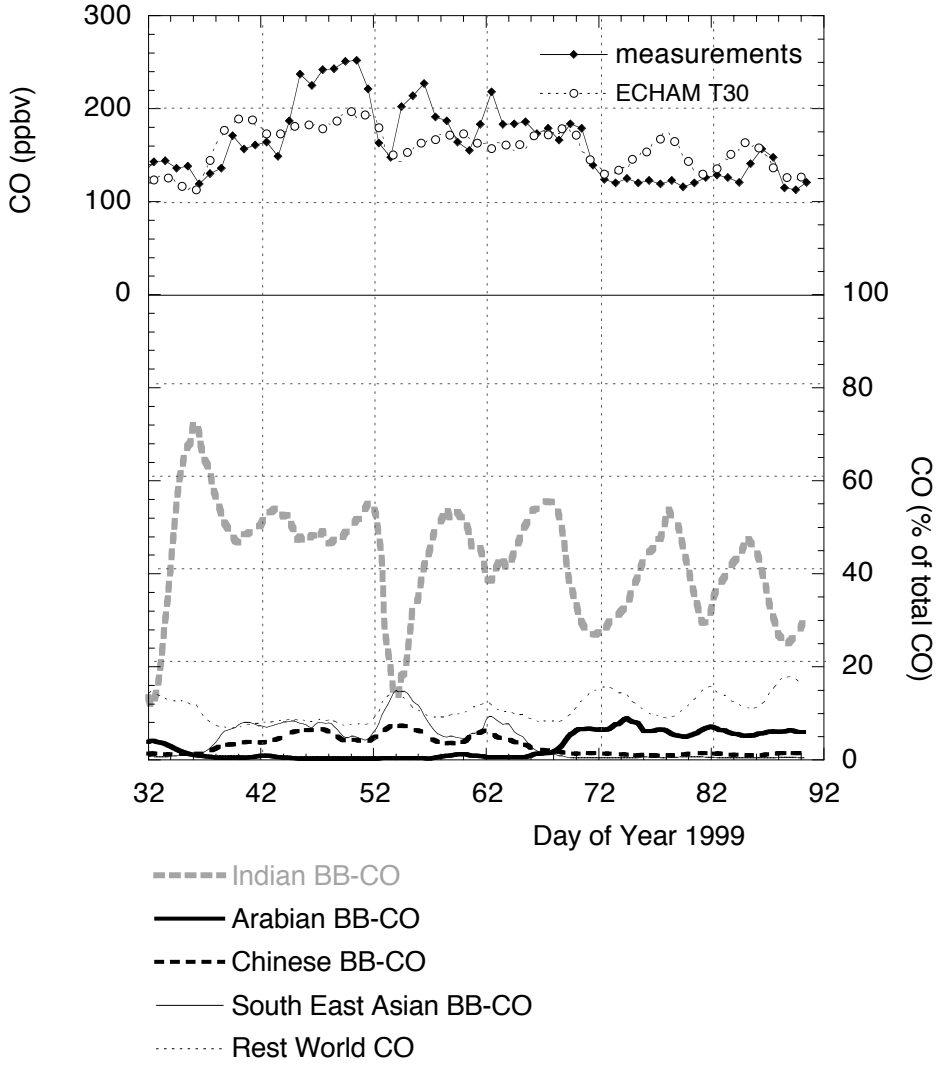

Figure 4.6 As Figure 4.5 for the island station at Kaashidhoo (73.5° E and 5° N).

Because of the definition of the Arabian area, i.e. the Middle East (Figure 4.1), the total amount of BB-CO emissions is about 3 times as large as the total amount of FF-CO emissions (Table 4.1). In fact, most of the BB-CO emissions take place north of the Arabian Peninsula (Turkey, Iraq, and Iran).

4.5 Modeled CO over the Indian Ocean.

Most of the modeled CO in the boundary layer over the Indian Ocean originates from the continental areas at the northern Indian Ocean rim (Figure 4.7). Over the central and western Indian Ocean BB-CO from India and Arabia are the main sources, whereas further east BB-CO from South East Asia and China become more important. These four regions contribute 50-70 % to the total CO at the surface over the Indian Ocean north of the ITCZ. Interestingly, the rest of the Asian continent accounts for only 5 % of the total-CO mixing ratios over most parts of the Indian Ocean, while, in general, little Asian pollution reaches the southern hemisphere. On the other hand, we infer a 10 % contribution by other global sources (notably African BB-CO) to CO over the entire Indian Ocean, including the region south of the ITCZ.

In the upper troposphere at 10-km altitude the most important CO source appears to be hydrocarbon oxidation (Figure 4.8). In the outflow regions of the ITCZ over the western Indian Ocean the most important source of directly emitted CO is Indian BB-CO. Further away from the convection the contribution of Indian BB-CO decreases whereas the contributions of African BB-CO and remaining Asian and global sources increase. All three source regions contribute about equally (10 %). Each individual source contributing to the "WORLD-REST"-source contributes only a limited fraction(< 2 %), with the exception of Indonesian BB-CO, which contributes up to 4 % directly over Indonesia. Therefore, the most important direct source of CO south of the ITCZ over the Indian Ocean is African BB-CO. Figure 4.8 also shows that most of the CO originating from northern hemispheric sources is transported back to the northern hemisphere after it is transported to the free troposphere at the ITCZ. A small fraction of the Indian BB-CO reaches the southern hemisphere. Most cross-equatorial transport takes place close to the tropical African east coast, as the ITCZ over land and near the coast is more latitudinally dispersed than over the ocean.

Another source of CO in the southern hemisphere is South American BB-CO, which accounts for most of the WORLD-REST-CO at high altitudes south of the equator in Figures 4.8 and 4.9, although its contribution is smaller than African BB-CO, in particular over the southern Indian Ocean. CO from India and South East Asia is advected in the marine boundary layer towards the ITCZ, where it is lifted into the free troposphere by convection. At high tropospheric altitudes, CO spreads out with most of it being transported back to the northern hemisphere and only a small part mixed to the southern hemisphere. The remaining global sources contribute significantly only in the continental Asian boundary layer. However, the African BB-CO is directly injected from the boundary layer over Africa into the upper troposphere by deep convection, where it disperses across the globe. Over northern India a maximum in African BB-CO mixing ratios is present in much of the troposphere. This is associated with large-scale subsidence over northern India. This is not the case over the southern Indian Ocean, where the maximum in African BB-CO is less pronounced because it travels at higher altitudes.

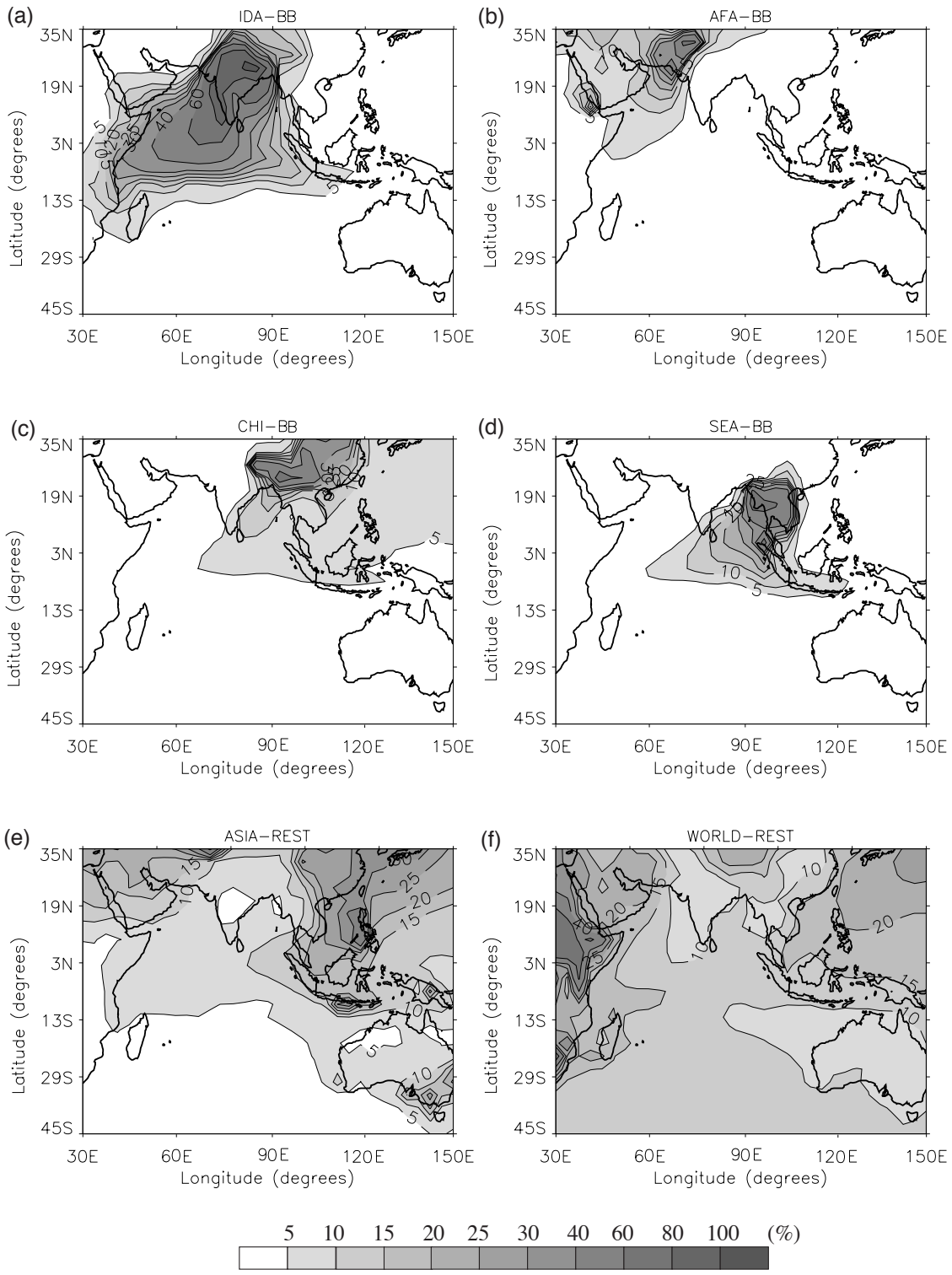

Figure 4.7. Modeled surface CO mixing ratios (ppbv) over the Indian Ocean by different sources, averaged for February and March 1999. (a) Indian, (b) Arabian, (c) Chinese, (d) South East Asian BB-CO, (e) the total of the remaining Asian sources and (f) the total of all other sources. Abbreviations used are defined in Table 4.1.

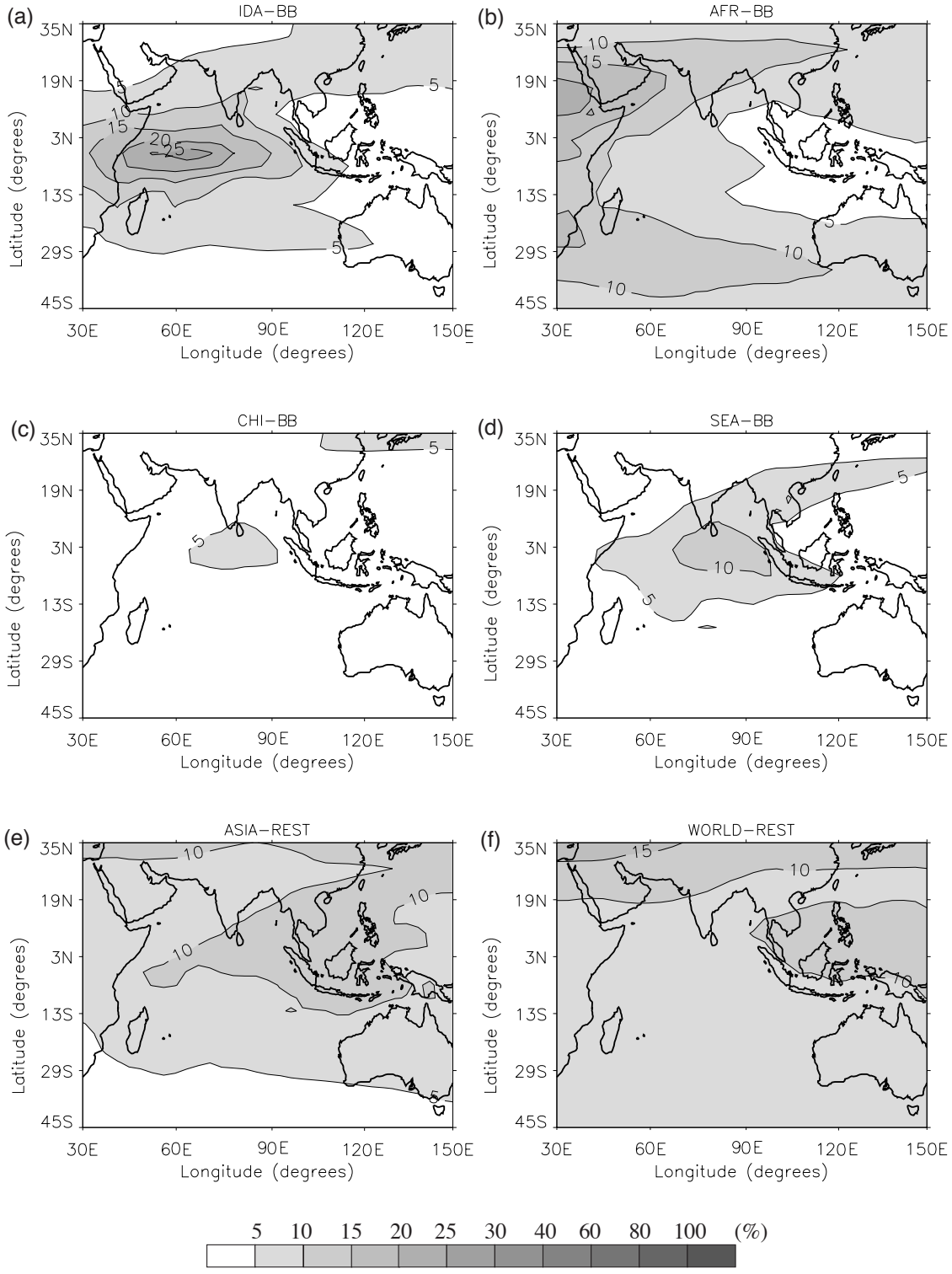

Figure 4.8 As Figure 4.7 at 10 km altitude for (a) Indian, (b) African, (c) Chinese, (d) South East Asian BB-CO, (e) the total of the remaining Asian sources and (f) the total of all other sources.

4.6 Discussion and conclusions

The comparison between measured CO profiles and the model results for the Indian Ocean troposphere indicates that the modeled CO distributions are realistic. Both measured and modeled profiles generally display a typical C-shape. The highest mixing ratios are found in the boundary layer and, to a lesser extent, between 8 and 12 km. The latter are associated with deep convection, which ventilates polluted boundary layer air. The comparison between modeled CO and surface observations indicates that, on average, the model reproduces the observed CO mixing ratios, although it cannot resolve some of the finer structures.

Based on both measured CO profiles and surface mixing ratios, it appears that the model does not correctly capture the boundary layer CO mixing ratios at T30 resolution; discrepancies are of the order of 20 %. For the vertical profiles taken at or prior to 4 March 1999, such discrepancies do not occur at T63 resolution. For the profiles obtained at 15 and 18 March, there is no such improvement between T30 and T63 resolution. This also appears from both the ship and island observations. On average, the modeled CO mixing ratios at KCO (Figure 4.6) before 11 March (DOY 72) were lower than the observed mixing ratios, and higher afterward. A similar problem is manifest from modeled and observed CO along the ship track (Figure 4.5a)

The meteorological overview of INDOEX in 1999 [Verver *et al.*, 2001] describes that the general airflow direction was northeasterly before 11 March. Thus, polluted air masses were advected from the Bay of Bengal region to the Maldives. After 11 March, the flow direction in the boundary layer changed from northeasterly to north-northwesterly. This flow transported air masses from the Arabian Sea to the Maldives, which, in general, were less polluted [De Laat *et al.*, 2001]. In general the underestimation of CO in the model for air masses from the Bay of Bengal region is resolution related, as the discrepancies decrease at T63 resolution. At T30 resolution sharp CO gradients across the Indian Ocean are not very well resolved due to strong artificial horizontal diffusion, which decreases at T63 resolution. It cannot be excluded that the semi-lagrangian advection scheme in the model also contributes to the problem as it is known to be diffusive.

No improvement between T30 and T63 resolution occurs at DOY 73-75 and DOY 86-87 (Figure 4.5). CO mixing ratios over the Arabian Sea (DOY 73-75) even increase for the polluted Indian air masses at T63 resolution, similar to the model results for the Bay of Bengal. The source analysis indicates an enhanced contribution of Indian BB-CO (Figure 4.5b) for both episodes in which CO is overestimated. At the same time, no significant contribution can be found from other regions. On both occasions the measured airmasses originated directly from the southern part of India, which supports the very high contribution from Indian BB-CO. The discrepancy may be related to the sea-breeze circulation at the Indian coast [Raman *et al.*, 2001]. Instead of directly advecting pollutants from the continent to the sea, the sea breeze can lift pollutants to higher altitudes directly above the marine boundary layer. Elevated layers with high levels of pollution between 1 and 3 km altitude have been observed at KCO and during the measurement flights as well [Lelieveld *et al.*, 2001; Lobert *et al.*, 2001]. The sea-breeze circulation also forms an effective barrier for the advection of continental air masses, hence preventing Indian outflow of pollution into the marine boundary layer.

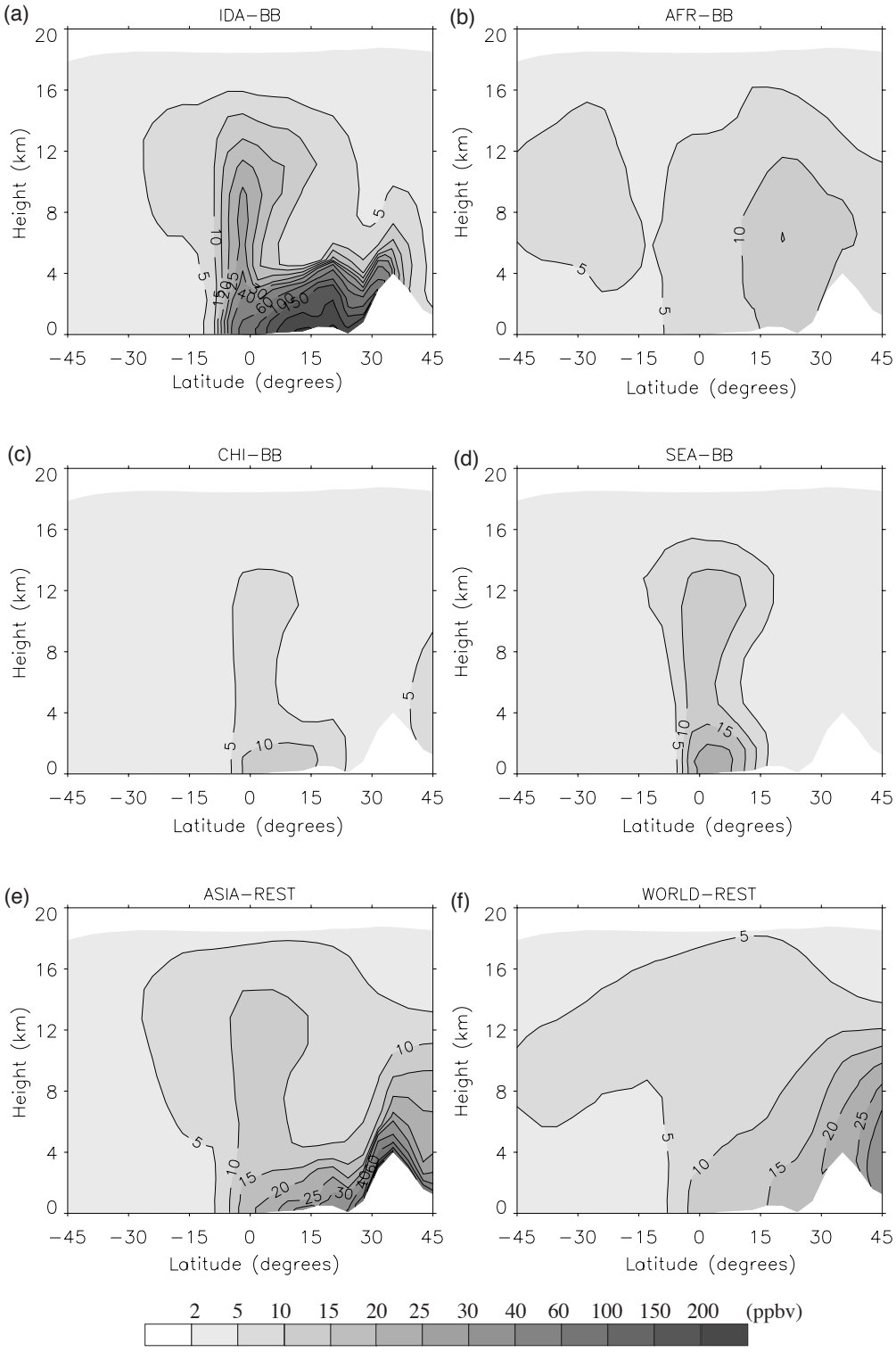

Figure 4.9 Altitude-latitude cross section of CO (in ppbv) for different sources along 77°E, between 45°S and 45°N, averaged for February and March 1999. (a) Indian, (b) African, (c) Chinese, (d) South East Asian BB-CO, (e) the total of the remaining Asian sources and (f) the total of all other sources.

The CO source analysis indicates that, for large parts of the Indian Ocean, Indian BB-CO is the major boundary layer pollution source. Biofuel use and agricultural waste burning contribute most strongly to these CO emissions. Over the eastern parts of the Indian Ocean, especially over the Bay of Bengal, we infer an increased contribution of BB-CO from China and South East Asia. The remaining sources contribute little to the total CO mixing ratios, although occasionally their combined contribution can reach up to 30 % of the total CO mixing ratio. Because the destruction of CO by OH is efficient in the tropical marine boundary layer, the fractional and absolute contribution of direct sources to total CO decreases substantially towards the ITCZ.

At high tropospheric altitudes, several sources contribute significantly to the total CO mixing ratios over the Indian Ocean. No individual source contributes more than about 15 %, with the exception of Indian BB-CO over the western equatorial Indian Ocean (up to 25 %). Over the central and eastern Indian Ocean we calculate an increased contribution of BB-CO from China and South East Asia. African BB-CO, the remaining Asian sources, as well as the remaining global sources each contribute between 5 and 15 %. The contribution by African BB-CO is quite important in the middle troposphere over India due to subsidence of high altitude CO, while the contribution of the remaining Asian sources is higher close to the central and eastern equatorial Indian Ocean. The contributions of the remaining global sources are rather evenly distributed.

The major CO source in the marine boundary layer in the close vicinity of India is Indian BB-CO. However, over large parts of the Indian Ocean other CO source categories and regions contribute as well. This is more evident over the northern parts of the Arabian Sea and the Bay of Bengal, where CO is comprised of Indian, Arabian (mostly from Turkey, Iran and Iraq) and African BB-CO, as well as northern hemispheric FF-CO, remaining global sources and CO from hydrocarbon oxidation, which all contribute about equally.

Figure 4.10 shows a comparison of the relative contribution of different sources to the total average model calculated CO mixing ratios at the surface and at 5-km altitude. The relative contribution is calculated for several important regions where CO levels are generally enhanced (the hydrocarbon oxidation part is calculated as the total CO mixing ratio minus FF-CO and BF-CO). The regions are similar to those in Table 1 and Figure 1, with the exception of "Southeast Asia", which also includes of China, Japan and Indonesia. Near the surface (Figure 4.10a) the CO emission signature of the different regions is dominant. For the Indian region the most important source is CO from biomass burning, in particular biofuel use. For South East Asia and Africa biomass burning is important, but fossil fuel use and hydrocarbon oxidation contribute significantly. Galanter *et al.* [2000], using a global transport chemistry model, report similar high contributions of 60-80 % by biomass burning to surface CO in Africa, India and South East Asia for the period December-February. However, they find higher fractions over Africa than over India, in part related to strong burning activity in the Sahel region in January, taking place before the INDOEX period (Feb-Mar). We suspect, moreover, that our Indian CO source from agricultural burning (58 Tg yr^{-1}) exceeds that assumed by Galanter *et al.* [2000], whereas our CO emission from biofuel use (47 Tg yr^{-1}) seems similar.

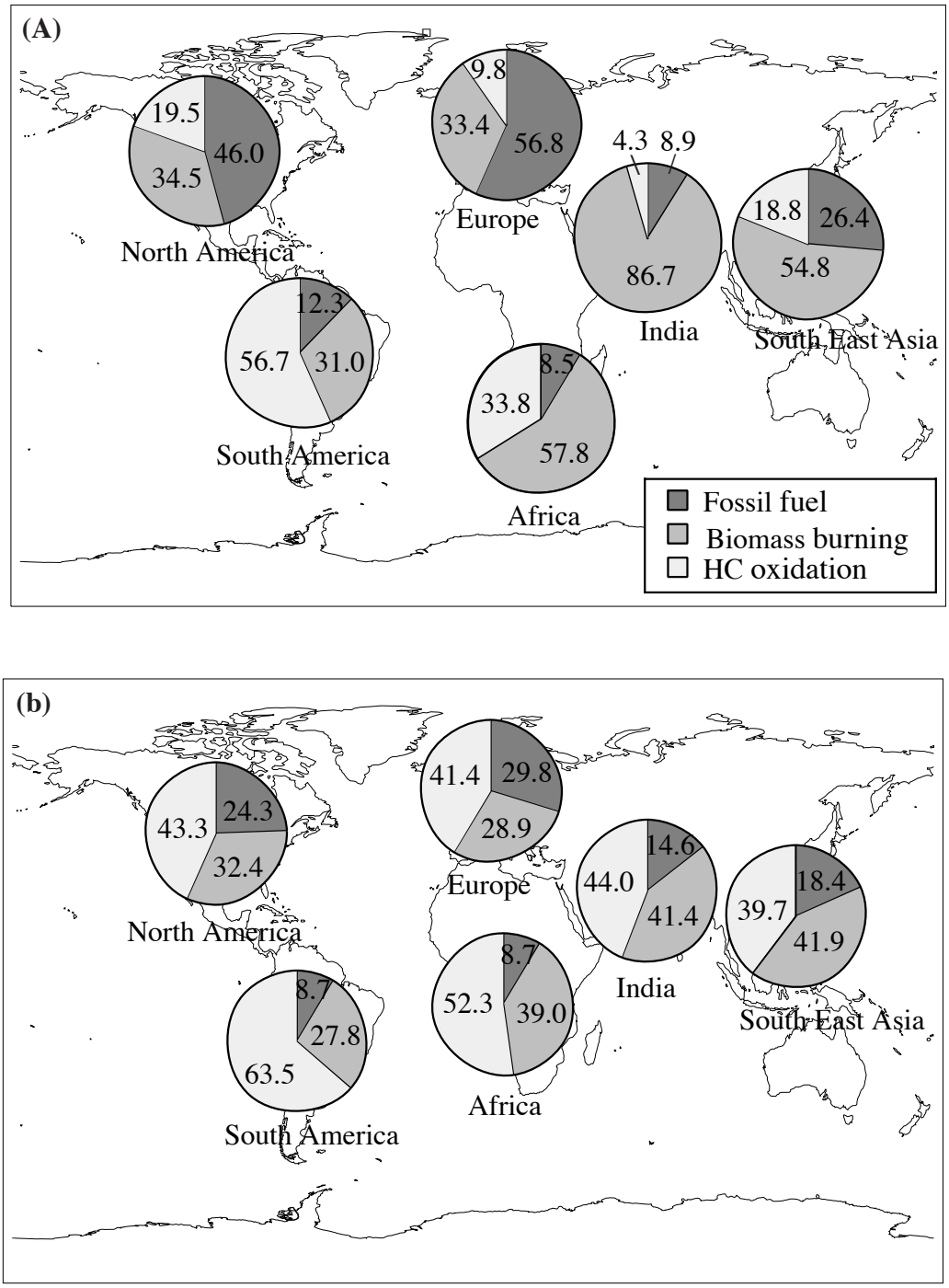

Figure 4.10 Comparison at **(a)** the surface and **(b)** 5 km altitude of the relative contribution (%) of different sources (biomass burning and biofuel use; fossil fuel use; hydrocarbon oxidation) to the modeled total average CO mixing ratios. The comparison is made for several regions around the globe, averaged over February and March 1999. For a definition of these regions, see Figure 4.1.

North America and Europe appear similar with a large contribution from fossil fuel use to surface CO (Figure 4.10a). For South America the most important source is the oxidation of hydrocarbons, which are emitted by the Amazon rainforest. The ratio of modeled BB-CO to FF-CO at the surface for the Indian region (nearly 10:1) is almost similar to the emission ratio of BB-CO and FF-CO as estimated by the EDGAR v2.0 emission inventory in our model [Lelieveld *et al*., 2001]. For other regions the modeled ratios differ more from the EDGAR v2.0 estimates. This indicates that in those regions, besides local emissions, advection from outside the region plays an important role. It also indicates that in India and the INDOEX region during the dry monsoon local emissions dominate the chemical composition of the lower troposphere.

At 5-km altitude (Figure 4.10b) the differences between regions are much smaller. In general, the signature of the CO emissions at the surface is still discernable (higher than average from biomass burning over India, Africa and South East Asia, higher than average fossil fuel use over North America and Europe, and higher than average from hydrocarbon oxidation over South America), however, due to the long lifetime of CO considerable dispersion takes place. The fractional contribution by biomass burning of about 40 % over Africa, India and South East Asia agrees with the estimate by Galanter *et al*. [2000], who report a range of 30-45 %. From Figure 4.10b it is also evident that the most important source of CO in the free troposphere is the oxidation of hydrocarbons that accounts for 40-60 % of the total CO mixing ratios.

Chapter 5

Model analysis of trace gas measurements and pollution impact during INDOEX

Abstract

An analysis of hydrocarbon measurements, performed during the Indian Ocean Experiment (INDOEX), using a chemistry general circulation model, points to (residential) biofuel use and agricultural burning as important pollution sources in the Indian region. A comparison with measurements indicates that the model simulates realistic CO and acetone distributions, except towards the Indian west coast near the surface. The latter may be related to a sea breeze circulation at the Indian west coast, not resolved by the model. A comparison of the measured and modeled correlation between CO and acetone indicates the presence of a background marine acetone source. A model sensitivity study suggests a global marine emission strength of 15-20 Tg acetone $year^{-1}$, a significant contribution to the estimated global acetone emissions of 40-60 Tg acetone $year^{-1}$. Modeled non-methane hydrocarbons (NMHC: ethane, propane, butane, pentane, acetylene, benzene) are comparable to measured NMHC. This gives credence to the EDGAR v2.0 NMHC-emission inventory used in the model and it confirms that biomass is the main source of these trace gases in the INDOEX region. The comparison of measured and modeled CO-acetonitrile correlation indicates that a model sink of acetonitrile in the marine boundary layer may be missing. A model sensitivity study suggests that this could be dry deposition (deposition velocity estimate: 0.01-0.05 cm s^{-1}) on the ocean surface.

Submitted to *Journal of Geophysical Research, 2000*, with co-authors J.A. de Gouw, A. Hansel and J. Lelieveld.

5.1. Introduction

South East Asia is an important source region of atmospheric pollution [Lelieveld *et al.*, 2001]. The nature of pollution sources in this region is different from that in, for example, North America and Europe. Pollution emissions in South and East Asia, notably of carbon monoxide (CO), are to a large extent caused by biofuel use [Streets and Waldhoff, 1999]. Biomass burning takes place at lower temperatures than fossil fuel combustion, which leads to fairly strong CO emissions. Furthermore, biomass burning causes hydrocarbon emissions. Especially over India much of the pollution is related to biofuel use (wood and cow dung) and agricultural waste burning [Sinha *et al.*, 1998; Mahapatra and Mitchel, 1999; Smith *et al.*, 2000].

During INDOEX, acetone (CH_3COCH_3) and acetonitrile (CH_3CN) were measured onboard a Cessna Citation aircraft by proton-transfer-reaction mass spectrometry (PTR-MS) [De Gouw *et al.*, 2001] and on the NOAA Research Vessel Ronald Brown [Dickerson, 2001; Wisthaler *et al.*, 2001]. Acetonitrile is an excellent tracer for biomass burning [Lobert *et al.*, 1991, Holzinger *et al.*, 1999] and can, in combination with other species like acetone and CO, provide strong indications about the sources of air pollution. Acetone has a more diverse origin, being emitted from natural sources as well as from biomass burning related sources [Singh *et al.*, 1994, 1995, and 2000]. It is also photochemically produced in the atmosphere by the oxidation of propane and other non-methane hydrocarbons (NMHC). The photochemical breakdown of acetone in the presence of NO_x can produce PeroxyAcetylNitrate (PAN), a reservoir of NO_x at low temperatures, e.g. in the upper troposphere [Singh *et al.*, 1995]. Furthermore, acetone can provide significant amounts of OH and HO_2 radicals in the free troposphere that may contribute to O_3 production [Singh *et al.*, 1994, 1995].

In addition to the continuous aircraft measurements of hydrocarbons by PTR-MS, canisters with air samples have been taken during the flights. Low-resolution information about several NMHCs, like ethane, propane, butane, pentane, acetylene and benzene, has been obtained from the canister analyses [De Gouw *et al.*, 2001].

We present a comparison of these measured species with the results from a chemistry-general circulation model (GCM), which provides indications about the model performance and the validity of the emission estimates. Moreover, model simulations have been used to evaluate the source categories and regions and the fate of the measured air pollution.

5.2 Model description.

In this study we use the ECHAM4 model with the NMHC chemistry scheme similar to that of chapter 4. A number of species, measured from canisters during INDOEX [de Gouw *et al.* 2001], are not explicitly modeled in the CBM-4 scheme, but are implicitly part of groups of hydrocarbons defined in the CBM-4 scheme. The effects of these species on the chemistry (including OH) are thus implicitly included in the model. To calculate the spatial and temporal behavior of these compounds, they were added off-line

to the model version at T30 resolution. The removal of these species in the model takes place solely by the reaction with OH, whereas OH itself is not affected. Table 5.1 lists the seven species for which this has been done and their rate coefficients for the reaction with OH as well as their main sources over the Indian subcontinent (60°E to 90°E, south of 30°N). Emission estimates for these species have been adopted from the EDGAR v2.0 database [Olivier *et al.*, 1996]. Because such estimates were not available for acetonitrile in the EDGAR database, these emissions were scaled to the CO release from biomass burning and biofuel use [scaling factor 0.0013 ± 0.0007 from Holzinger *et al.*, 1999]. A model spinup period of 4 months was applied, after which the model was nudged for February and March 1999. Since the lifetime of acetonitrile from the breakdown by OH is of the order of 6-12 months, much longer than the model spin-up time, a zonal average initial profile was constructed based on average CO mixing ratios, with a minimum free tropospheric CH_3CN mixing ratio of 150 pptv adopted from Schneider *et al.* [1997].

Species		K_{298}	Global annual emissions (Tg C yr^{-1})	Main sources in India	
Ethane	(C_2H_6)	2.50E-13	6.6	Residential biofuel use	80 %
				Gas/Oil production	10 %
Propane	(C_3H_8)	1.10e-12	6.2	Residential biofuel use	45 %
				Gas/Oil production	45 %
Butane	(C_4H_{10})	2.23E-12	11.7	Residential biofuel use	10 %
				Gas/Oil production	55 %
				Road transport	25 %
Pentane	(C_5H_{12})	3.90E-12	10.3	Residential biofuel use	25 %
				Gas/Oil production	30 %
				Road transport	35 %
Benzene	(C_6H_6)	1.23E-12	3.7	Residential biofuel use	85 %
				Road transport	10 %
Acetylene	(C_2H_2)	9.00E-13	5.4	Residential biofuel use	90 %
				Road transport	5 %
Acetonitrile	(CH_3CN)	2.16E-14 *	0.9 **	Biomass burning	100 %

Table 5.1 Rate coefficients for the OH reactions of the additional hydrocarbon tracers in the ECHAM4 model and their estimated annual emission [Olivier *et al.*, 1996].

* For acetonitrile the following temperature dependent reaction rate coefficient was applied: 8.1E-13 exp[-1080/T]
** The acetonitrile emissions were assumed to be 0.13 % of the CO emissions from biomass burning and biofuel use

5.3 Comparison of modeled CO and Acetone with observations from the Ronald Brown.

Figure 5.2 shows the measured and modeled CO and acetone mixing ratios at both T30 and T63 resolution during leg 2 of the R/V Ronald Brown track. Modeled CO mixing ratios agree well with the observations between Day of Year (DOY) 65 and 72 and between DOY 76 and 80. The model overestimates CO mixing ratios between DOY 72 and 76 and between DOY 80 and 82. A similar overestimation appears for acetone, but for DOY 78 to 80 the modeled acetone mixing ratios are too low, whereas modeled CO is too high.

Figure 5.1 shows 5-day boundary layer backtrajectories based on ECHAM4 modeled wind fields along the ship track of the Ronald Brown. Between DOY 66 and DOY 72 the ship was located in the Arabian Sea, where the model mixing ratios of both CO and acetone were comparable to the observed mixing ratios. The trajectories indicate that during DOY 65 and DOY 66 the air originated from the Indian subcontinent, whereas between DOY 67 and 72 the air masses originated from the northern Arabian Sea. CO and acetone mixing ratios were relatively high before DOY 66, and they rapidly

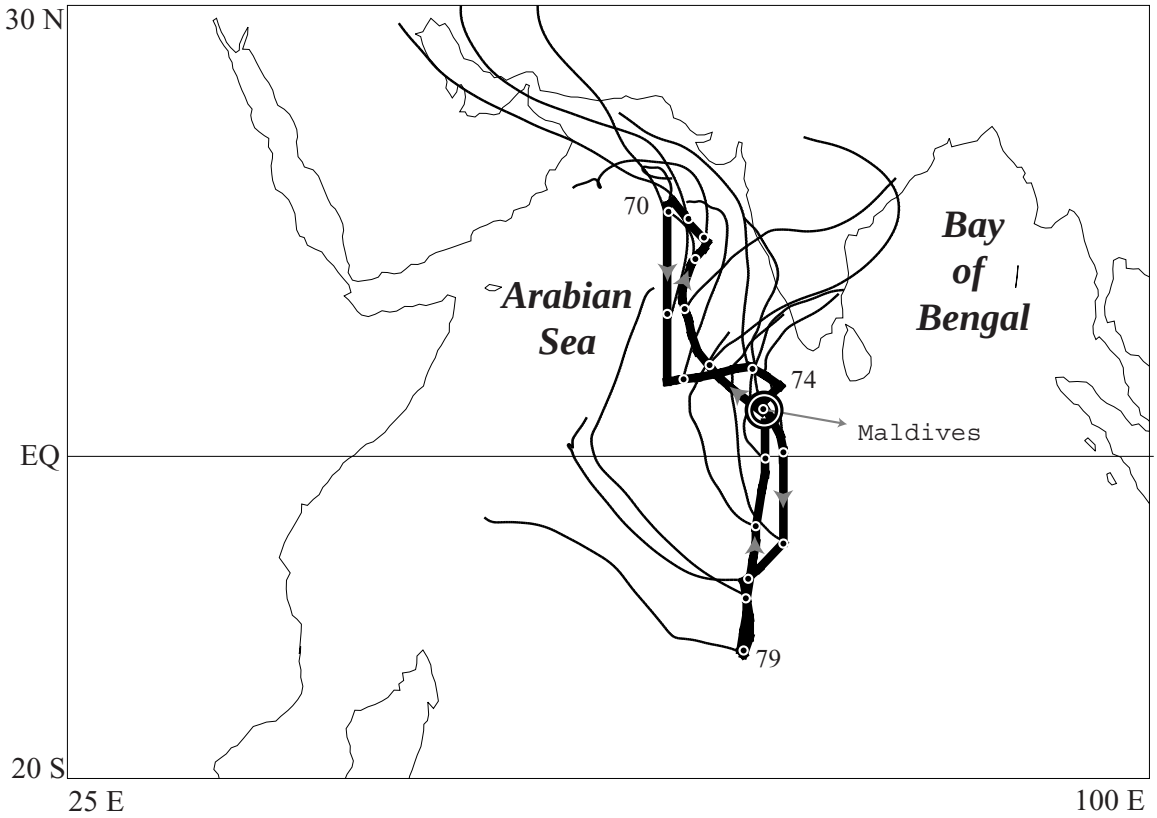

Figure 5.1 The position of R/V Ronald Brown during leg 2 (thick line). The arrows indicate the ship's direction, the numbers indicate the dates (Julian Days) at which the ship was located at that position. The leg started at DOY 66 in Male, Maldives, and ended at DOY 82 at the same location. The thin lines are 5-day backtrajectories based on ECHAM4 simulated wind fields, starting each day at 12 UTC, at 950 hPa, at the ship's position at that time.

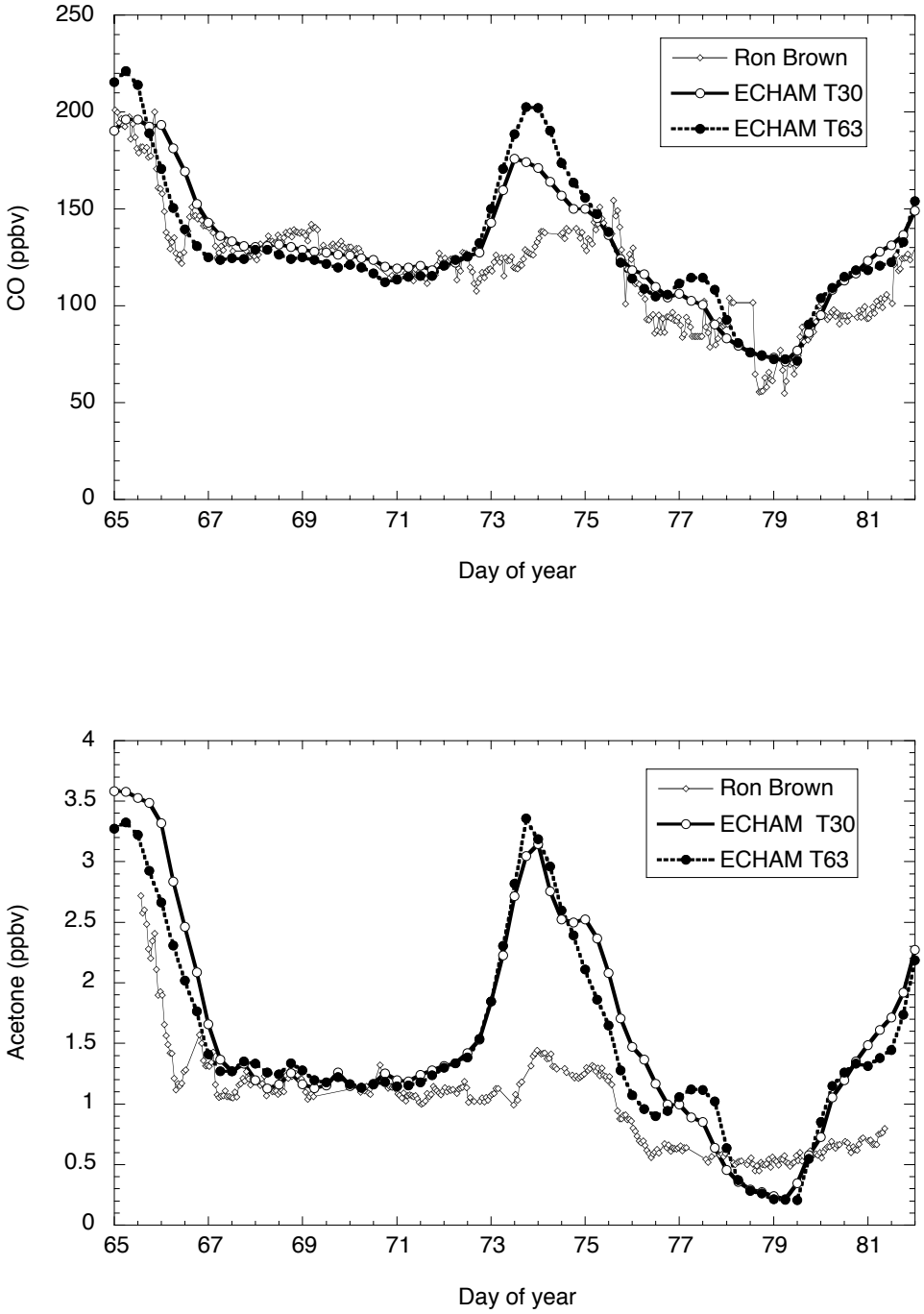

Figure 5.2 Measured and model simulated surface CO and acetone mixing ratios (ppbv) during R/V Ronald Brown leg 2. Model results are shown for two resolutions: T30 (3.75° × 3.75° and T63 (1.9° × 1.9°).

decreased afterwards by the change in air mass origin. Between DOY 72 and 76 the ship went through a more polluted region near the Maldives. For this period modeled mixing ratios of both CO and acetone are high compared to the observed mixing ratios.

The trajectories (Figure 5.1) indicate that the modeled air masses are affected by emissions from the Indian subcontinent. However, 5-day high resolution backtrajectories from the Florida State University model [not shown, Jha and Krishnamurty, 1999] indicate that between DOY 72 and 76 the air masses may not have been affected by the Indian subcontinent but instead have spent an extended period in the marine boundary layer. According to the FSU trajectories pollution from northern India was advected to the northern Arabian Sea. This was not the case in the ECHAM4 model simulation, where the pollution from northern India was advected south along the Indian west coast (Figure 5.3). De Laat *et al*. [2001a] show that overall modeled CO mixing ratios, both in the boundary layer and in the free troposphere, agree with measurements, except for cases during which the modeled air masses were advected along the Indian west coast. This points to a possible role for the local sea breeze circulation at the Indian west coast [Raman *et al*., 2001], which prevents the Indian pollution from being advected into the marine boundary layer over the Indian Ocean. Instead, the pollution is advected to layers just above the marine boundary layer [Lelieveld *et al*., 2001]. In the model the pollution from northern India is directly advected from the continental boundary layer into the marine boundary layer because the model resolution is too coarse to resolve the sea-breeze circulation.

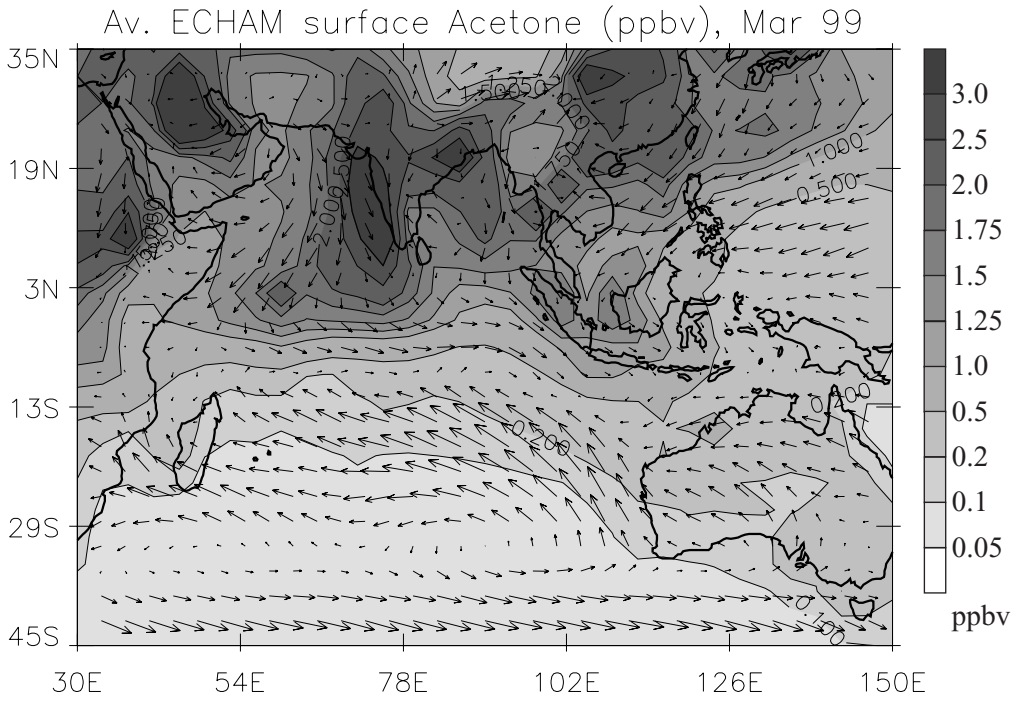

Figure 5.3 Average surface acetone mixing ratios for March 1999 in ppbv from the ECHAM4 model and the corresponding average surface wind field (arbitrary units).

Apparently, the T170 resolution of the FSU model suffices, at least partially, to resolve the sea breeze circulation. At T63 resolution the plume mixing ratios were even higher than at T30 resolution This could be related to artificial horizontal diffusion by the large grid size at T30 resolution, which causes unrealistic plume dilution.

After DOY 74 the ship sailed south and reached its most southern position during leg 2 at 12°S on DOY 79, thereafter returning to the Maldives (Figure 5.2). Observed CO mixing ratios decreased from about 130 ppbv at DOY 76 to about 60 ppbv at DOY 80, indicating that the ship encountered clean air, probably of southern hemispheric origin. The modeled CO and acetone mixing ratios reach minimum values at the most southern part of the shiptrack, but the model does not reproduce the very low CO mixing ratios. This indicates that, in the model, the southern hemispheric influence remains further south.

After DOY 79, observed and modeled CO and acetone mixing ratios increased as the ship headed back to the Maldives. The ECHAM4 backtrajectories from Figure 5.3 reveal that the modeled air masses during the southern part of the leg were advected from the Arabian Sea, carrying only moderate amounts of pollution. During this period a tropical cyclone was present around 12°S, 66°E. The cyclone probably mixed northern and southern hemispheric air masses. The ship's position on 19 March (DOY 78) was northeast of the cyclone, encountering southern hemispheric air masses advected north at the western edge of the cyclone. In the model the cyclone was situated a few degrees further south. Therefore, modeled air masses were very likely not mixed across the ITCZ, resulting in higher CO mixing ratios.

Between DOY 78 and 80 modeled CO mixing ratios are higher than observed, whereas acetone mixing ratios are lower than observed. Since the modeled air masses are of tropical oceanic origin, the model apparently underestimates background acetone mixing ratios over the central Indian Ocean. This will be discussed in more detail in the next section.

5.4 Acetone-CO Correlations

Figure 5.4 shows the measured and modeled acetone-CO correlations. For CO mixing ratios higher than 100 ppbv, the observed and the modeled correlations are similar. This indicates that, although the model overestimates the CO mixing ratios for DOY 72-76 and DOY 80-82 in the Indian plumes due to transport deficiencies, production and destruction of CO and acetone in the model are in overall agreement with the observations, at least in polluted air masses. For CO mixing ratios below 100 ppbv measured acetone mixing ratios were nearly constant, indicating a background acetone mixing ratio of about 0.5 ppbv. Singh *et al.* [1994] have measured similar mixing ratios in the boundary layer at remote locations over the Pacific Ocean. Modeled acetone mixing ratios, however, are not constant for CO mixing ratios below 100 ppbv, but decrease to values close to zero, as the standard model does not account for acetone emissions nor production in clean marine air south of the ITCZ. Figure 5.3 shows that modeled background acetone mixing ratios in the southern hemisphere can even be as low as 0.05 ppbv, a factor of 10 below the observations. It has been suggested that

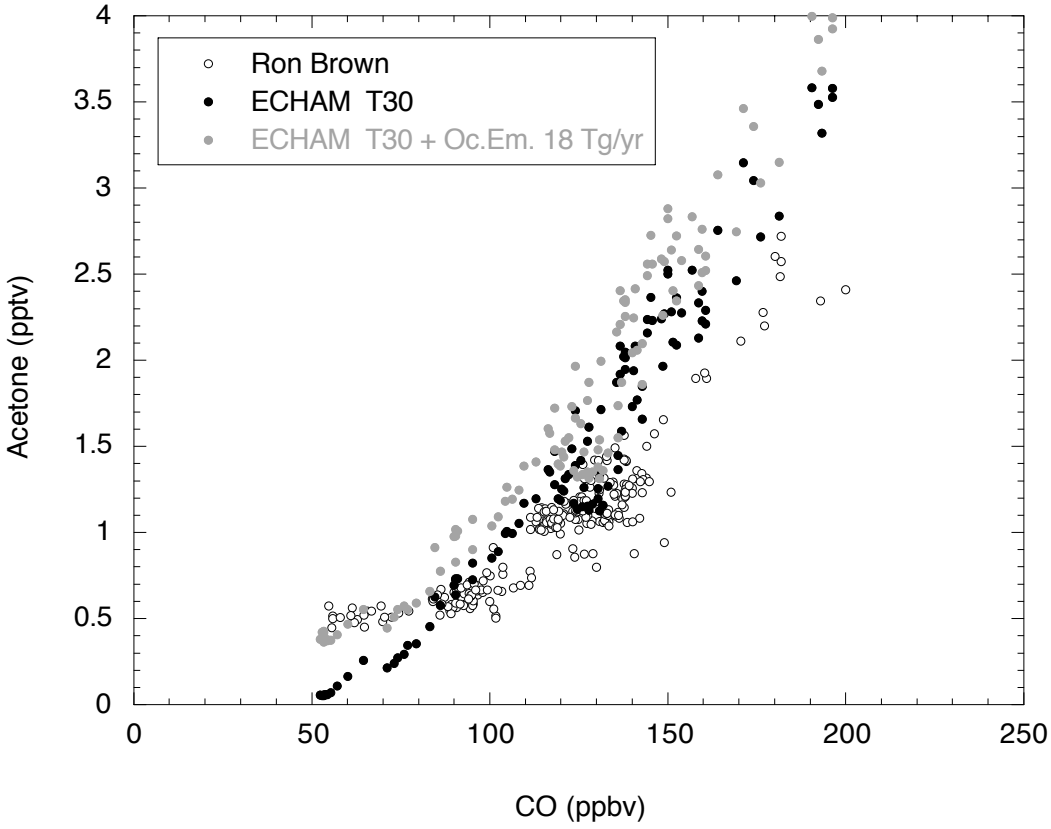

Figure 5.4 Correlation between CO and acetone from the R/V Ronald Brown leg 2 measurements and the corresponding model results from the simulation at T30 resolution. The gray dots show the results from a simulation with presumed marine acetone emissions.

the oceans are a potential photochemical acetone source [Zhou and Mopper, 1997]. Therefore, a model simulation was performed to which a global marine acetone source was added. The emissions were assumed to be dependent on solar radiation leading to a seasonal and latitudinal dependent ocean source amounting to 18.6 Tg acetone $year^{-1}$ (11.6 Tg C $year^{1}$). Thus the strongest emissions result from the tropical and summertime extra-tropical oceans. The effect of this source on modeled acetone mixing ratios and the acetone-CO correlation is shown in Figure 5.4. The acetone mixing ratios increase by about 0.3 ppbv, a small increase relative to the high acetone mixing ratios over the northern Indian Ocean. The slope of the CO-acetone correlation for high CO mixing ratios (> 100 ppbv) remains very similar, as expected. The modeled background mixing ratios of acetone have increased to about 0.4 ppbv, and the discrepancy with the measurements has reduced substantially. If the acetone source assumed here is

representative of the world oceans, these emissions may even exceed other large sources such as biomass burning, thus maintaining the global background of this compound.

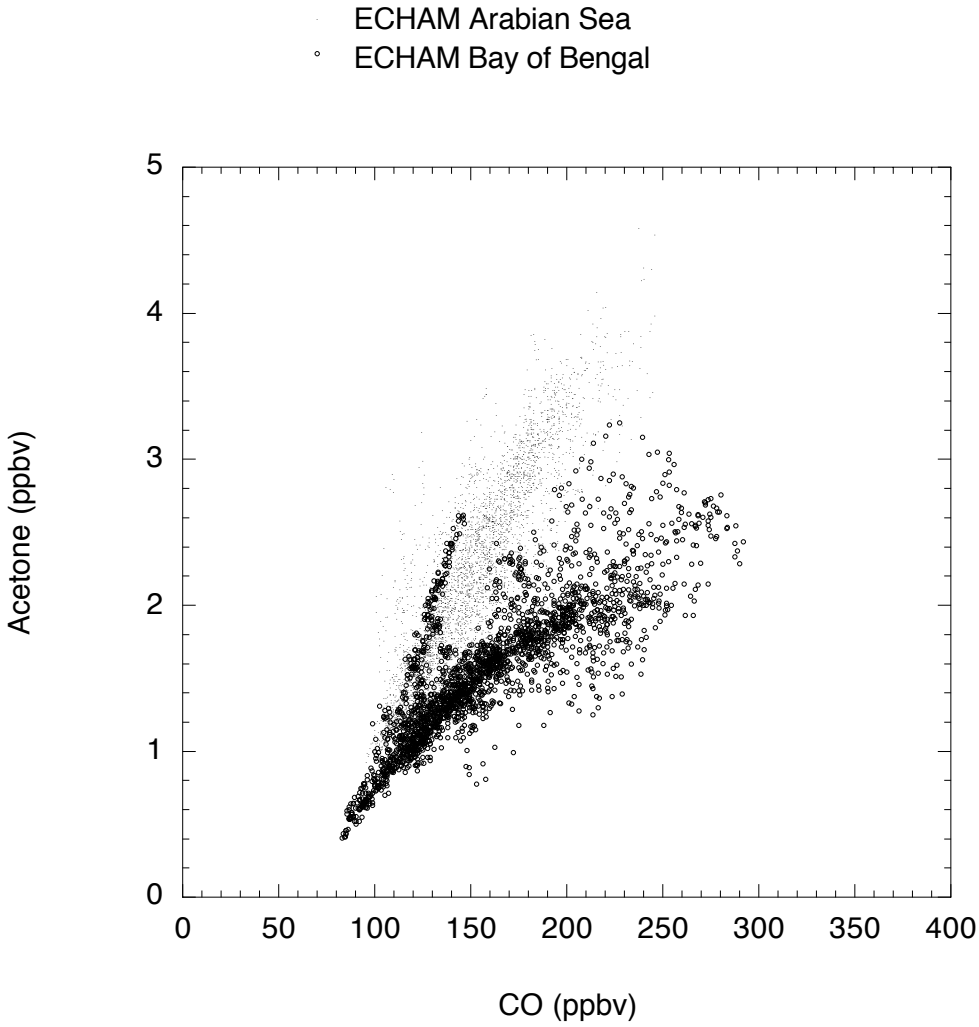

Figure 5.5 Model simulated CO-acetone correlation at T30 resolution (without oceanic source) for the average surface mixing ratios of both February and March 1999. Only gridpoints north of the equator are selected that are at least one grid point away from land grids. The Arabian Sea is defined as west of 77°E, the Bay of Bengal is defined as east of 77°E.

Figure 5.5 shows correlations between modeled surface CO and acetone during February and March 1999 for the Indian Ocean north of the equator between 60° E and 90° E. Only oceanic grid points that are situated at least one gridpoint away from the continents have been selected. Furthermore, we distinguish between the months February and March and between the Bay of Bengal (longitude > 77° E) and the Arabian Sea (longitude < 77° E). These regions are characterized by different CO-acetone

relationships. The mean CO-acetone slope is steeper for the Arabian Sea than for the Bay of Bengal. Figure 5.3 shows that, on average, the highest modeled acetone mixing ratios over the northern Indian Ocean are found over the eastern Arabian Sea close to the Indian west coast, whereas over the Bay of Bengal acetone mixing ratios are lower. For CO, on the other hand, we calculated the highest values in the Bay of Bengal region (Figure 5.6). Although high CO mixing ratios occur along the Indian west coast, even higher mixing ratios occur over southern China and the northeastern part of the Bay of Bengal. The differences in the CO-acetone slopes for both areas are related to the differences in emission sources. At low CO and acetone mixing ratios both Arabian Sea and the Bay of Bengal air masses show the same CO-acetone slope, indicating that mixing between different air masses causes dilution. For higher CO mixing ratios the CO-acetone slope

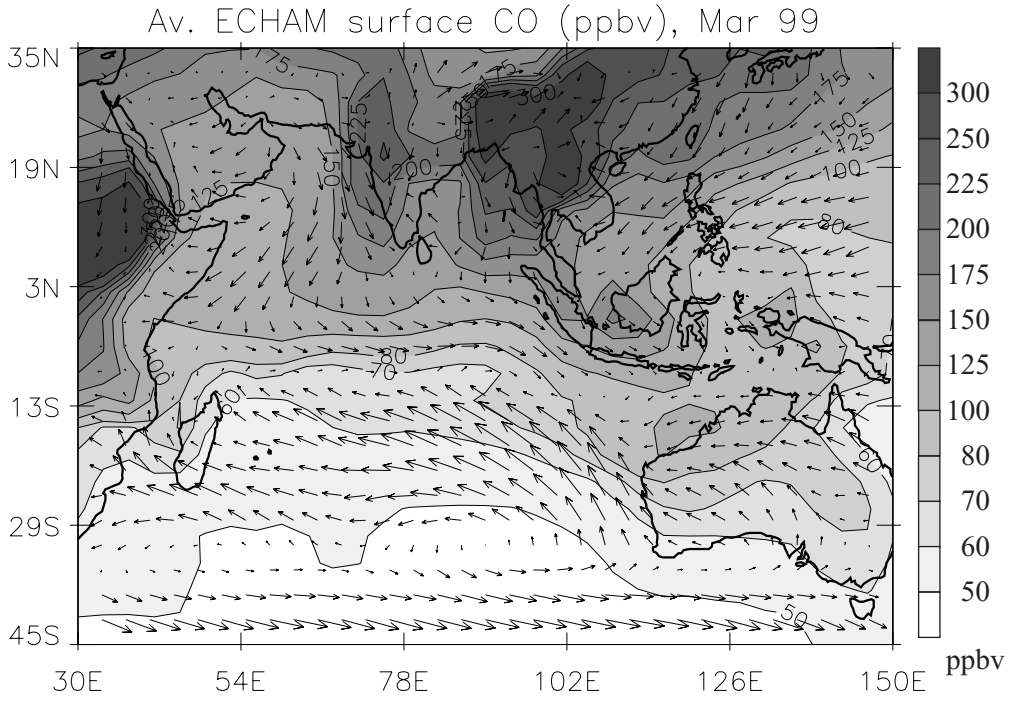

Figure 5.6 Average model calculated surface CO mixing ratios for March 1999 in ppbv, and the corresponding average surface wind field (arbitrary units).

for the Bay of Bengal area deviates from the one for the Arabian Sea. The velocity field (Figure 5.6) indicates that in the northern part of the Bay of Bengal mixing takes place between Indian and Chinese air masses. The Indian air masses are high in acetone because almost all Indian emissions originate from biomass burning (model CO emissions for the Indian region are 73 Tg C yr^{-1} from biomass burning and 3.4 Tg C yr^{-1} from fossil fuel use; for the South East Asian region these values are 59 Tg C yr^{-1} and 32 Tg C yr^{-1}, respectively). Acetone emissions from fossil fuel combustion are only small, so that the CO-acetone ratio is smaller in South East Asia than in India.

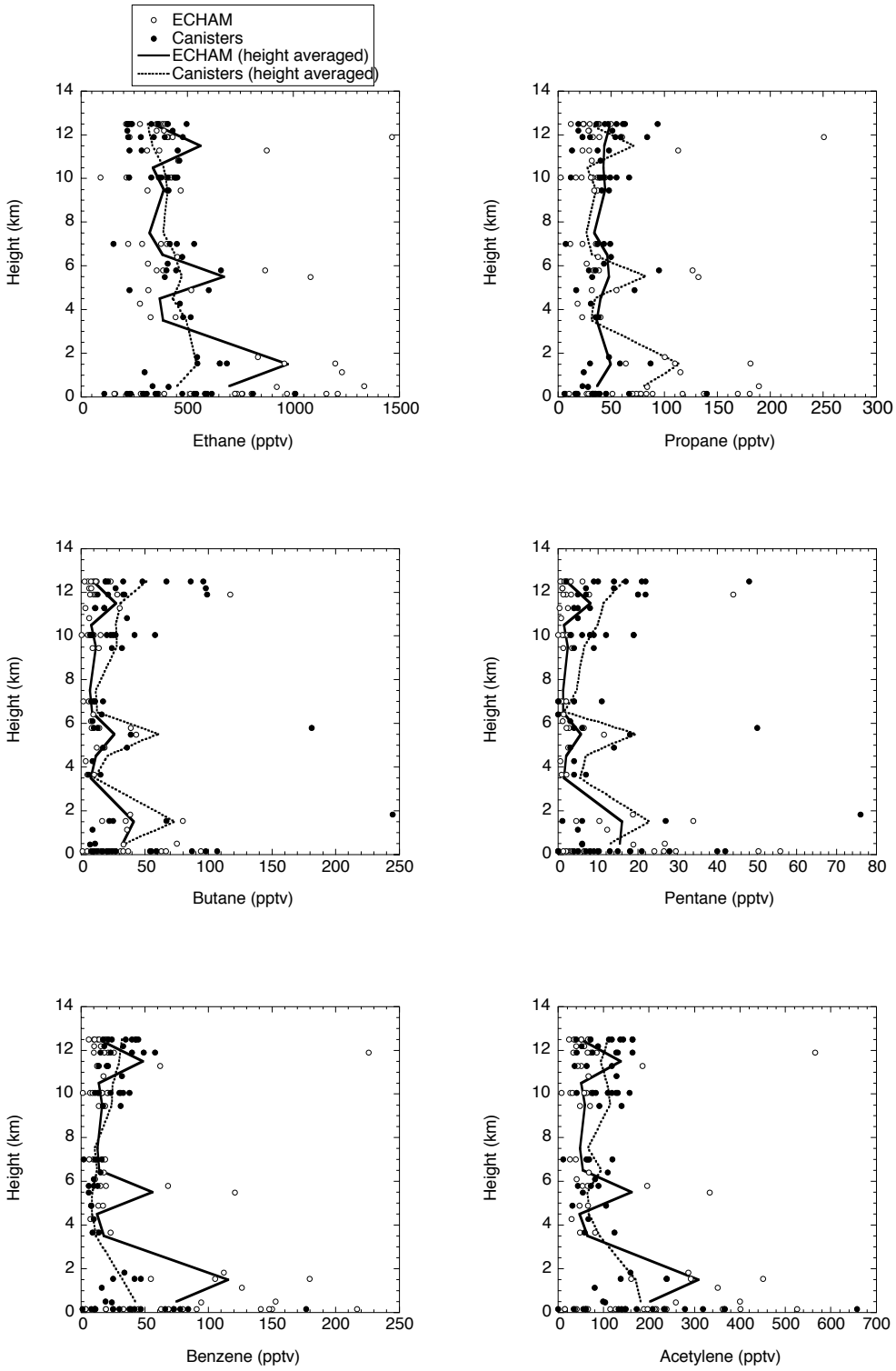

Figure 5.7 Altitude profiles of measured hydrocarbons (ethane, propane, butane, pentane, benzene and acetylene) from canisters taken during INDOEX and the corresponding ECHAM4 model results. Solid lines are the average modeled profiles and dashed lines are average measured profiles, both calculated for 1-km altitude bins.

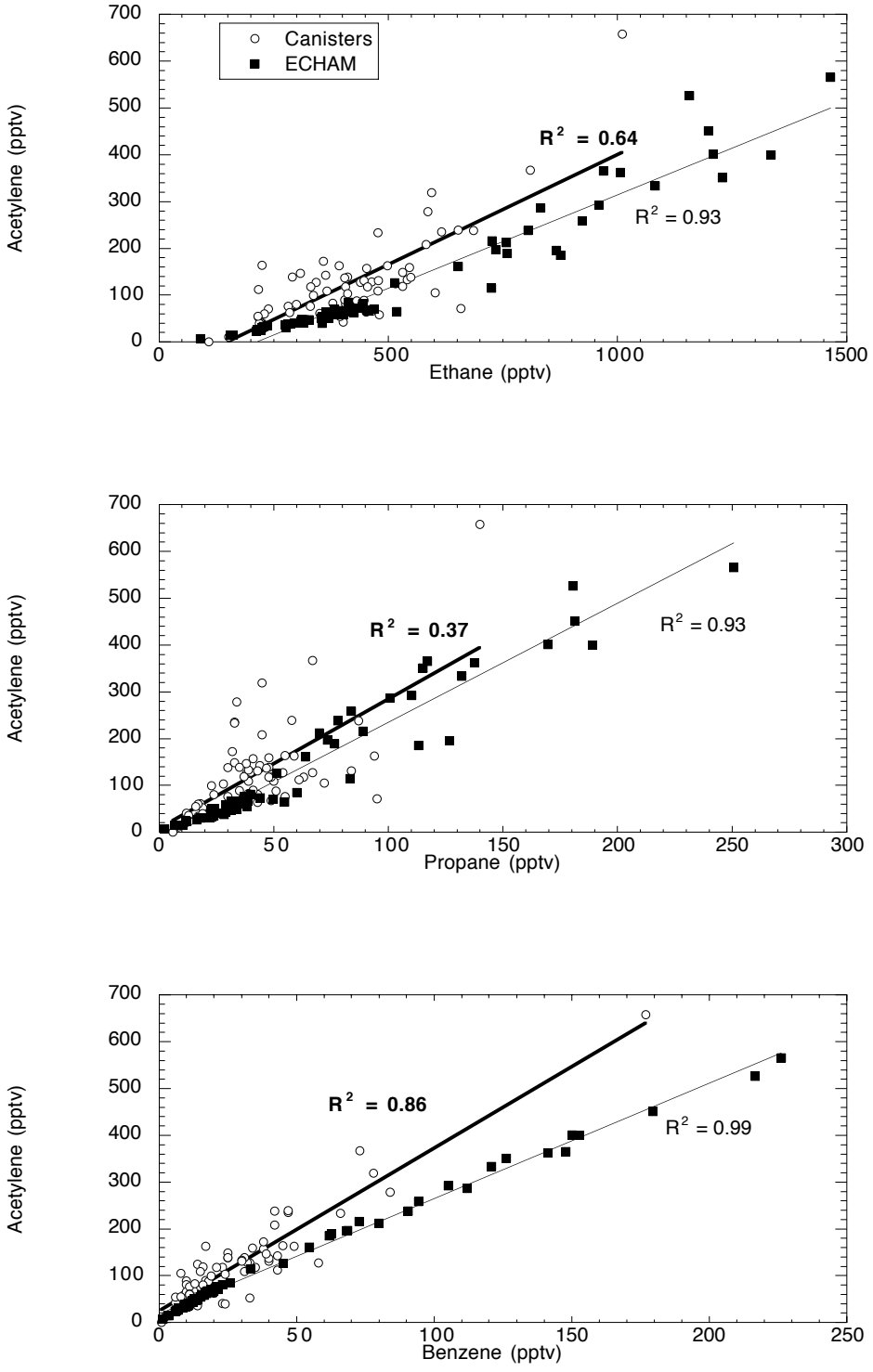

Figure 5.8 Correlation between acetylene and ethane, propane and benzene for the canister data and corresponding model results. The bold numbers indicate the correlations for the measurements, the thin numbers for the model results.

5.5 NMHC model-data comparison

Figure 5.7 shows the comparison between several of the measured species from canister data and the model results as a function of altitude. The model results correspond to the time and location where the canister samples were taken. In general the measured and modeled mixing ratios are comparable. Except for butane and pentane, the model overestimated boundary layer mixing ratios, which appears consistent with the findings from the comparison between the ship measurements and the model as well as the results for CO profiles from de Laat *et al.* [2001a]. On the other hand, the model fairly well reproduces free tropospheric mixing ratios. The mixing ratios of butane and pentane in the free troposphere are underestimated. Because of the short lifetime of these species (~ 2-3 days), the relatively high levels of these gases in the upper troposphere suggest rapid transport of boundary layer air by convection which may have been displaced or underestimated in the model.

Figure 5.8 shows the correlation for both canister data and model results between acetylene and ethane, propane and benzene. For these species the correlations from the model are in fair agreement with those obtained from the canisters. This indicates that the emissions derived from the EDGAR v2.0 database used in this study are probably realistic, and that for the Indian region biofuel use and agricultural burning is an important pollution source, as indicated by the EDGAR v2.0 emission inventory. Furthermore, the minimum ethane mixing ratio of about 0.1 ppbv in the model is similar to that indicated by the measurements. This suggests that the model produces a realistic C_2H_6 background.

5.6 Acetonitrile model-data comparison.

Figure 5.9 shows the correlation of acetonitrile and CO from the ship measurements and the corresponding model mixing ratios. In the model, acetonitrile is emitted by biomass burning and it is photochemically removed by its reaction with OH.
The measurements can be subdivided according to two regions [Wisthaler *et al.*, 2001], represented by two branches. The first branch, for which the trajectories trace back to India, shows a positive correlation between CO and acetonitrile. The major sources and sinks of CO and acetonitrile over India are similar, resulting in a positive correlation. The second branch, for which the data trajectories trace back to the Middle East (Arabian region), shows a negative correlation. This branch appears in the lower panel of Figure 5.9 at about 125 ppbv CO. These air masses originate from sources further north and northwest. A model analysis indicates that the contribution of biomass burning emissions was small in these air masses [de Laat *et al.*, 2001a]. CO remains fairly constant in these measurements, whereas acetonitrile decreases to background levels below 150 pptv. This decrease of acetonitrile also indicates that the contribution by biomass burning emissions is relatively smaller [Wisthaler *et al.*, 2001].

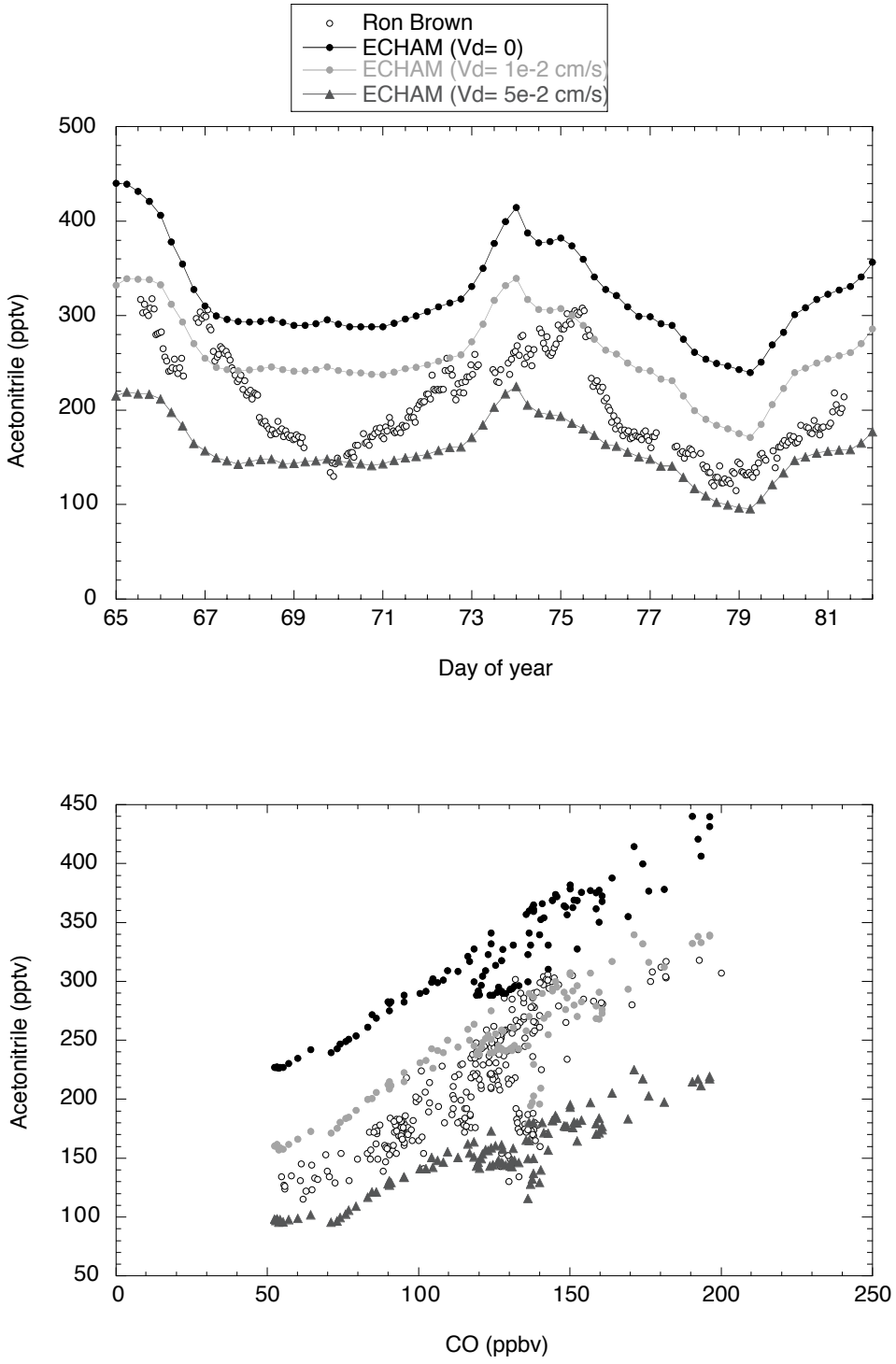

Figure 5.9 Measured and modeled acetonitrile mixing ratios (pptv) as a function of time from leg 2 of the R/V Ronald Brown track (upper pannel) and the correlation between measured and modeled CO (ppbv) and acetonitrile (lower panel),. The markers in both graphs refer to the same data. The model results are shown for simulations: without dry deposition of acetonitrile, and with a deposition velocity of 0.05 and 0.01 cm s^{-1}.

The modeled CO-acetonitrile correlation is positive, but the model overestimates acetonitrile mixing ratios, while the slope of the modeled correlation is smaller than in the observations. The increasing differences between modeled and observed acetonitrile mixing ratios with decreasing CO mixing ratios suggest a sink during advection of acetonitrile in the marine boundary layer, not accounted for in the model. Acetonitrile is moderately soluble in water (Henry's law coefficient: 53 mol $kg^{-1}bar^{-1}$, Benkelberg *et al.* [1995]). Nevertheless, dry deposition of acetonitrile on the sea surface may have a considerable effect on the acetonitrile mixing ratios because of the very slow chemical breakdown of acetonitrile by OH (chemical lifetime in the boundary layer by the OH reaction is 6-12 months). Several model simulations were performed in which different deposition velocities were applied for acetonitrile. Figure 5.9 shows the results from acetonitrile simulations with deposition velocities of 0.01 and 0.05 cm s^{-1}. The CO-acetonitrile correlation is clearly more realistic with a surface deposition sink than in the results from the run without surface deposition. The model results indicate that the

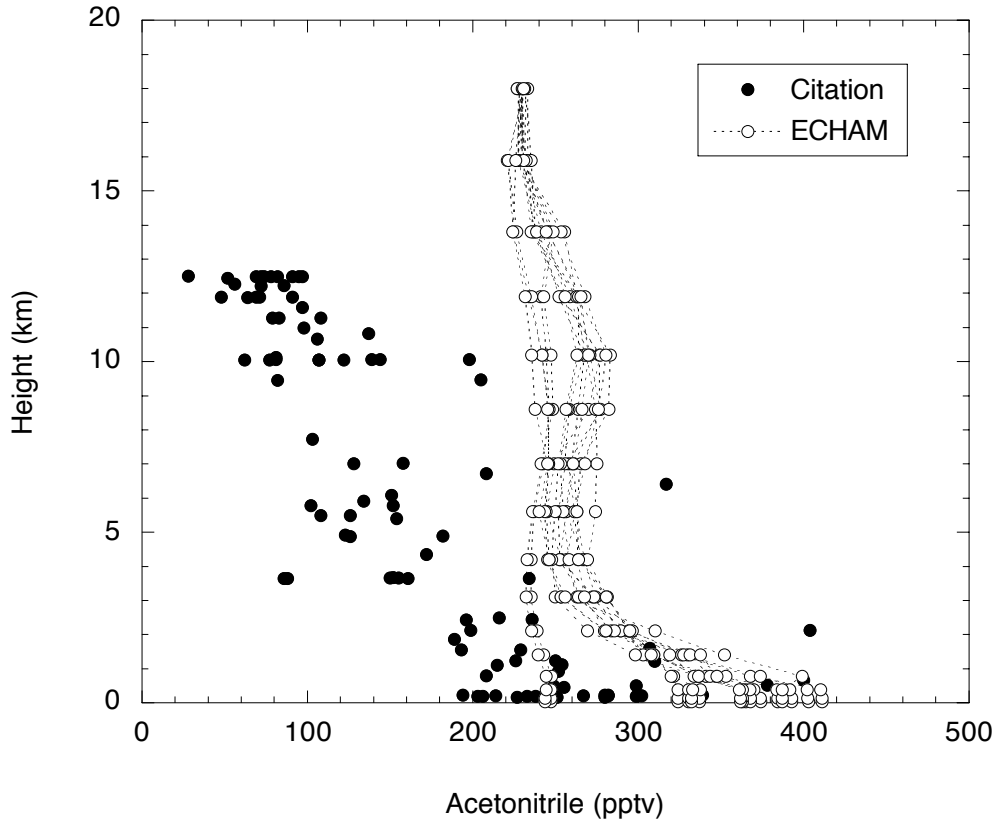

Figure 5.10 Measured and modeled acetonitrile mixing ratios (pptv) as a function of altitude. The measurements include average acetonitrile data from the Citation aircraft constant-altitude flight legs. The modeled profiles (open circles and dashed lines) are obtained for the flight legs during which acetonitrile measurements were performed.

deposition velocity lies between 0.01 and 0.05 cm^{-1}. Using Henry's law constant it is also possible to calculate a deposition velocity for acetonitrile over the oceans based on the parameterization by Wesely [1989]. The calculated deposition velocity is 0.05 cm s^{-1}, somewhat higher than indicated by the model, but an order of magnitude lower than the dry deposition velocity of 0.5 cm^{-1} proposed by Hamm *et al.* [1984].

Figure 5.10 shows the averaged measured acetonitrile mixing ratios obtained from the Citation aircraft constant altitude legs, and the corresponding profiles from the model simulation of acetonitrile with a deposition velocity of 0.01 cm s^{-1}. The observed and modeled mixing ratios in the boundary layer are similar. The two model profiles that deviate from the other modeled profiles were taken around 5°S, where relatively clean air masses were present. De Laat *et al.* [2001a] show that this model overestimation of pollution for clean air masses might be related to an underestimate of cyclonic mixing in the clean air south of the ITCZ.

The observed acetonitrile mixing ratios decrease with altitude, but the modeled mixing ratios are almost constant in the free troposphere, a consequence of the long lifetime of acetonitrile in the free troposphere. The free tropospheric sink of acetonitrile is only small, and acetonitrile is also photodissociated in the stratosphere. This stratospheric sink was not included in the model. Therefore, the upper tropospheric decrease may reflect the influence by stratosphere-troposphere exchange (STE), as suggested by Tuck *et al.* [1997]. Hence STE may transport acetonitrile-depleted air towards the tropical upper troposphere. In addition, wet deposition of acetonitrile through rainout may also remove some acetonitrile from the free troposphere, although this is probably a minor sink [Hamm *et al.*, 1984; Arijs and Brasseur, 1986].

5.7 Conclusions

The comparison between measured and modeled CO and acetone surface mixing ratios reveals that the ECHAM4 model is capable of reproducing the measurements at both T30 and T63 resolutions for the Arabian Sea air masses. The model overestimates both CO and acetone for polluted conditions near the Maldives. This is probably related to the inability of the model to resolve the sea breeze circulation at the Indian west coast. The sea breeze partially prevents advection of polluted continental air masses into the marine boundary layer. Instead, air masses may be transported into the free troposphere, directly above the marine boundary layer. Because of the stability of these layers over the northern Indian Ocean, due to large-scale subsidence, they can be maintained in the monsoonal flow for hundreds of kilometers. As a result of the increasing convective activity towards the ITCZ, these layers will eventually break up by trade-wind convection. Such layers have been observed frequently during aircraft flights, as well as in O_3 soundings from ships and the Maldivian island site Kaashidhoo [Zachariasse *et al.*, 2000, Lelieveld *et al.*, 2001; Mandal *et al.*, 2001; Smit *et al.*, 2001]. In the model, the polluted continental air masses are directly transported to the marine boundary layer in the absence of the sea breeze circulation, and subsequently transported south near the surface. Although there are some discrepancies between modeled and measured CO and acetone, the CO-acetone correlation reveals that for higher CO and acetone mixing ratios

model results and observations are quite similar. This suggests that for polluted environments discrepancies are likely related to mixing and transport processes, rather than emissions and chemistry.

At measured CO mixing ratios below 100 ppbv acetone mixing ratios become almost constant at about 0.5 ppbv. This was not reproduced by the standard model version. Instead, acetone mixing ratios continued to decrease with decreasing CO mixing ratios. Modeled background acetone mixing ratios over the Indian Ocean could be as low as 0.05 ppbv. The oxidation of hydrocarbons from the oceans, as an in situ acetone source (annually 0.5 Tg C yr^{-1}, Singh *et al.*, [1994]), is not included in the model. However, this contributes only about 0.05 ppbv acetone [Singh *et al.*, 1994]. A possible explanation of the discrepancy could be that acetone is directly produced at the ocean surface by photochemical processing of the hydrocarbons in the uppermost layer of the water [Zhou and Mopper, 1997]. A model simulation with a marine photochemical acetone source indicates that about 15-20 Tg acetone yr^{-1} needs to be emitted from the oceans to reproduce the measurements. Such a source equals 25-50 % of the global acetone source of 40-60 Tg yr^{-1} as estimated by Singh *et al.* [1994, 1995]. Although this is only a rough estimate and much remains unknown about this source, our model study nevertheless indicates that an oceanic acetone source can contribute significantly to the global acetone budget.

The comparison between measured and modeled ethane, propane, butane, pentane, acetylene and benzene indicates that the model is capable of reproducing the observed mixing ratios, especially of the relatively longer-lived species. This provides some support to the EDGAR v2.0 NMHC emission inventory as adapted from Olivier *et al.* [1996]. Boundary layer mixing ratios are overestimated, in accord with the model-measurement comparison for acetone and CO as discussed above. The modeled correlations between acetylene and ethane, propane and benzene are also comparable to the observed correlations. This indicates that, according to the EDGAR v2.0 emission inventory, biofuel use and agricultural burning are important sources of NMHC for the Indian region.

The CO-acetonitrile correlation showed that for high acetonitrile mixing ratios model and measurements are comparable. However, for low acetonitrile mixing ratios the modeled mixing ratios were too high. This suggests a missing sink, possibly dry deposition over the oceans. A simulation was performed with different deposition velocities, revealing that a deposition velocity of at least of 0.01 cm s^{-1} and at most 0.05 cm s^{-1} is needed to obtain a realistic CO-acetonitrile correlation. A deposition velocity of 0.01 - 0.05 cm s^{-1} corresponds with a boundary layer lifetime of 1 - 4 months, assuming a boundary layer height of 1 km. This is substantially shorter than the 6-12 month lifetime of acetonitrile with respect to the reaction with OH. This suggests that the most important sink for acetonitrile is dry deposition, not the photochemical breakdown by OH. Li *et al.*, [2000] have suggested a similar oceanic sink for hydrogen cyanide (HCN). Both HCN and acetonitrile have long lifetimes (for HCN a few years, based on the reaction with OH), they are emitted mainly by biomass burning, and are only moderately soluble in sea water (Henry's law coefficient: 12 mol $kg^{-1}bar^{-1}$ for HCN; 53 mol $kg^{-1}bar^{-1}$for acetonitrile).

The measurements also reveal that the acetonitrile mixing ratios decrease with altitude, whereas modeled acetonitrile mixing ratios in the free troposphere are nearly constant.

Acetonitrile is photochemically destroyed in the stratosphere, leading to typical stratospheric mixing ratios of 1-10 pptv [Brasseur et al, 1983; Arijs and Brasseur, 1986]. This process was not included in the model. This deficiency can be reconciled with the suggestion of Tuck *et al*. [1997] that there is a "standing crop" of stratospheric air in the tropical upper troposphere. It seems that the role of STE deserves further attention, since it probably also affects the ozone budget in this altitude region [Zachariasse *et al*., 2000].

Chapter 6

Interannual variability of the Indian winter monsoon circulation and consequences for pollution levels over the northern Indian Ocean

Abstract

Near surface pollution levels over the northern Indian Ocean during the winter monsoon period are subject to large variations between different months and different years. We study this variability using global chemistry-climate model simulations of the Indian winter monsoon during February and March of 1996 to 1999. Previously it was shown that the model reproduces the observed differences in near surface Carbon Monoxide (CO) pollution amounts. Our results suggest that three processes largely determine the CO variability during the winter monsoon: the monsoonal cycle, El Niño and the Madden-Julian oscillation. During the winter monsoon northeasterlies advect polluted air masses in the boundary layer from the continents to the InterTropical Convergence Zone (ITCZ). Variations in the strengths of the Asian continental high pressure and the ITCZ strongly influence pollution levels over the continent and the northern Indian Ocean. Strong continental outflow and a strong ITCZ moderate pollution concentrations through efficient transport. Strong continental outflow combined with a weak ITCZ, on the other hand, prevents efficient removal of pollution from the marine boundary layer, hence CO accumulates. During an El Niño the Asian continental high pressure reduces, which weakens advection of polluted air masses, reduces CO buildup in the boundary layer near the sources over land and decreases CO mixing ratios over the northern Indian Ocean. Variations in the ITCZ convection strenght are associated with active (strong) and passive (weak) phases of the Madden-Julian oscillation (MJO). During active phases the ventilation of pollution from the marine boundary layer reduces CO concentrations.

Submitted to *Journal of Geophysical Research, 2000*, with J. Lelieveld as co-author.

6.1 Introduction

One of the intriguing aspects of the INDian Ocean EXperiment (INDOEX) was the observation that air masses over the northern Indian Ocean contained much more pollutants like CO and aerosols during the Intensive Field Phase (IFP, February-March 1999) than during the First Field Phase (FFP, February-March 1998) [Coakley *et al.*, 2001]. The reason for this difference has been subject of debate since the IFP.

To explain the differences between different months and years it is important to understand the dynamics of the general circulation over the Indian Ocean. Many processes on different spatial and temporal scales play a role in this circulation. The shortest time scale on which the controlling processes take place, apart from diurnal variations, is 3-7 days. In a pre-INDOEX study from Krishnamurty *et al.* [1997] it was found that the variability on this time scale is related to the different "inflow channels" of the InterTropical Convergence Zone (ITCZ). These channels advect air masses from subtropical latitudes towards the ITCZ during the winter monsoon. They are typically located in the western Arabian Sea, the western Bay of Bengal and the southeastern Indian Ocean. The strength of these channels shows a 3 to 7-day variability, related to baroclinic disturbances propagating eastward at subtropical latitudes. Variability on a 3-7 day time scale can be discerned in, for example, the modeled CO mixing ratios in

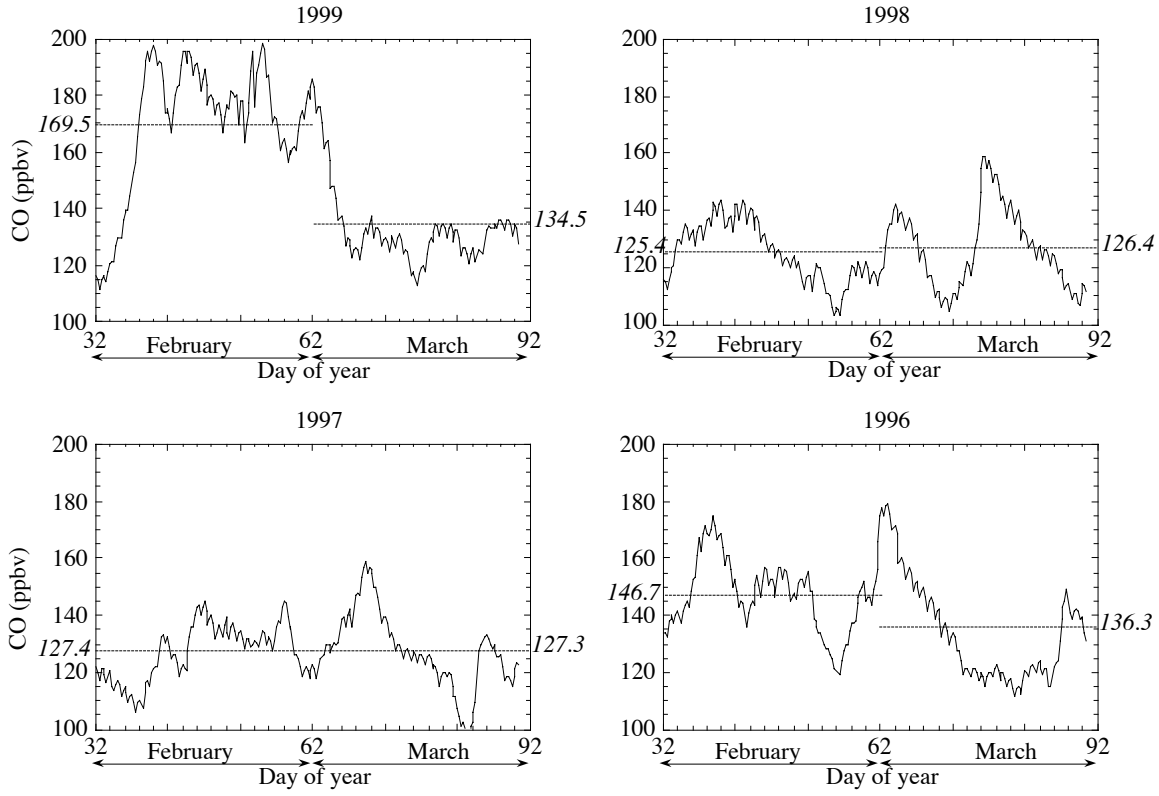

Figure 6.1 Surface CO mixing ratio (ppbv) at 5.6°N, 76.9° E, for February and March 1999, 1998, 1997 and 1996, calculated with the ECHAM4 chemistry-general circulation model. The solid lines correspond with the monthly averaged modeled CO mixing ratios.

Figure 6.1. However, the amplitude of CO variations on this time scale are relatively small compared to the differences between February 1999 and 1998.

Another type of variability in the tropical circulation patterns, taking place on a 30-60 day time scale, is the so-called "Madden-Julian" oscillation (MJO). This variability is especially manifest at higher altitudes in, for example, the wind fields or the outgoing long wave radiation [e.g. Knutson and Weickmann, 1987]. The MJO is related to upper-tropospheric eastward propagating waves, causing increases and decreases in the strength of convection. It is believed that the MJO is the result of complex interactions between tropical waves and convection, although the exact mechanism is still debated [e.g. Waliser *et al*., 1999].

Furthermore, the monsoon has its own interannual variability, the Tropical Biennial Oscillation (TBO). Observations show that a strong monsoon is often followed in the next year by a weaker monsoon [Meehl, 1997]. This feature appears to be more important for the Indian summer monsoon than for the winter monsoon.

According to Webster *et al*. [1999] another oscillation exists in the Indian Ocean basin because of a coupled ocean-atmosphere interaction, which behaves similar to the El Niño/Southern Oscillation (ENSO) over the Pacific Ocean. The time scale of this phenomenon is not exactly known.

The last (known) mechanism, which could explain part of the observed variability, is ENSO, which also affects the monsoon circulation over the Indian Ocean. The atmospheric circulation during an El Niño year is characterized by changes in the precipitation patterns. El Niño is associated with complex interactions between the equatorial ocean and atmosphere circulations, and it is know that El Niño affects the summer monsoon [Webster *et al*., 1998]. It is therefore plausible that El Niño also affects the winter monsoon circulation.

Our approach to explain the observed variability of the Indian winter monsoon circulation has been to establish whether or not the our chemistry-general circulation model the observations, in particular the more polluted 1999 compared to 1998, and subsequently use the model as a tool for analysis. We have shown in previous work that the model represents CO levels over the northern Indian Ocean quite accurately [De Laat et al, 1999, 2001]. From Figure 6.1, which shows the modeled CO mixing ratios at 5.6°N, 76.9°E, during the February and March period for 1996 to 1999, the CO variability is quite evident, indicating that February 1999 was more polluted than the other periods shown.

It is important to note that in these simulations the model emissions are the same for all years. Furthermore, the total CO emissions used in the model for the Indian subcontinent add up to 20 Tg C for February and 19 Tg C for March [EDGAR v2.0 database, Olivier *et al*., 1996; Hao and Liu, 1994]. The difference in CO emissions (5 %) between February and March cannot explain the differences between February 1999 and the other months (of the order of 20-40 %).

The 1999-1998 differences may partially be related to El Niño, because from summer 1997 to early 1998 a particularly strong El Niño occurred. However, El Niño does not explain why 1999 was also much more polluted than early 1997 and 1996, previous to this El Niño year. Therefore, other mechanisms must be involved as well.

In this study we investigate how the variability of CO over the Indian Ocean is linked to the different processes that play a role in the general circulation in this region.

In section 6.2 we explain the spatial and temporal scales of the processes that determine the variability of the winter monsoon circulation. In section 6.3 we present model results for the February months of 1996 to 1999. In section 6.4 we discuss these results and explain the year to year variations using the processes, and we briefly discuss model results for the March months of 1996 to 1999. We end with a summary and conclusions in section 6.5.

6.2 Variability of the winter monsoon circulation

The large scale circulation over the Indian and Pacific Oceans during the winter monsoon can be characterized by three main branches [Figure 6.2, adapted from Webster *et al.*, 1998]. These branches have a common origin, the convective regions over northern Australia and Indonesia. The Walker circulation couples the monsoon with the Pacific Ocean atmosphere. The transverse monsoon links the monsoon convection with high pressure areas over the southern Indian Ocean, and the lateral monsoon links the monsoon convection with the high pressure area over central Asia.

At the surface a flow from the subtropical high-pressure areas towards the ITCZ is present over the Indian Ocean. This circulation is the result of a pressure gradient between the high pressure areas over the Asian continent and the southern Indian Ocean, and the ITCZ where the surface pressure is low. The surface flow advects polluted northern hemispheric air masses from the north and clean southern hemispheric air masses from the south toward the ITCZ.

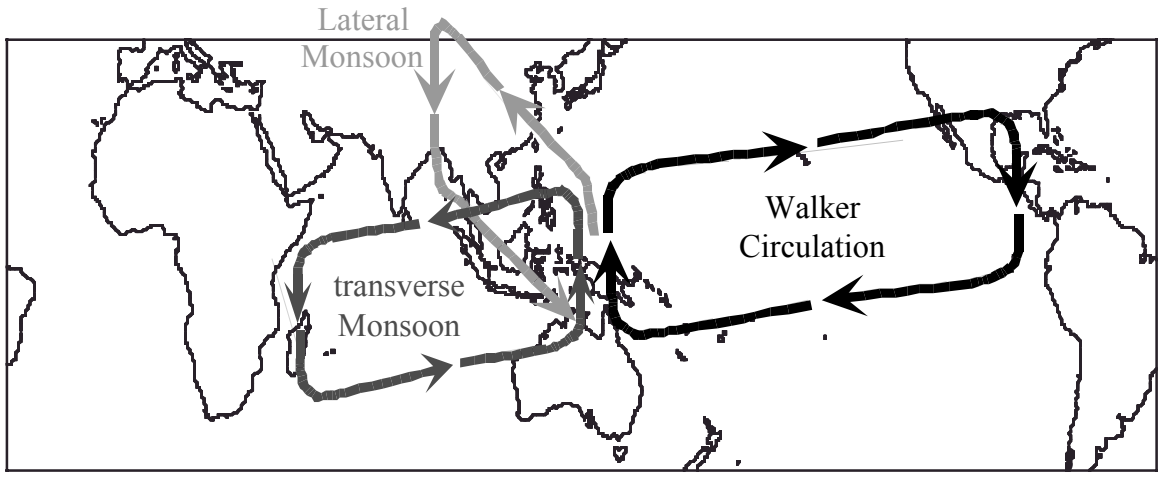

Figure 6.2 Schematic overview of the important components of the general circulation during the winter monsoon [Webster *et al.*, 1998].

The presence of the Asian continent north of Indian Ocean causes high surface temperatures during summer, which causes the ITCZ to advance relatively far north. Air masses are advected from the warm and moist Indian Ocean towards India, bringing extensive rainfall. At the end of the summer (early September) the ITCZ starts to

withdraw from India. This southward withdrawal is a gradual process during which the ITCZ follows the maximum in solar radiation. By December the monsoonal rains have disappeared from India, although convection occasionally occurs over southern India during the entire winter monsoon period. In the mean time, the Asian continent cools during autumn because of lower solar radiation and snowfall, and high pressure gradually builds up. This results in a surface pressure gradient between the continent and the ITCZ. The circulation reverses and dry and cold air masses start to be advected from the continent to the ITCZ over the Indian Ocean, the continental outflow. By December the ITCZ is located south of the Equator, and it remains there until spring (March) when the maximum in solar radiation moves back to the northern hemisphere. At the same time the high-pressure area over the Asian continent weakens due to higher surface temperatures, and the continental outflow weakens. The ITCZ continues to follow the maximum in solar radiation north until it has returned to India by June. This cycle occurs every year with a remarkable regularity. For large parts of southeast Asia and India the monsoon rains return every year in almost the same week.

6.2.1 El Niño

The most important process causing variations in the monsoon circulation is El Niño. This phenomenon changes the tropical circulation over the entire globe. During an El Niño year sea surface temperature anomalies cause an eastward shift of the deep convection over the tropical Pacific Ocean. This shift of convection changes the tropical Walker circulation. It also affects the convection over South America and Africa, which shifts eastwards from the equatorial landmasses towards the equatorial Oceans. In the Indian Ocean region El Niño causes a decrease of the convective activity over Indonesia and northern Australia, and an increase east of Madagascar. As a result, the circulation over the Indian Ocean changes considerably. The lateral monsoon weakens (Figure 6.2), thereby weakening the high-pressure area over the Asian continent. The convective area east of Madagascar causes strong upper tropospheric outflow and subsidence, which suppresses the occurrence of convection over the central and eastern equatorial Indian Ocean. The higher equatorial surface pressure over the Indian Ocean and the lower continental surface pressure decrease the pressure gradient over the Indian Ocean and thus the continental outflow. In the mean time, the strong convection east of Madagascar causes enhanced southward advection of northern hemispheric air masses along eastern Africa.

6.2.2 Madden-Julian Oscillation.

Another process that plays an important role in the variability of the (winter) monsoon circulation is the Madden-Julian oscillation (MJO). This feature, accompanied by variations in convective activity, is still not fully understood. The oscillation is associated with eastward propagating waves in the upper troposphere, and consists of periods of weak and strong convective activity along the ITCZ on a time scale of 30-60 days. The MJO is best distinguished in upper tropospheric meteorological variables like the outgoing longwave radiation or the velocity potential [e.g. Knutson and Weickman, 1987; Matthews *et al.*, 1999].

Although the MJO is a reoccurring feature, the oscillation itself is rather irregular. Periods with decreased MJO-activity are often seen in both observations and model simulations [Waliser *et al.*, 1999; Matthews *et al.*, 1999], and the period of the MJO also varies considerably between 30 and 60 days. The MJO exhibits its greatest variability over the Indian and western Pacific Oceans. Over the Eastern Indian Ocean the MJO activity weakens, also because the Andes mountains in South America deflect the MJO wave north and south along the mountain range, thereby decreasing the MJO activity [Waliser *et al.*, 1999; Matthews *et al.*, 1999]. During strong El Niño years the MJO appears to weaken [Slingo *et al.*, 1996].

Active and passive phases of the MJO are associated with strong and weak convection in the ITCZ. Strong ITCZ convection is associated with strong advection of air masses from the surrounding oceans to the convective areas, and similarly, weak convection is associated with weak advection. The strong advection and convection will lead to an efficient transport of pollutants in the boundary layer from the source regions and subsequently rapid vertical transport and upper tropospheric detrainment as well as removal of soluble species. If the convection is weak, the advection is less efficient and the amount of pollution removed from the boundary layer is smaller.

6.3 ECHAM4 model results for February.

Figure 6.3 shows the average modeled surface CO mixing ratios and Figure 6.4 the differences in the modeled average surface CO mixing ratios for February 1999 and 1998, 1997 and 1996. Overall, February 1999 was more polluted than the other years for most parts of the Bay of Bengal and the southern Arabian Sea. The plume of enhanced CO mixing ratios over the Indian Ocean is located along the northeasterly boundary layer flow. This indicates that during 1999 the northeasterly flow was different from those during the other years. The differences become smaller when the

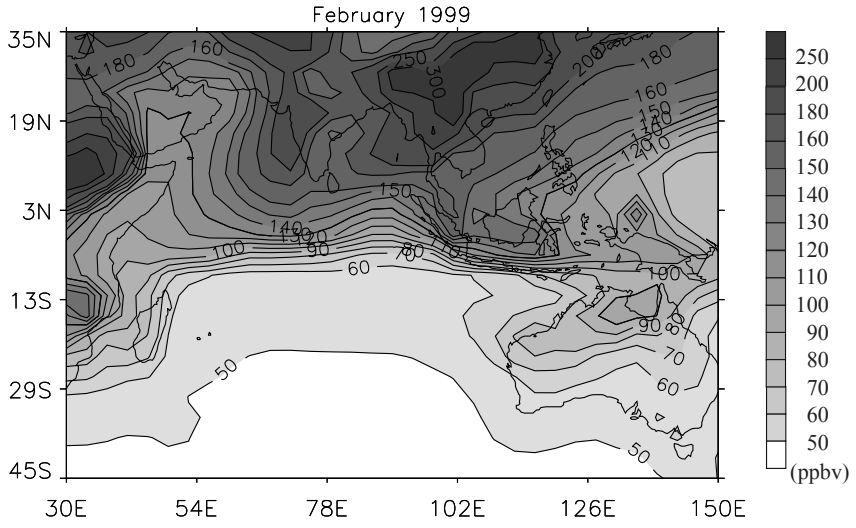

Figure 6.3 Average model calculated CO surface mixing ratios (ppbv) over the northern Indian Ocean during February 1999.

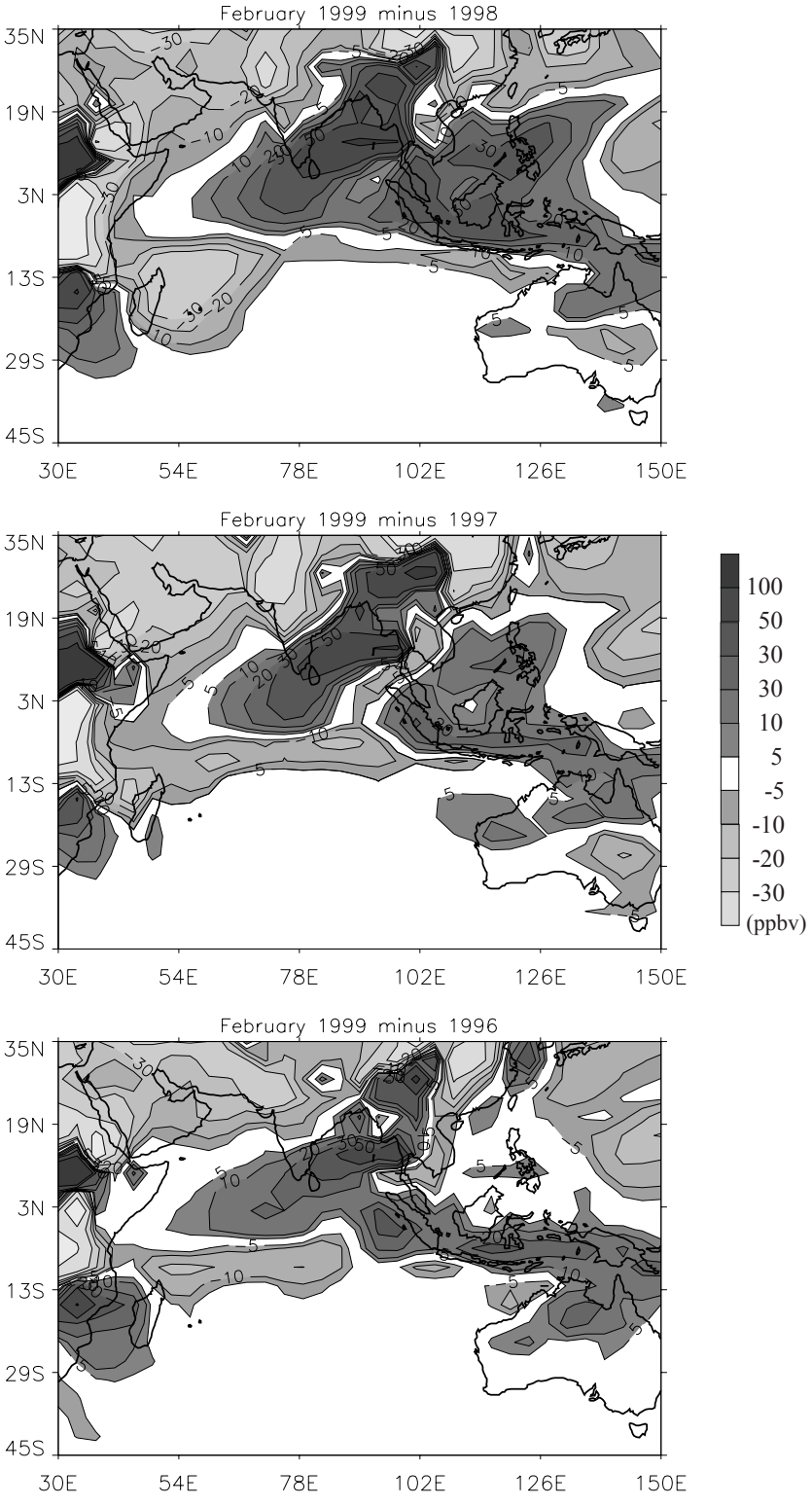

Figure 6.4 Average differences in model calculated CO surface mixing ratios (ppbv) over the Indian Ocean between February 1999 and 1998, 1997 and 1996 respectively.

airmasses approach the ITCZ, situated around 10°S. Around 15°S an area with negative CO mixing ratio differences exist, indicating that during 1999 the pollution advanced less far south. The differences are largest for 1999-1998, smaller for 1999-1997 and smallest for 1999-1996. Furthermore, during 1998 an area with relatively high CO mixing ratios compared to 1999 is found east of Madagascar. This is caused by the occurrence of deep convection east of Madagascar during the El Niño year. The transport of polluted northern hemispheric air masses reaches further south during 1998 than during the other years.

Figure 6.5 shows the average surface wind field for the four different years. For all years northeasterlies and southeasterlies are found north and south of the equator. However, large differences occur around the equator. During 1997 and 1996 strong convergence takes place around 10°-15°S. This indicates strong convection in the ITCZ. During 1999 and 1998 the convergence at the ITCZ is much weaker, associated with weaker convection. Furthermore, the 1998 El Niño year shows significant differences compared to the other years. In general the winds towards the ITCZ are weaker, and a cyclonic flow is found east of Madagascar.

Comparing the differences in CO mixing ratios with the differences in the surface wind fields, one can deduce how these differences occur. The northeasterlies over the Bay of Bengal and the Arabian Sea are strong in 1999, 1997 and 1996. This causes a constant strong advection of CO from the source regions in India and Southeast Asia.

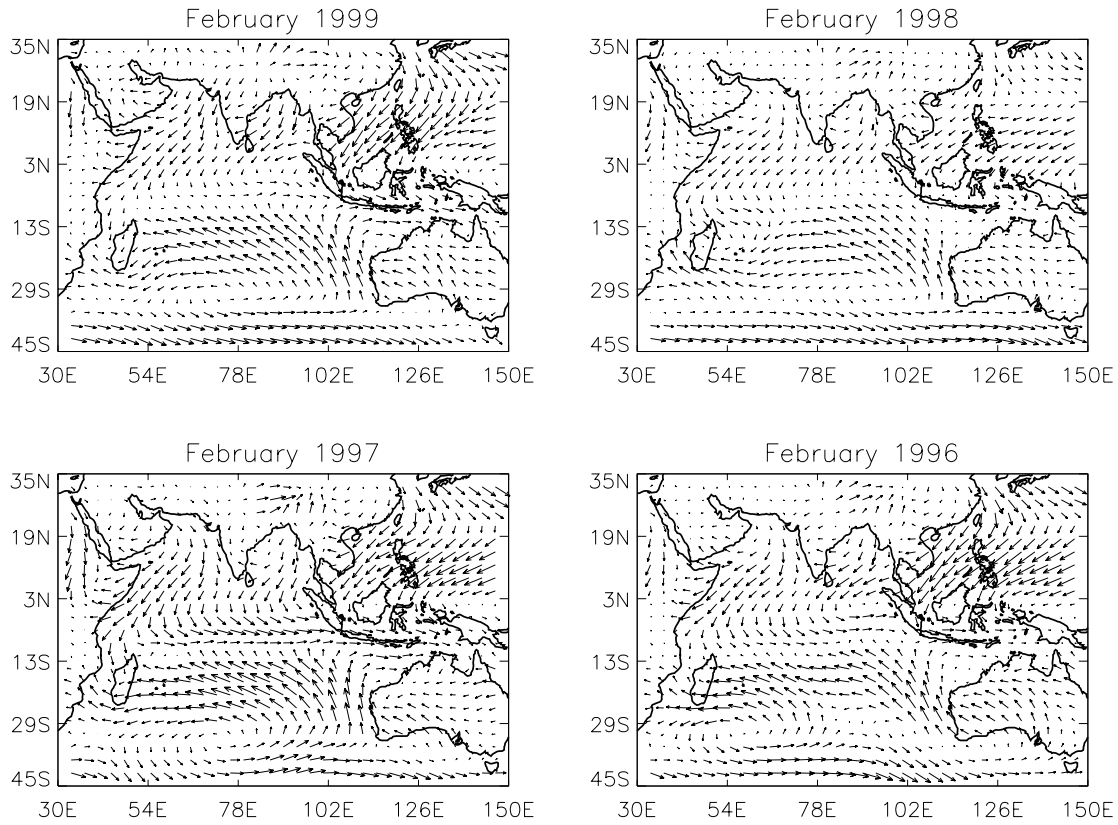

Figure 6.5 Average model calculated surface wind field (arrow length indicates wind speed in arbitrary units).

However, during 1999 the convergence at the ITCZ and the winds towards the ITCZ are much weaker than during 1997 and 1996. The weaker convergence and thus weaker convection cause less vertical transport during 1999 compared to 1997 and 1996. Because the continental outflow remains strong during 1999, CO accumulates over the northern Indian Ocean causing relatively high CO mixing ratios. The ITCZ is located further south during 1997 and 1996 compared to 1999, leading to slightly higher CO mixing ratios in a band around 15°S during 1997 and 1996.

Comparing 1997 with 1996 indicates that the ITCZ was more intense in 1997 than in 1996. This resulted in a less efficient advection and vertical transport during 1996, leading to higher CO mixing ratios during 1996 compared to 1997.

The differences in CO mixing ratios between 1999 and 1998 appear similar to the differences between 1999 and 1997-1996, but the explanation is different. Both during 1999 and 1998 the ITCZ is weak over the Indian Ocean. However, the continental outflow is also weak during 1998, whereas during 1999 it is strong. Hence, a significant part of the CO pollution never reaches the Indian Ocean in the first place during 1998, in contrast with 1999.

6.4 Discussion

Figure 6.6 shows the average modeled velocity potential at 190 hPa for February, and the corresponding divergent part of the wind field. The divergent part of the wind field is derived from the horizontal gradient in the velocity potential, with the wind direction from low to high values of the velocity potential. The lateral and transverse monsoon circulations can be clearly discerned. The changes in the convection strength are reflected in the modeled velocity potential. Strong outflow over the equatorial Indian Ocean is found during February 1996 and 1997, whereas during February 1999 the outflow is relatively weak over the western Indian Ocean with even an area of local convergence. This convergence results in descending air masses and suppressed convection. The increased convective activity east of Madagascar and the decreased convective activity over northern Australia during the February 1998 El Niño are also clearly visible.

Comparing 1999, 1997 and 1996, the equatorial outflow is strongest during 1997, somewhat weaker during 1996 and much weaker during 1999, especially over the western part of the Indian Ocean. This coincides with strong convection during 1997, somewhat weaker convection during 1996 and much weaker convection during 1999. This pattern can also be found in the average modeled precipitation rate in Figure 6.7, in which the changes in convective activity during the 1998 El Niño are visible, i.e. reduced convection over northern Australia and strong convection east of Madagascar.

According to Figure 6.1, the differences in CO mixing ratios in March between the different years are small,. An analysis of the circulation patterns and the convective activity for March 1996 to 1999 (Figure 6.8) reveals that an active phase of the MJO occurred during March 1999 and March 1996, while during 1997 the MJO was passive. The velocity potential (Figure 6.9) for March 1998 was similar to that of March 1997, indicating that El Niño reached its end and the circulation went back to normal, with a

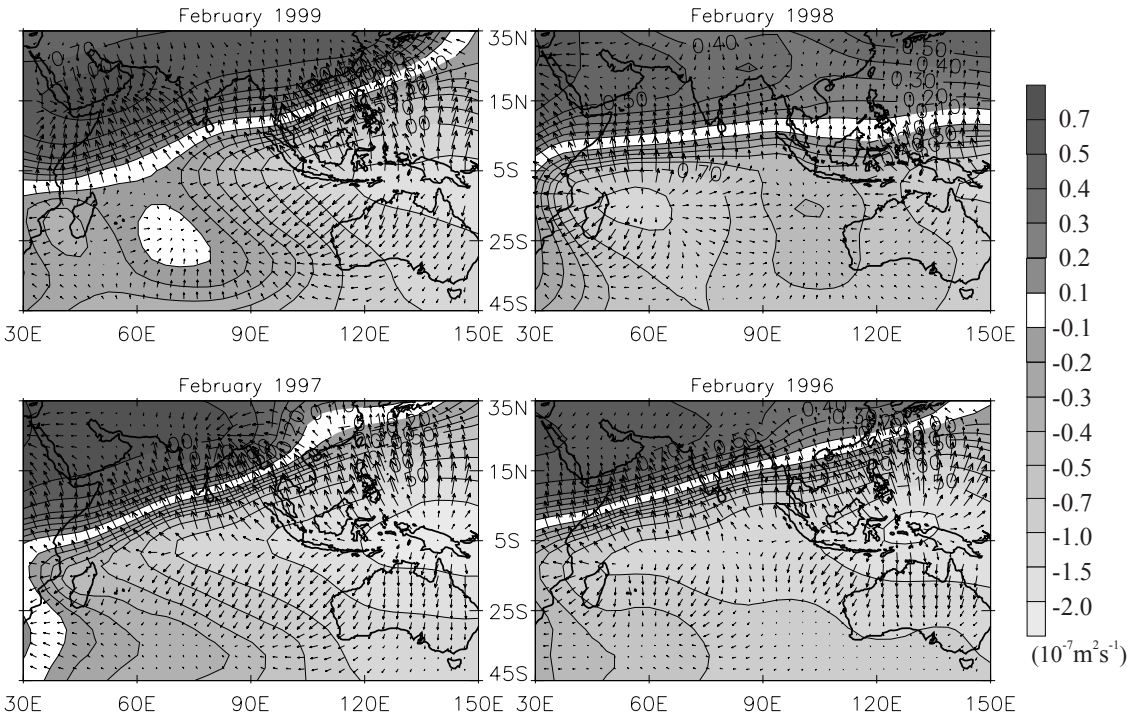

Figure 6.6 Average modeled velocity potential (*10^{-7} m^2s^{-1}) at 190 hPa, and the corresponding divergent wind field (arbitrary arrow length).

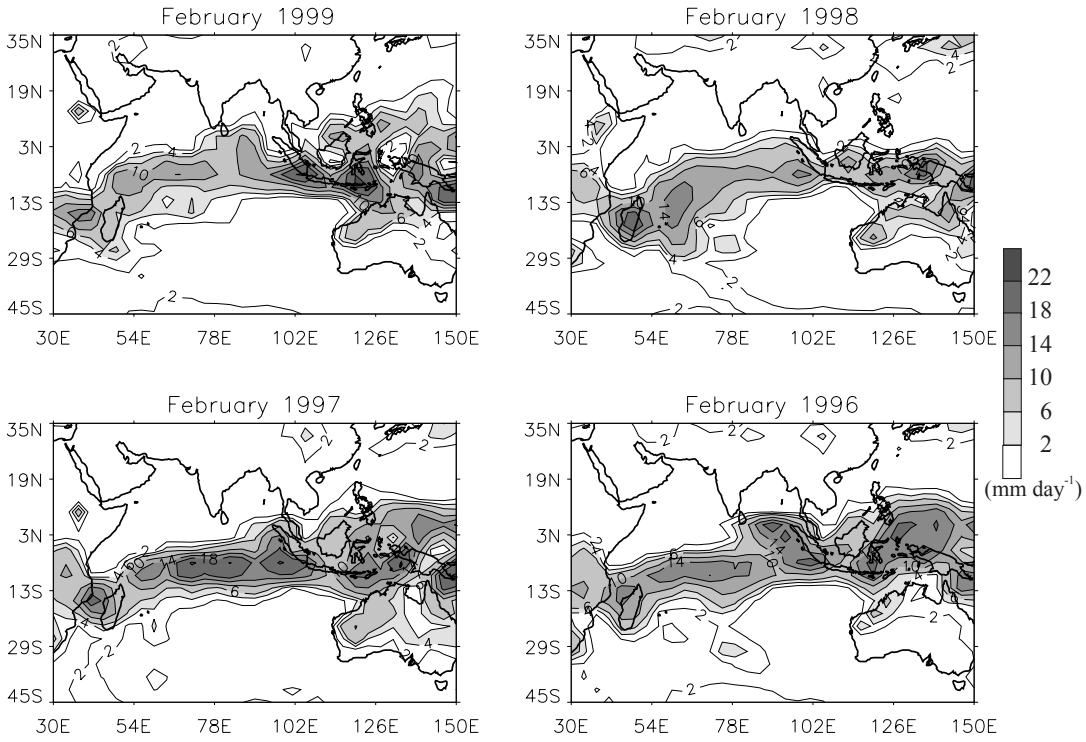

Figure 6.7 Average modeled precipitation (mm day^{-1}) for February 1996 to 1999.

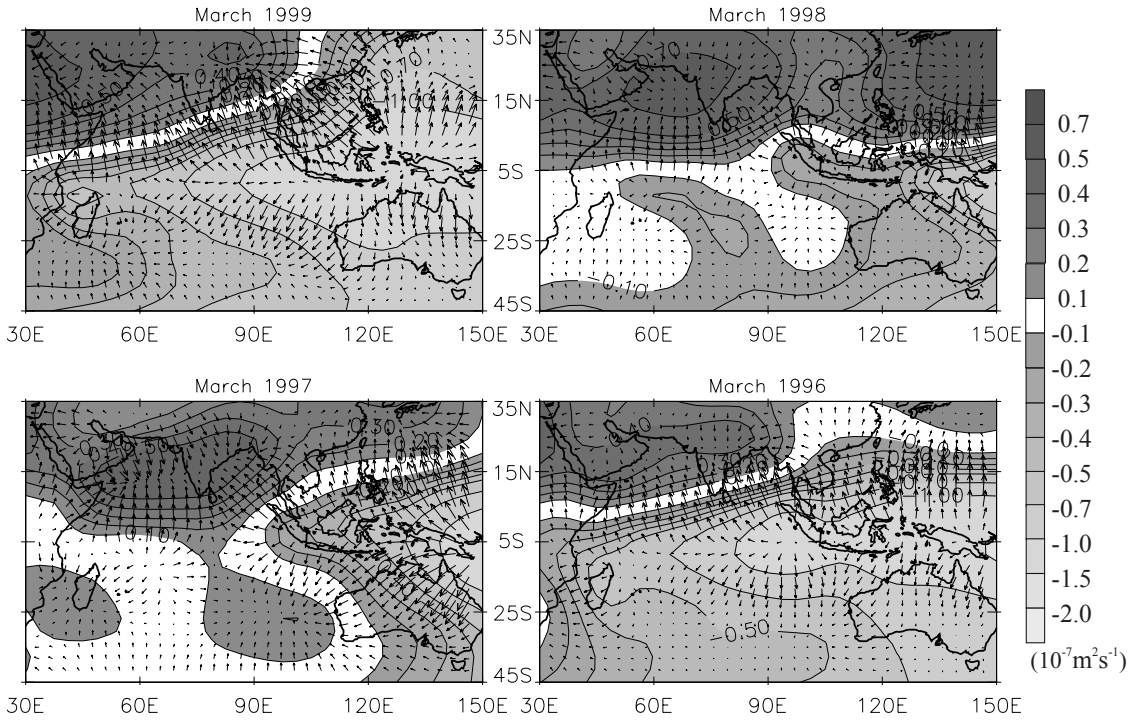

Figure 6.8 As Figure 6.6 but for March 1999, 1998, 1997 and 1996.

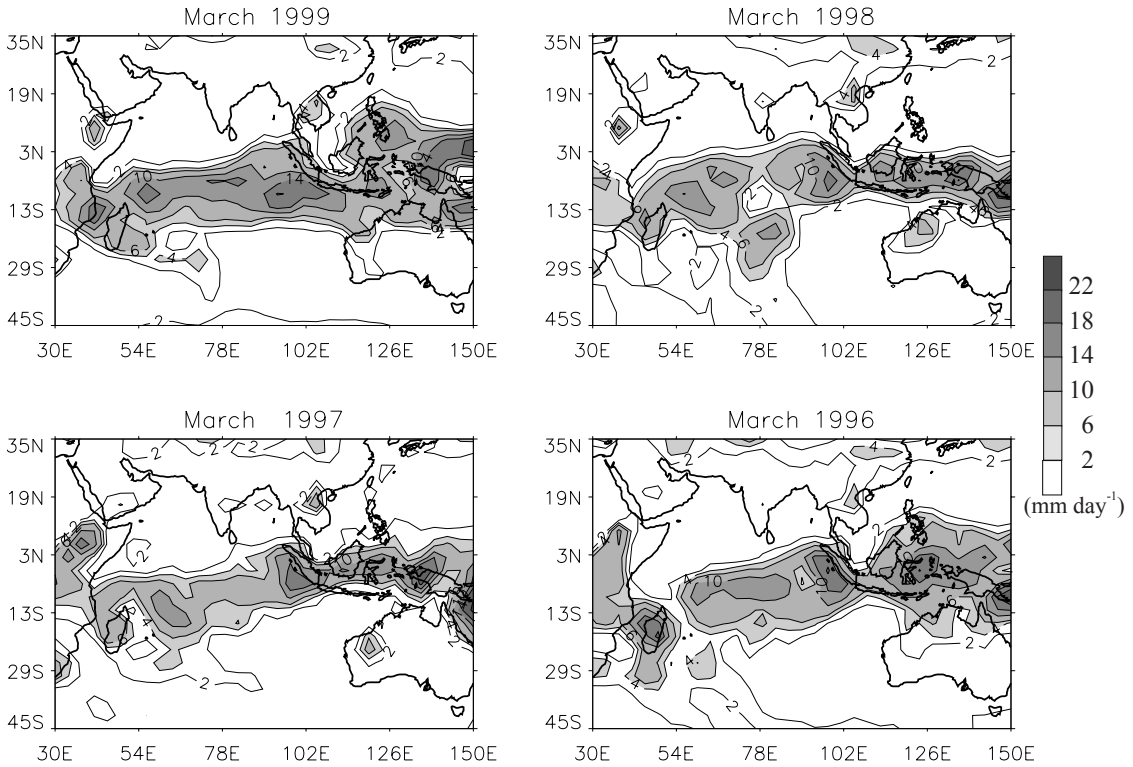

Figure 6.9 As Figure 6.7 but for March 1999, 1998, 1997 and 1996.

passive phase of the MJO. A similar pattern was found in the precipitation rate, with very weak convection during March 1997 and 1998. This does not result in large differences in CO mixing ratios as occurred during February, although the CO mixing ratios during March 1999 and 1996 are slightly higher than during 1998 and 1997. During March, the landmasses at the northern Indian Ocean rim become warmer due to the stronger solar radiation, resulting in a weakening of the high-pressure areas. This reduces the continental outflow considerably, and less polluted air masses are advected from the continent to the Indian Ocean. Because of the passive phase of the MJO and relatively weak convection, the pollution that reaches the Indian Ocean is not advected very far south during 1998 and 1997. During 1996 and 1999 active phases of the MJO occur, and the pollution that reaches the Indian Ocean is advected towards the ITCZ, resulting in higher CO mixing ratios over the equatorial Indian Ocean during 1999 and 1996 compared to 1998 and 1997.

6.5 Conclusions

The influence of the different processes on pollution advection over the northern Indian Ocean during the winter monsoon can be summarized as follows:

a) During an El Niño year the location of equatorial convection changes drastically. The convection over northern Australia weakens and strong convection occurs east of Madagascar. The weakening of convection over northern Australia weakens the lateral monsoon, which in turn lowers the surface pressure over the Asian continent. This leads to a reduction of the continental outflow, so that less pollution from southeast Asia reaches the Indian Ocean. The strong convection east of Madagascar contributes to a strong southward advection of polluted northern hemispheric air masses east of Africa.

b) The active and passive phases of the MJO cause large differences in the convection strength within the ITCZ. Strong convection enhances advection of air masses in the boundary layer towards the ITCZ and subsequent efficient and rapid vertical transport of the air pollution. Weak convection is associated with accumulation of polluted air masses in the marine boundary layer over the northern Indian Ocean.

c) The annual cycle of the monsoon circulation determines the strength of the continental outflow during different months. During February the outflow is strong due to strong subsidence north of the Indian Ocean. During March, because of the heating of landmasses north of the Indian Ocean, the high pressure system weakens which also reduces the continental outflow.

A summary of the listed above listed effects for February and March 1996 to 1999 is given in Table 1.

Month		Convection	Outflow	Pollution
February	1999	Weak	Strong	Very High
	1998	Weak (El Niño)	Weak	Low
	1997	Very Strong	Strong	Low
	1996	Strong	Strong	Moderate
March	1999	Strong	Weak	Low-Moderate
	1998	Weak	Weak	Low
	1997	Weak	Weak	Low
	1996	Strong	Weak	Low-Moderate

Table 1 Summary of the main convection and advection effects on mean pollution levels in the lower atmosphere over the northern Indian Ocean during February and March 1996 to 1999.

Thus, in normal (average) years the annual cycle in the continental outflow has the strongest outflow during mid-winter and weaker outflow during spring. During an El Niño year the outflow is weaker. During the 1998 El Niño year the sea surface temperatures (SST) over almost the entire Indian Ocean were about 1°C higher than during 1996, 1997 and 1999 [Webster *et al*., 1999]. Nevertheless, the ITCZ convection was still weak, despite the fact that, in absence of large scale forcing, the convection strength is highly dependent on the SST [e.g. Lau *et al*., 1997]. This illustrates the importance of EL Niño in the tropical circulation.

Furthermore, the convection strength in the ITCZ determines the efficiency of pollution advection towards the ITCZ and removal from the boundary layer. Active and passive phases of the MJO cause strong and weak convection in the ITCZ, respectively, and thus the strength of advection of air masses towards the ITCZ. The combination of these different processes determines the amount of pollution over the northern Indian Ocean. The high levels of CO over the northern Indian Ocean observed during INDOEX in February 1999, i.e. up to 50 % higher than in other years, can be understood as a concerted action from the MJO and El Niño. The improved insight into these large scale meteorological phenomena contributes to the understanding of air pollution in the region. Once pollution measurements over Indian and neighboring countries become available, our analysis can be extended to the south and southeast Asian region.

Chapter 7

Summary and discussion

Summary

This thesis focuses on the chemical composition of the atmosphere over the Indian Ocean during the winter monsoon period. Results from the 3-D global chemistry climate model ECHAM4 have been compared with observations using the "nudging" technique, which enables a direct comparison between observations and model results. The comparison reveals model weaknesses and provides indications where the model can be improved. On the other hand, the model results can be used to analyse the observations. Both approaches are used in the previous chapters.

In chapter 2 a comparison between ship measurements from the r/v Malcolm Baldrige obtained during a pre-INDOEX campaign in spring 1995 and ECHAM4 model results at T30 resolution was presented. The comparison of surface measurements of CO indicated that the model reproduces the general features of the observed CO mixing ratios in both clean and polluted air masses. The model also captures the transitions between the different air masses. For O_3 the model also captures the transitions, although modeled surface O_3 mixing ratios were overestimated by the model. The model did not reproduce the strong diurnal cycle as was observed during a number of days. This might be related by halogen chemistry [Dickerson *et al.*, 1999], not represented in the model. The model reproduces the observed surface pressure, including the diurnal cycle.

The model also reproduces the general features of the measured O_3 profiles, i.e. gradually increasing O_3 mixing ratios from the surface (20-30 ppbv) to about 250 hPa (80-100 ppbv), and a distinct O_3 minimum (20-40 ppbv) between 250 and 150 hPa. An analysis of the O_3 profiles with both the ECHAM4 model and trajectories based on ECMWF analyses showed that the O_3-rich air masses originated from biomass burning occurring over Africa north of the equator. These air masses were transported vertically by deep convection and then subsequently advected towards the Indian Ocean at high altitudes. The analysis also showed that the high tropospheric O_3 minimum was caused by vertical displacement of O_3 depleted boundary layer air masses, caused by strong convection associated with the tropical cyclone Marlene during February 1995.

In chapter 3 a detailed analysis was presented of the diurnal O_3 cycle as observed at the KCO site on the Maldives. It was shown that the model reproduces the observed diurnal O_3 cycle, i.e. daytime decrease of O_3 mixing ratios and a nighttime increase. The recent theory about the nighttime increase of O_3 mixing ratios in the marine boundary layer is that it is caused by vertical transport of O_3-rich free-tropospheric air masses. It was explained why this process cannot be simulated by the model, and therefor cannot be the reason for the nightime O_3 increase as simulated by the model. An alternative explanation was presented in which the nighttime increase is caused by horizontal advection of O_3-rich air masses because of the presence of an upwind O_3 gradient. In turn the gradient is caused by daytime photochemical O_3 depletion. It was shown that this explains the model results, and that this approach could explain a number of observations that could not be explained by the traditional approach. Finally, it was noted that for

chemistry studies with box-models both approaches lead to the same result, which does not make previous box model studies using the concept of O_3 entrainment to simulate the diurnal O_3 cycle in the marine boundary layer less credible (i.e. being right for the wrong reasons).

In chapter 4 a comparison of different CO measurements from the r/v Ron Brown, the Cessna Citation aircraft and the Kaashidhoo climate observatory with model results was presented. The observations were obtained during the IFP. It was shown that the model reproduces most of the surface CO measurements, including the sharp gradient at the ITCZ, with the exception of areas in the direct outflow from the Indian subcontinent. Furthermore, at higher horizontal resolution the model performance generally improved, and was better capable of reproducing the observed small-scale features.

It was explained that the discrepancies between modeled and measured CO mixing ratios close to the Indian coast were related to the sea breeze circulation occurring at the Indian coast. The sea breeze circulation lifts polluted continental air masses from the boundary layer to the free troposphere above the marine boundary layer. The model does not simulate the sea breeze circulation because it occurs on subgrid scales. Instead, continental pollution is directly injected into the modeled marine boundary layer. Therefore, modeled CO mixing ratios were higher than observed. The minimum horizontal resolution required to resolve the sea breeze circulation is less than 50 km. Therefore, the model performance did not improve by changing the model resolution from T30 (grid size ~ 400 km) to T63 (~ 200 km).

The comparison of measured and modeled vertical CO profiles showed that over the northern Indian Ocean a "C-shape" occurs. High CO mixing ratios were measured in the boundary layer, where the air originates directly from CO emission regions, and between 8 and 12 km altitude, the typical outflow region of deep convection. It was also shown that the model results pertaining to the region close to the ITCZ did not necessarily improve at higher resolution because the model cannot reproduce the exact location of the ITCZ very well.

An analysis of modeled CO, separated into different source categories and source regions, showed that Indian biomass burning is the most important CO source for the marine boundary layer over the northern Indian Ocean, in agreement with observatons of K^+ and CH_3CN. However, other sources can contribute significantly, especially in less polluted air masses away from the Indian subcontinent. Furthermore, the most important free tropospheric CO source is the oxidation of hydrocarbons (notably CH_4). It was also shown that free tropospheric air masses are often affected by of a large number of sources, each contributing a small but significant amount to the total CO mixing ratio.

A comparison of the INDOEX region with other regions around the globe showed that the INDOEX region is rather unique with regard to its sources. In the boundary layer more than 85 % of the CO originated from biomass burning. For other regions biomass burning did not contribute more than 60 %, whereas most of these biomass burning sources are large-scale forest fires. For India the sources are mainly (small-scale) domestic fires.

In chapter 5 a comparison between measured and modeled NMHCs was presented. The model reproduced most of the measured acetone mixing ratios, except for areas close to the Indian subcontinent, where large discrepancies existed. As explained in chapter 4,

these discrepancies are related to the absence of the sea breeze circulation at the India coast in the model.

A comparison of the CO-acetone correlation showed that for polluted air masses the modeled and measured CO-acetone correlation are comparable, indicating that the model chemistry is correct. For less polluted air masses discrepancies exist between the modeled and measured CO-acetone correlation. The measured acetone mixing ratios are almost constant for CO mixing ratios below 100 ppbv. The modeled acetone mixing ratios continue to decrease with decreasing CO to near-zero acetone mixing ratios in clean air masses. A possible explanation is the presence of an oceanic acetone source, not represented in the model. Based on measurements it has been suggested in literature that such a source could exist. A simulation with an oceanic acetone source indicated that such a source could explain constant acetone mixing ratios concurrent with low CO mixing ratios. It also indicated that the oceanic acetone source could contribute significantly (25-50 %) to the currently estimated global source strength of acetone.

Because the effects of NMHCs on the chemistry are included in the NMHC model, it was possible to perform off-line calculations of NMHCs based on emission estimates and photochemical breakdown of the NMHCs by modeled OH. The comparison of analysed air samples with model results showed that the modeled mixing ratios are comparable to the measured ones, indicating that the emission inventory used for the simulation provides credible results.

A similar simulation was performed for acetonitrile, an excellent indicator for biomass burning emissions. The comparison of modeled and measured acetonitrile as well as the CO-acetonitrile correlation showed that large discrepancies existed. These discrepancies could be related to a missing acetonitrile sink, possibly dry deposition at the ocean surface. Although acetonitrile is only moderately soluble in water, this sink can significantly contribute to the total acetonitrile budget because acetonitrile is also very slowly removed from the free troposphere. A model simulation with an oceanic sink based on the solubility of acetonitrile in water improved both the acetonitrile mixing ratios and the CO-acetonitrile correlations.

Discrepancies between measured and modeled acetonitrile also existed in the free troposphere. Modeled acetonitrile mixing ratios were almost constant with height, whereas the measurements showed a decrease with altitude. This could be related to the absence of a stratospheric sink of acetonitrile in the model. A stratospheric sink would result in low stratospheric mixing ratios, and stratosphere-troposphere exchange can cause a decrease in free tropospheric mixing ratios. The contribution of stratosphere-troposphere exchange is more important at high altitudes, which may explain the decrease in observed mixing ratios with altitude.

In chapter 6 we looked at the dynamics of the winter monsoon circulation and the interannual variability. The INDOEX observations from 1999 and 1998 showed that 1999 was much more polluted than 1998, especially during February. The obvious question was what caused the differences. Model simulations showed a very similar variability as evident from the observations. A model analysis resulted in the following theory.

The northeasterlies over the northern Indian Ocean during the winter monsoon occur because of a surface pressure gradient between the Asian continent (high pressure) and the ITCZ (low pressure). The strenghht of the pressure gradient is caused by the strength of the ITCZ and the continental high pressure. Strong convection at the ITCZ results in a

lower surface pressure and efficient transport of air masses from the surrounding oceans towards the ITCZ. Strong continental surface pressure causes a strong surface outflow from the continent towards the northern Indian Ocean.

Three processes dominate the strength of the ITCZ and the continental high pressure: the annual monsoon cycle, El Niño and the Madden-Julian oscillation. During a normal average year the continental high pressure strengthens and weakens with the cooling and heating of the land surfaces because of the decreases and increases in solar radiation. This means that for March, when the continents are warmer than during February, the continental high pressure is weaker, causing a smaller pressure gradient over the continent, resulting in weaker continental outflow. The weakened continental outflow causes a decrease in pollution advected from the continents to the ITCZ.

Another process that weakens the continental high pressure is El Niño. During the winter monsoon the continental high pressure is connected to the monsoon convection over northern Australia by the transverse monsoon. During an El Niño year this convection weakens considerably, thus weakening the continental high pressure, which weakens the pressure gradient and the continental outflow. This is what occurred during February 1998. El Niño also weakened the strength of the ITCZ, but because the outflow was weak to start with, the weakening of the convection did not strongly affect the amount of pollutants.

However, when the continental outflow is strong during a normal year, a weakening of the convection considerably affects the pollutant transport. The main process causing weakening and strengthening of the ITCZ is the MJO (by definition). During passive phases of the MJO the convection is weak, whereas during active phases the convection is strong. During February 1999 the MJO was in an inactive phase. The continental outflow was strong. Pollution was advected from the continent towards the northern Indian Ocean, but there was no subsequent efficient vertical displacement of boundary layer air by the ITCZ. Hence, pollution accumulated. During other years, like February 1996 and 1997, the MJO was in an active phase. Polluted air masses were removed efficiently from the boundary layer, causing lower pollution levels in the marine boundary layer. Similar passive and active phases of the MJO could be found for the modeled March months from 1996 to 1999, although the average differences in pollutant levels between the months were smaller because the continental outflow was weaker as part of the normal annual cycle.

Final remarks

We have shown in this thesis that the nudged ECHAM4 model is capable of reproducing the chemical composition of the atmosphere over the Indian Ocean, as long as the measured features are related to large scale phenomena. This thesis also provides strong indications about discrepancies between model results and measurements exist and where the model can be improved.

In general discrepancies between model results and measurements occurred when observed features were related to processes taking place on scales smaller than the model grid size. The most important model weaknesses for the Indian Ocean area are summarized below

1 Sea breeze circulation at the Indian coast.

A comparison between modeled and measured O_3 profiles over KCO [not presented in this thesis, see Lelieveld *et al.*, 2001] shows that, averaged over a longer period of time, modeled and measured free tropospheric O_3 profiles are comparable. In the boundary layer there still exists a difference because of the influence of the sea breeze circulation; too high modeled surface O_3 mixing ratios, and too low "trade-wind" layer O_3 mixing ratios. However, it appears that, on average for the entire lowest 3 km, modeled O_3 mixing ratios are comparable to the measured ones. This indicates that for large spatial and time scales, the errors in the advection of O_3 is not as large as it appears initially, based on individual O_3 soundings. At larger distances from the Indian coast the absence of the sea breeze circulation mostly affects trace gases that experience large changes in mixing ratios over land during the course of day, and which have a sufficiently long photochemical lifetime to be advected over large distances. An important example of such a trace gas is O_3, produced over land during the day and being deposited during the night. CO is less affected by this effect, mainly because there are no large differences in chemical behaviour between night and day (no surface deposition). This is confirmed by the comparison of both modeled surface CO and O_3 mixing ratios with measurements. O_3 mixing ratios are overestimated by the model over large parts of the Indian Ocean, whereas modeled CO mixing ratios are overestimated close to the Indian coast, but further away they are comparable to the observations. This is caused by vertical mixing of the lowest 3 km of the atmosphere further away from the continents.

2 Free tropospheric layers with enhanced O_3 over the northern Indian Ocean related to stratosphere troposphere exchange.

The observations often show shallow vertical layers of enhanced O_3 mixing ratios on subgrid model scales. The model reproduces these stratosphere-troposphere events, but due to the coarse vertical resolution the stratospheric air masses are smeared out vertically. The layering of stratospheric air masses occurs because they are very dry and stable. Mixing with the surrounding air masses is suppressed in the slowly descending air masses over the northern Indian Ocean, and other perturbing processes like deep convection do not occur in this area during the winter monsoon.

3 Free tropospheric layers with enhanced CO and O_3 over the western Indian Ocean related to convective transport of biomass burning plumes.

Again, the model resolution is too coarse to resolve the shallow plumes. In addition the horizontal resolution is too coarse to resolve individual convective cells. Modeled vertical transport by convection occurs over the entire gridbox, whereas in reality it occurs scattered over the gridbox. This causes discrepancies between model and observations. Additionally, it can be shown that with the low vertical resolution the modeled outflow of deep convective cells always occurs at the same altitude. In reality the outflow occurs over a broader range of altitudes, dependent on the strength of

individual convective cells. This also causes layering of polluted air masses, which the model cannot simulate.

4 Boundary layer structure over the Indian Ocean.

The observations show that over the Indian Ocean the boundary layer often can be subdivided into two layers: the marine boundary layer and the trade-wind layer. The model cannot reproduce this structure because of the low vertical resolution. This might cause some additional discrepancies. Krishnamurty *et al*. [1997] have shown that in the trade-wind layer the general wind direction is east-west, while in the marine boundary layer it is northeast-southwest. In the model the winds blow strictly from the northeast to the southwest. The sea breeze circulation advects significant amounts of air pollution into the trade-wind layer, and part of the pollution may not be advected to the ITCZ, but to Arabia and northeastern Africa. In the model no such separation exists, and all air masses are advected to the ITCZ. Unfortunately no observations are currently available to assess the magnitude of this discrepancy.

5 Exact location of the ITCZ

The model reproduces the sharp transitions between different air masses over the Indian Ocean, however, the observations also show that these transitions often occur on subgrid scales. The transition of the air masses at the ITCZ are closely related to the occurrence of convection; as discussed above, the model does not reproduce the location of individual convective cells very well.

It can be expected that the most important model weaknesses become smaller with increasing model resolution because they are resolution related. The comparison between observed and modeled surface CO from the R/V Ron Brown at two different resolution (T30 and T63, Chapter 4) confirms that this is the case for a number of processes, however, this does not apply to the sea breeze circulation.

Figure 7.1 and 7.2 illustrate the differences that occur at different model resolutions, and it provides a flavour of the model capabilities and deficiencies. The figure shows an infrared picture from the Meteosat-5 satellite over the Indian Ocean and the corresponding modeled surface velocity field at the two resolutions.

We can clearly see that clouds and cloudy areas correspond with features in the modeled wind field, like the convection west and north of Madagascar, around the equator south of India towards Indonesia and the circulation around a tropical cyclone present south of India over the southern Indian Ocean. We can also see that, although the model simulates the large-scale circulation at T30 resolution, it is too coarse to resolve many of the smaller scale features. At T63 resolution the model is better capable of simulating the smaller scale cloud bands and cloudy areas that are visible in the satellite picture. Still, a number of discrepancies remain, like the differences between the exact and modeled position of the tropical cyclone.

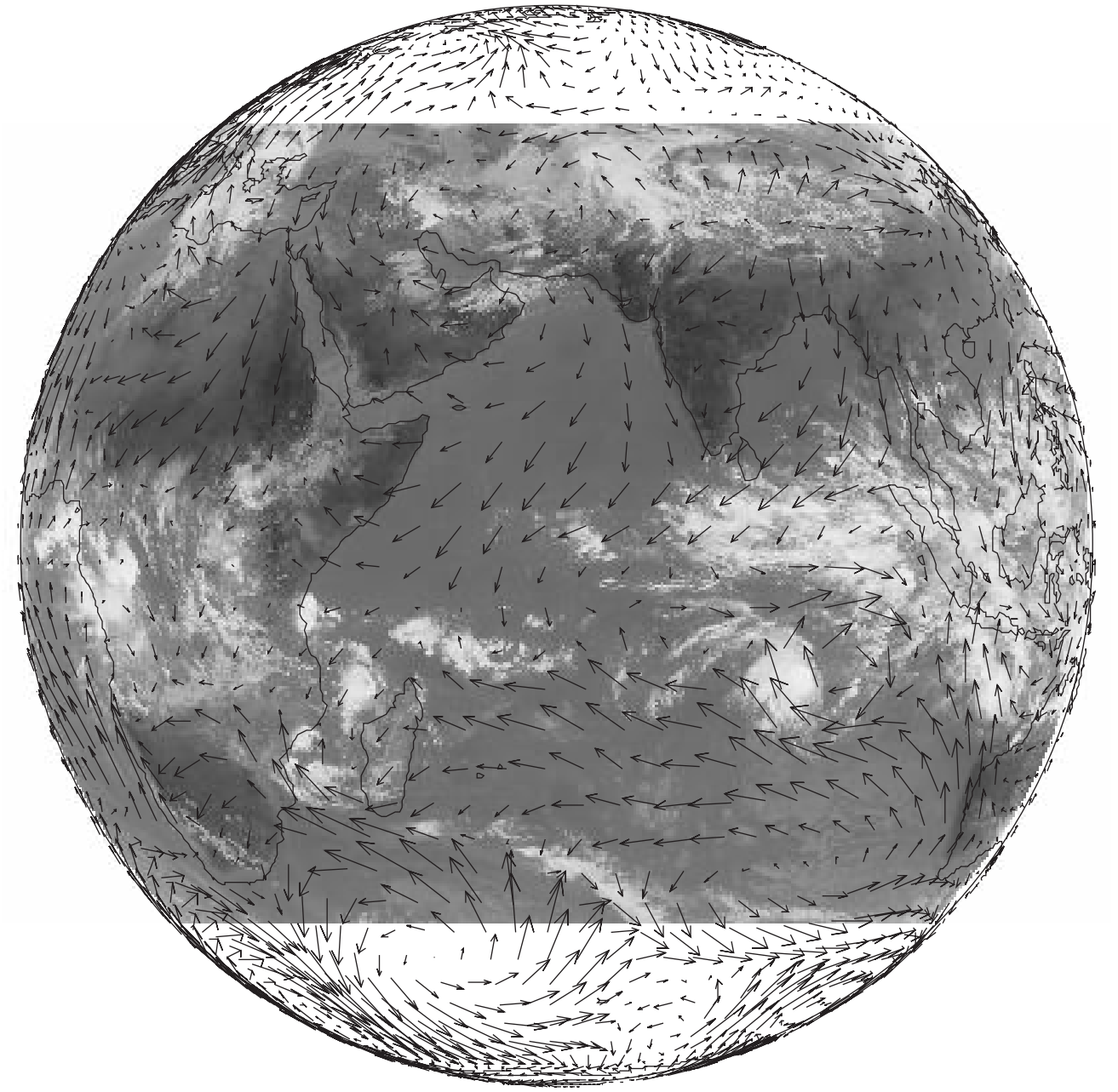

Figure 7.1 ECHAM modeled surface wind field at T30 resolution and the corresponding Meteosat-5 infrared image for 4 March 1999, 12:00 UTC. The arrow length indicates the wind speed in arbitrairy units.

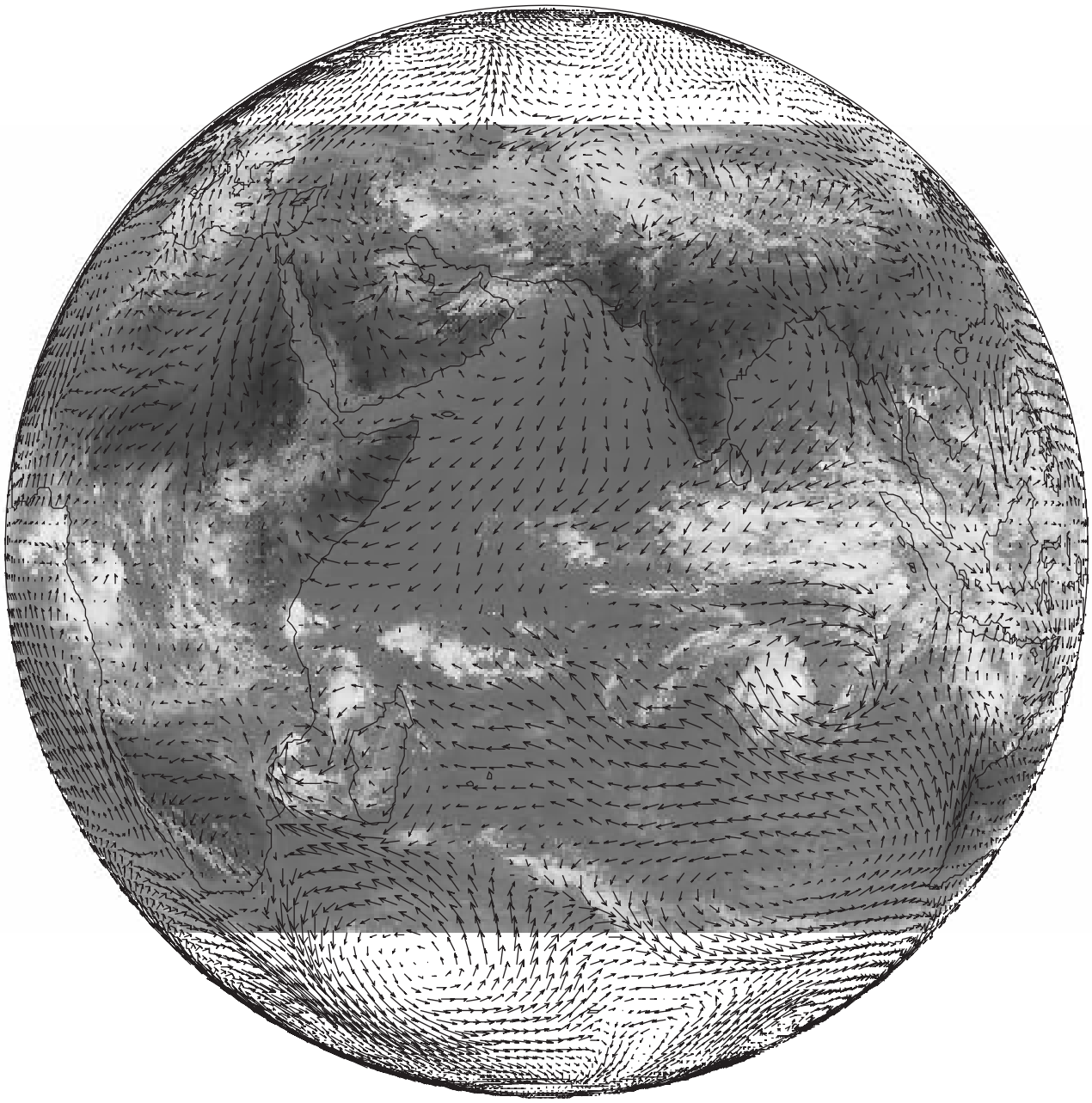

Figure 7.2 As Figure 7.1 but with ECHAM modeled surface wind fields at T63 resolution

APPENDIX

A.1 The ECHAM model

The "governing equations" on which the model dynamics are based [Adopted from DKRZ technical report No 6, Hamburg, 1992]

$$\frac{d\vec{v}_h}{dt} = -\frac{1}{\rho}\nabla_h p - 2(\vec{\Omega} \times \vec{v}_h)_h - \frac{1}{\rho}\frac{\partial J_{\vec{v}_h}}{\partial z} + K_{\vec{v}_h} \tag{A.1}$$

$$\frac{dT}{dt} = \frac{R_d T_v}{pC_p}\frac{dp}{dt} + \frac{1}{\rho}\left(Q_R + Q_L + Q_D - \frac{1}{\rho}\left[\frac{\partial J_S}{\partial z} - C_{pd}T(\delta - 1)\frac{\partial J_{q_v}}{\partial z} \right] \right) + K_T \tag{A.2}$$

$$\frac{dq_v}{dt} = S_{q_v} - \frac{1}{\rho}\frac{\partial J_{q_v}}{\partial z} \tag{A.3}$$

$$\frac{dq_w}{dt} = S_{q_w} - \frac{1}{\rho}\frac{\partial J_{q_w}}{\partial z} \tag{A.4}$$

$$p = \rho R_d T_v \tag{A.5}$$

$$\frac{\partial p}{\partial z} = -g\rho \tag{A.6}$$

with

$$T_v = T(1 + (\frac{1}{\varepsilon} - 1)q_v) \tag{A.7}$$

and

$$C_p = C_{pd}(1 + (\frac{C_{pv}}{C_{pd}} - 1)q_v) \tag{A.8}$$

C_p = specific heat of moist air at constant pressure
C_{pd} = specific heat of dry air at constant pressure
C_{pv} = specific heat of water vapour at constant pressure
g = acceleration of gravity
J_χ = vertical eddy flux of variable χ
K_χ = tendency of variable χ due to horizontal diffusion
p = pressure
q_v = water vapour mixing ratio
q_w = cloud water mixing ratio
Q_D = heating rate due to unorganized transfers between enthalpy and sub-grid scale kinetic energy
Q_L = heating rate due to heat release associated with internal phase changes
Q_R = heating rate due to heat transferred from falling rain and snow
R_d = gas constant for dry air
S_{qv} = change of q_v due to condensation or evaporation
S_{qw} = change of q_w due to condensation, evaporation or precipitation
t = time
T = temperature
T_v = virtual temperature
$\vec{v}_h$ = horizontal wind vector
z = height
δ =C_{pv}/C_{pd}
ρ = air density
Ω = angular velocity of earth

Spectral model

- The model uses a spectral representation of the dynamic fields, with the prognostic variables expanded in terms of spherical harmonics with triangular truncation at a specified wavenumber.

- Non-linear and physical terms are calculated on a Gaussian grid.

Horizontal resolution

	Grid size	**Timestep**
T30	3.75˚ × 3.75˚	1800 s
T63	1.9˚ × 1.9˚	900 s

Vertical resolution

A hybrid σ-p vertical coordinate system (σ = pressure/surface surface) pressure. At the surface the layers follow the orography, whereas at the top layers are at constant pressure levels. The hybrid σ-p vertical coordinate system is computationally efficient.

Pressure levels (19 Layers, the lowest 16 given here)

hPa	**km**
990	0.03
970	0.14
950	0.38
900	0.78
840	1.4
760	2.1
670	3.1
580	4.2
490	5.6
400	7.0
320	8.6
250	10.2
190	11.9
140	13.8
100	15.9
75	18.0

Prognostic model variables:

- Vorticity
- Divergence
- Temperature
- Log surface pressure
- Water vapour
- Cloud water

Radiation

- Two stream approximation [Hense et al, 1982, Rockel *et al*., 1991, Eickerling, 1989]

Horizontal transport of tracers

- Semi-Lagrangian advection scheme [Rasch and Williamson, 1990]

Vertical transport:

- Vertical diffusion [Roeckner *et al*., 1996]

- Convective mass-flux scheme [Tiedke, 1989]

A.2 CH_4-CO-NO_x-HO_x chemistry scheme

The standard CH_4-CO-NO_x-HO_x uses an Eulerian Backward Iterative (EBI) scheme to calculate chemical reactions [Roelofs and Lelieveld, 1995, 1997]. It basically describes:

- ✓ CH_4 oxidation to CO and CO_2
- ✓ formation and destruction of nitric oxides like NO and NO_2
- ✓ O_3 formation and destruction
- ✓ OH and HO_2 radical formation and destruction

It includes:

- Formation of HNO_3 through reaction of N_2O_5 on aerosols
- OH formation by reaction of $O(^1D)$ with H_2O using modeled water vapour mixing ratios
- Photolysis rates based on modeled meteorological parameters and climatological O_3 columns.
- Stratosphere-troposphere exchange that is determined by simulated dynamics. The simulated tropopause is marked by a potential vorticity of $3.5 \cdot 10^{-6}$ K m^2 kg^{-1} s^{-1} poleward of 20° latitude [Hoerling *et al.*, 1993], and by a -2 K km^{-1} temperature lapse rate equatorward of 20° latitude.
- O_3 mixing ratios that are prescribed in the stratosphere from 2-3 layers above the tropopause towards the top of the model, based on results from a 2-D troposphere-stratosphere chemical model [Brühl and Crutzen, 1988]. The tropospheric chemistry scheme does not fully account for O_3 production and destruction in the stratosphere
- Dry deposition of O_3, NO_x, and HNO_3 [Ganzeveld and Lelieveld, 1995]. Deposition calculated based on modeled meteorological parameters.
- Wet scavenging of HNO_3 and H_2O_2 using modeled precipitation rates [Roelofs and Lelieveld, 1995, 1997]

EMISSIONS

The standard model emissions of NO and CO are summarized in Table A.1. The biomass burning sources of NO is distributed according to Hao and Liu [1994]. NO emissions from soils are distributed according to Yienger and Levy [1995], whereas the lightning source is parameterized according to Price and Rind [1992]. CO emissions are distributed according to Lelieveld and Van Dorland [1995]. The total NO and CO emissions considered in the model are 37.5 Tg N yr^{-1} and 1900 Tg CO yr^{-1}, consistent with IPCC [1994]. In view of the relatively long lifetime of CH_4, the CH_4 surface concentrations are prescribed.

Source	**Specie**	**Source strength**
Biomass burning	NO	6 Tg N yr^{-1}
Soils	NO	5.5 Tg N yr^{-1}
Lightning	NO	5 Tg N yr^{-1}
Fossil fuels	NO	21 Tg N yr^{-1}
Biomass burning	CO	700 Tg CO yr^{-1}
Fossil fuel use	CO	450 Tg CO yr^{-1}
Vegetation	CO	100 Tg CO yr^{-1}
Natural NMHCs	CO	280 Tg CO yr^{-1}
Anthropogenic NMHCs	CO	300 Tg CO yr^{-1}
Wildfires	CO	30 Tg CO yr^{-1}
Oceans	CO	40 Tg CO yr^{-1}

Table A.1 Emission sources and strengths as used in the standard CH_4-CO-NO_x-HO_x chemistry scheme.

In chapter 4 we also use the CO emissions based on the EDGAR v2.0 emission inventory [Olivier *et al.*, 1996].

A.2 Non-Methane-Hydrocarbon chemistry scheme

The model version: the Carbon Bond Mechanism 4 (CBM-4) with extended acetone and isoprene chemistry [Gery *et al.*, 1989; Houweling *et al.*, 1998]. Emissions for CO and NO are similar to those summarized in table 1.2, with the exception of CO originating from NMHCs. This process is explicitly described with the CBM-4 scheme. Results from this model version at T30 are discussed in Roelofs and Lelieveld [2000].

Spatial distributions of NMHC emissions from industry, biomass burning and other combustion sources is implemented using the EDGAR V2.0 emission inventory [Olivier *et al.*, 1996], adding up to 90 Tg C yr^{-1}.

NMHC emissions from biomass burning amount to 19.4 Tg C yr^{-1}, with contributions by paraffinic carbon bond hydrocarbons and ethene of about 50% and 25%, respectively. Biomass burning emissions are distributed according to Hao and Liu [1994].

An annual global source of isoprene of 400 Tg C yr^{-1} is considered according to the spatial distribution from the GEIA emission inventory [Guenther *et al.*, 1995]. The diurnal variation of isoprene emissions is obtained by using the simulated shortwave radiative flux at the surface as a weighting factor.

Acetone is formed in the atmosphere through the oxidation of propane and other hydrocarbons. Since propane is neither explicitly nor implicitly represented in the chemistry scheme, the approach of Wang *et al.* [1998] is followed, and a direct source of acetone was included, assuming an 80% yield from the oxidation of propane of which the anthropogenic emission amounts to 7.8 Tg C yr^{-1} (EDGAR V2.0 inventory). Additionally, 2.3 Tg C yr^{-1} of acetone is emitted from vegetation, distributed in the same way as isoprene [Guenther *et al.*, 1995]. Formation of acetone from precursor NMHCs (isobutane and isobutene) is included in the CBM-4 scheme.

The dry deposition parameterization of Ganzeveld *et al.* [1998], which derives aerodynamic and stomatal resistances directly from parameters calculated by ECHAM, is extended to include formaldehyde, aldehydes, PAN and organic nitrates. Wet deposition of formaldehyde and methylperoxide is parameterized analogously to H_2O_2 and HNO_3 [Roelofs and Lelieveld, 1995]. Wet deposition of organic nitrates, not very soluble, has been neglected.

In addition, the parameterization for the calculation of photodissociation rates in this model version is from Landgraf and Crutzen [1998]. Photodissociation rates are evaluated each time step using chemical (stratospheric ozone) and meteorological parameters (pressure, temperature, cloud distribution and humidity) provided online by the GCM.

Bibliography

Anderson, B.E., G.L. Gregory, J.D.W. Barrick, J.E. Collins, G.W. Sachse, C.H. Hudgins, J.D. Bradshaw and S.T. Sandholm: Factors influencing dry season ozone distributions over the tropical south Atlantic, *J. Geophys. Res., 98*, 23,491-23,500, 1993.

Arijs, E., and G. Brasseur, Acetonitrile in the stratosphere and implications for positive ion composition, *J. Geophys. Res., 91,* 4003-4016, 1986.

Ayers, G.P., S.A. Penkett, R.W. Gillett, B. Bandy, I.E. Galbally, C.P. Meyer, C.M. Elsworth, S.T. Bentley and B.W. Forgan: Evidence for photochemical control of ozone concentrations in unpolluted marine air, *Nature, 360*, 446-449, 1992.

Ayers, G.P., S.A. Penkett, R.W. Gillett, B. Bandy, I.E. Galbally, C.P. Meyer, C.M. Elsworth, S.T. Bentley and B.W. Forgan: Then annual cycle of peroxides and ozone in marine air at Cape Grim, Tasmania, *J. Atmos. Chem., 23*, 221-252, 1996.

Ayers, G.P., H. Granek and R. Boers, Ozone in the MBL at Cape Grim, model simulation, *J. Atmos. Chem., 27*, 179-195, 1997.

Baldy, S., G. Ancellet, M. Bessafi, A. Badr and D. Lan Sun Luk: Field observations of the vertical distribution of tropospheric ozone at the island of Reunion (southern tropics). *J. Geophys. Res.*, *101*, 23.835-23.849, 1996.

Benkelberg, H.J., S. Hamm, and P. Warneck, Henry's law coefficients for aqueous solutions of acetone, acetaldehyde and acetonitrile, and equilibrium constants for the addition compounds of acetone and acetaldehyde with bisulfate, *J. Atmos. Chem., 20*, 17-34, 1995.

Brasseur, G., E. Arijs, A. de Rudder, D. Nevejans, and J. Ingels, Acetonitrile in the atmosphere, *Geophys. Res. Let., 10,* 725-728, 1983.

Brasseur, G.P., J.J. Orlando and G.S. Tyndall, 1999: Atmospheric Chemistry and Global Change, Oxford University press, 654 pp.

Bremaud, P., J.F. Taupin, A.M. Thompson and N Chaumerliac: Ozone nighttime recovery in the marine boundary layer: Measurement and simulation of the ozone diurnal cycle at Reunion Island, *J. Geophys. Res.*, *103*, 3463-3473, 1998.

Brill, K.F., L.W. Uccellini, J. Manobianco, P.J. Kocin and J.H. Homan, The use of successive dynamic initialization by nudging to simulate cyclogenesis during GALE IOP 1, *Meteorol. Atmos. Phys., 45,* 15-40, 1991.

Brühl, C. and P.J. Crutzen, Scenarios of possible changes in atmospheric temperatures and ozone concentrations due to man's activities estimated with a one dimensionsal coupled photochemical climate mode, *Clim. Dyn,* 2, 173-203, 1988.

Chen, C.T., and E. Roeckner, Validation of the earth radiation budget as simulated by the Max Planck Institute for Meteorology general circulation model ECHAM4 using satellite observations of the Earth Radiation Budget Experiment, *J. Geophys. Res., 101,* 4269-4287, 1996.

Chester, R., A.S. Berry and K.J.T. Murphy: The distribution of particulate trace metals and mineral aerosol over the Indian Ocean. *Marine Chemistry*, *43*, 261-290, 1991.

Coakley, J.A. Jr., B. Gandrud, T. Bates, A. Clarke, W. Collins, R. Dickerson, F.Dulac, J. Heintzenberg, T.N. Krishnamurti, A. Jayaraman, V. Ramanathan, R.Sadourny and J. Williams, General overview of INDOEX, *submitted to J. Geophys. Res.,*

Crutzen, P.J., Photochemical reactions initiated by and influencing ozone in unpolluted tropospheric air, *Tellus, 26*, 47-57, 1974.

Crutzen, P.J., Tropospheric Ozone: An overview, *Tropospheric Ozone,* edited by I.S.A. Isaksen, Riedel Publishing Company, 1988.

Crutzen, P.J., M. Lawrence, and U. Pöschl, On the background photochemistry of tropospheric ozone, *Tellus, 51A*, 123-146, 1999.

De Gouw, J., M. Bolder, J. Lelieveld, H.A. Scheeren, C. van der Veen, C Warnecke, J. Williams, P.J. Crutzen, H. Fischer, L. Lange, and S. Wong, Overview of the measurements onboard the Citation Aircraft during the Intensive Field Phase of INDOEX, *Submitted to J. Geophys. Res., 2001.*

De Laat, A.T.J., M. Zachariasse, G.J. Roelofs P., van Velthoven, R.R. Dickerson K.P., Rhoads, S.J. Oltmans and J. Lelieveld, Tropospheric O_3 distribution over the Indian Ocean during spring 1995 evaluated with a chemistry-climate model, *J. Geophys. Res., 104*, 13,881-13,893 , 1999.

De Laat, A.T.J., and J. Lelieveld, The diurnal O_3 cycle in the tropical and subtropical marine boundary layer ‚*J. Geophys. Res., 105*, 11547-11559, 2000.

De Laat, A.T.J, R.R. Dickerson, J. Lelieveld, J. Lobert, and G.J. Roelofs, Source analysis of Carbon Monoxide pollution during INDOEX, *submitted to J. Geophys. Res*, 2001a.

De Laat, A.T.J., J. de Gouw, J. Lelieveld, and A. Hansel, Model analysis of pollution impact based on trace gas measurements during INDOEX, *submitted to J. Geophys. Res*, 2001b.

De Roode, S.R., and P.G. Duynkerke, Observed lagrangian transition of stratocumulus into cumulus during ASTEX: mean state and turbulence structure, *J. Atmos. Sci., 54*, 2157-2173, 1997.

Dickerson, R.R., G. J. Huffman, W. T. Luke, L. J. Nunnermacker, K. E. Pickering, A. C. D. Leslie, C. G. Lindsey, W. G. N. Slinn, T. J. Kelly, A. C. Delany, J. P. Greenberg, P. R. Zimmerman, J. F. Boatman, J. D. Ray and D. H. Stedman, Thunderstorms: An Important Mechanism in the Transport of Air Pollutants, Science, 235, 460-465, 1987.

Dickerson, R.R., K.P. Rhoads, T.P. Carsey, S.J. Oltmans and P.J. Crutzen: Ozone in the remote marine boundary layer: A possible role for halogens, *J. Geophys. Res., 104*, 21,385-21,395, 1999.

Dickerson, R.R., Overview: The cruise of the research vessel Ronald H. Brown during the Indian Ocean Experiment (INDOEX) 1999, *Submitted to J. Geophys. Res., 2001.*

Duynkerke, P.G., The stability of cloud top with regard to entrainment: Amandment of the theory of cloud-top entrainment instability, *J. Atmos. Sci, 50*, 495-502, 1993.

Fishman, J, G.L. Gregory, G.W. Sachse, S.M. Beck and G.F. Hill, Vertical profiles of ozone, carbon monoxide and dewpoint temperature obtained during GTE/CITE 1, October-November 1983. *J. Geophys. Res., 92,* 2083-2094, 1987.

Galanter, M., H. Levy II, and G.R. Carmichael, Impacts of biomass burning on tropospheric CO, NO_x and O_3, *J. Geophys. Res., 105*, 6633-6653, 2000.

Ganzeveld, L.N., and J. Lelieveld, Dry deposition parameterization in a chemistry - general circulation model and its influence on the distribution of chemically reactive trace gases, *J. Geophys. Res., 100*, 20,999-21,012, 1995.

Ganzeveld, L.N., and J. Lelieveld and G.J. Roelofs, A dry deposition parameterization for sulfur oxides in a chemistry and general circulation model, *J. Geophys. Res., 103*, 5679-5694, 1998.

Garratt J.R., 1992, The atmospheric boundary layer. Cambridge University Press, 316 pp.

Gery, M., G. Whitten, J. Killus, and M. Dodge, A photochemical kinetics mechanism for urban and regional scale computer modeling, *J. Geophys. Res., 94,* 12,925-12,956, 1989.

Graedel, T.E., and P.J. Crutzen, 1993, Atmospheric Change: an earth system perspective, AT&T, 446 pp

Guenther, A., C.N. Hewitt, D. Erickson, R. Fall, C. Geron, T. Graedel, P. Harley, L. Klinger, M. Lerdau, W.A. McKay, T. Pierce, B. Scholes, R. Steinbrecher, R. Tallamraju, J. Taylor, and P. Zimmerman, A global model of natural volatile organic compound emissions, *J. Geophys. Res., 100,* 8,873-8,892, 1995.

Hamm, S., J. Hahn, G. Helas, and P. Warneck, Acetonitrile in the free troposphere: residence time due to rainout and uptake by the ocean, *Geophys. Res. Lett, 11*, 1207-1210, 1984.

Hao, W.M. and M.H. Liu, Spatial and temporal distribution of tropical biomass burning, *Global Biogeochem. Cycles, 8,* 495-503, 1994.

Haskins, R.D., T.P. Barnett, M.M. Tyree, and E. Roeckner, Comparison of cloud fields from atmospheric general circulation model, in situ and satellite measurements, *J. Geophys. Res., 100,* 1367-1378, 1995.

Hastenrath, S., 1988: Climate and circulation in the tropics, Kluwer Academic Press, 455 pp.

Hense, A., M. Kerschgens and E. Raschke, An economical method for computing radiative transfer in circulation models, *Quart. J. Roy. Meteor. Soc, 108*, 231-242, 1982.

Heikes, B., M. Lee, D. Jacob, R. Talbot, J. Bradshaw, H. Singh, D. Blake, B. Anderson, H. Fuelberg and A.M. Thompson, Ozone, hydroperoxides, oxides of nitrogen, and hydrocarbon budgets in the MBL over the South Atlantic, *J. Geophys. Res., 101*, 24,221-24,234, 1996.

Hoerling, M.P., T.K. Schaack, and A.J. Lenzen, A global analysis of stratospheric-tropospheric exchange during northern winter, *Mon. Wea. Rev., 121*, 162-172, 1993.

Hoke, J.E. and R.A. Anthes, The initialization of numerical models by a dynamic-initialization technique, *Mon. Weather Rev., 104,* 1551-1556, 1976.

Holzinger, R., C. Warneke, A. Hansel, A. Jordan, W. Lindinger, D. Scharffe, G. Schade, and P.J. Crutzen, Biomass Burning as a Source for Formaldehyde, Acetaldehyde, Methanol, Acetone, Acetonitrile and Hydrogen Cyanide, *Geophys. Res, Let., 26,* 1161-1164, 1999.

Houweling, S., F. Dentener, and J. Lelieveld, The impact of nonmethane hydrocarbon compounds on tropospheric photochemistry, *J. Geophys. Res., 103,* 10,673-10,696, 1998.

Hsu, H.H. and B.J. Hoskins, Tidal fluctuations as seen in ECMWF data, *Q. J. R. Meteorol. Soc., 115,* 247-264, 1989.

Intergovernmental Panel on Climate Change (IPCC), *Climate Change,* edited by J.T. Houghton, L.G. Meira Filho, J. Bruce, H. Lee, B.A. Callander, E.Haites, N. Harris, and K. Maskell, Cambridge University Press, Cambridge, 1994.

Jayaraman, A., D. Lubin, S. Ramachandran, V. Ramanathan, E. Woodbridge, W. Collins and K.S. Zalpuri: Direct observations of aerosol radiative forcing over the tropical Indian Ocean during the Jan-Feb 1996 Pre-Indoex cruise, *J. Geophys. Res., 103*, 13827-13836, 1998.

Jeuken, A.B.M., P.C. Siegmund, L.C. Heijboer, J. Feichter and L. Bengtson, On the potential of assimilating meteorological analysis in a climate model for the purpose of model validation, *J. Geophys. Res., 101,* 16939-16950, 1996.

Jha, B., and T.N. Krishnamurty, Real-Time meteorological Atlas during the INDOEX-1999, *FSU Report # 99-09*, Department of Meteorology, Florida State University, 1999.

Johnson, J.E., R.H. Gammon, J. Larsen, T.S. Bates, S.J. Oltmans and J.C. Farmer: ozone in the marine boundary layer over the Pacific and Indian Oceans: Latitudinal gradients and diurnal cycles. *J. Geophys. Res.*, *95*, 11.847-11.856, 1990

Kawa, S.R. and R. Pearson, Ozone budgets from the dynamics and chemistry of marine stratocumulus experiment, *J. Geophys. Res.*, *94*, 9,808-9,817, 1989.

Kley, D., P.J. Crutzen, H.G.J. Smit, H Vömel, S.J. Oltmans, H. Grassl and V. Ramanthan, Observations of near-zero ozone concentrations over the Convective Pacific: effects on air chemistry, *Science, 274,* 230-233, 1996.

Kentarchos, A.S., G.J. Roelofs, and J. Lelieveld, Model study of a stratospheric intrusion event at lower midlatitudes associated with the development of a cutoff low, *J. Geophys. Res., 104,* 1,717-1,727, 1999.

Kentarchos, A.S., G.J. Roelofs, and J. Lelieveld, Simulation of extratropical synoptic scale stratosphere-troposphere exchange using a coupled chemistry-GCM: Sensitivity to horizontal resolution, *J. Atmos. Sci.,* in press, 2000.

Komhyr, W.D., R.A. Barnes, G.B. Brothers, J.A. Lathrop and D.P. Opperman: Electrochemical concentration cell O3sonde performance evaluation during STOIC 1989. *J. Geophys. Res.*, *100*, 9.231-9.244, 1995

Knutson, T.R., and K.M. Weickmann, 20-60 day atmospheric oscillations: compositie life cycles of convection and circulation anomalies, *Mon. Wea. Rev., 115*, 1407-1436, 1987.

Krishnamurty, T.N., H.S.Bedi, W. Heckley and K. Ingles, Reduction of the spinup time for evaporation in a spectral model, *Mon. Wea. Rev., 116,* 907-920, 1988.

Krishnamurty, T.N., J. Xue, K. Ingles and D. Oosterhof, Physical initialization for numerical weather prediction over the tropics, *Tellus, 43 AB,* 53-81, 1991.

Krishnamurti, T.N., B. Jha, P.J. Rasch and V. Ramanathan: A high-resolution global reanalysis highlighting the winter monsoon. *Meteorol. Atmos. Phys*, *64*, 123-171 1997.

Krishnamurti, T.N., B. Jha, J.M. Prospero, A. Jayaraman and V. Ramanathan: Aerosol and pollutant transport over the tropical Indian Ocean during the 1996 northeast monsoon and the impact on radiative forcing,*Tellus, 50B*, 521-542, 1998.

Lal, S. M. Naja and A. Jayaraman: ozone in the marine boundary layer over the tropical Indian Ocean, *J. Geophys. Res, 103*, 18,907-18,917, 1998.

Landgraf, J., and P.J. Crutzen, An efficient method for online calculations of photolysis and heating rates, *J. Atmos. Sci.,55* , 863-878, 1998.

Lawrence, M.G., P.J. Crutzen and P.J. Rasch, *Quart. J. Roy. Meteor. Soc, 125*, 2987-3010, 1999.

Lelieveld, J., and P.J. Crutzen, influences of cloud photochemical processes in tropospheric ozone, *Nature*, *343*, 227-233, 1990.

Lelieveld, J. and P.J. Crutzen, Role of deep cloud convection in the ozone budget of the troposphere, *Science, 264*, 1759-1761, 1994.

Lelieveld, J., and R. van Dorland, ozone chemistry changes in the troposphere and consequent radiative forcing of climate, in *Atmospheric ozone as a climate gas,* edited by W.C. Wang and I.S.A. Isaksen, pp. 227-258, Springer-Verlag, Berlin, 1995.

Lelieveld, J., in *USA-Today*, September 9, 1997.

Lelieveld, J., P.J. Crutzen, M.O. Andreae, T. Campos, G.R. Cass, R.R. Dickerson, H. Fischer, J.A. de Gouw, A. Hansel, A. Jefferson, D. Kley, A.T.J. de Laat, S. Lal, M.G. Lawrence, J.M. Lobert, O. Mayol-Bracero, A.P. Mitra, T. Novakov, S.J. Oltmans, K.A. Prather, V. Ramanathan, T. Reiner, H. Rodhe, H.A. Scheeren, D. Sikka, H.G.J. Smit, J. Williams, and M. Zachariasse, The Indian Ocean Experiment: Widespread air pollution from South and South-East Asia, submitted to *J. Geophys.res*, 2001.

Lenschow, D.H., R. Pearson and B.B. Stankov, Measurements of ozone vertical flux to ocean and forest, *J. Geophys. Res.*, *87*, 8,833-8,837, 1982.

Li, Q., D.J. Jacob, I. Bey, R.M. Yantosca, Y. Zhao, Y. Kondo, and J. Notholt, Atmospheric hydrogen cyanide (HCN): biomass burning source, ocean sink? ,*Geophys. Res. Lett., 27*, 357-360, 2000.

Liu, S.C., M. McFarland, D. Kley, O. Zafiriou and B. Huebert, Tropospheric NO_x and O_3 budgets in the equatorial Pacific, *J. Geophys. Res., 88*, 1,360-1,368, 1983.

Lobert, J.M., D.H. Scharffe, W-M Hao, T. Kuhlbusch, R. Seuwen, P. Warneck, and P.J. Crutzen, in *Global Biomass Burning: Atmospheric, Climatic and Biospheric Implications*, J.S. Levine, Ed. (MIT Press, Cambridge, MA, 1991), p. 289-304,

Lobert, J.M. and J.M. Harris, Trace gases and air mass origin over Kaashidhoo, Indian Ocean, *sumitted to J. Geophys. Res.*, 2000.

Lobert, J.M., B.J. Johnson, S.J. Oltmans, J.M. Harris and S.K. Satheesh, Tropospheric and Column Ozone Over Kaashidhoo, Indian Ocean, During INDOEX 1999, *submitted to Geophys. Res. Lett.*, 2000.

Lobert J.M., V. Ramanathan, J. Prospero, and A. Majeed, Kaashidhoo Climate Observatory (KCO): A new site for observing long-term changes in the tropical Indian Ocean, *Submitted to J. Geophys. Res., 2001.*

Mahapatra, A.K., and C.P. Mitchell, Biofuel consumption, deforestation, and farm level tree growing in rural India, *Biomass and Bioenergy, 17*, 291-303, 1999.

Mandal, T., S.K. Peshin, H.H.J. Smit, R.R. Dickerson, J. Kar, D. Kley, S.K. Srivastava, and A.P. Mitra, Ozonesonde observations over the Indian Ocean and India, *Submitted to J. Geophys. Res., 2001.*

Matthews, A.J., J.M. Slingo, B.J. Hoskins and P.M. Inness, Fast and slow Kelvin waves in the Madden-Julian Oscillation of a GCM, *Q. J. R. Meteorol. Soc., 125*, 1473-1498, 1999.

Martyn, D., 1992: Climates of the world, Elsevier, 435 pp.

McGregor, G.R. and S. Nieuwolt, 1998: Tropical climatology, Wiley and Sons, New York, 339 pp.

Meehl, G.A., The South Asian monsoon and the tropospheric biennial oscillation, *J. Climate, 10*, 1921-1943, 1997.

Monks, S.M., L.J. Carpenter, S.A. Penket, G.P. Ayers, R.W. Gillet, I.E. Galbally and C.P. Meyer, Fundamental ozone photochemistry in the remote MBL: the SOAPEX experiment, measurement and theory, *Atmos. Env., 32*, 3,647-3,664, 1998.

Moorthy, K.K., S.K. Satheesh and D.V. Murthy: Investigations of marine aerosol over the tropical Indian Ocean. *J. Geophys. Res.*, *102*, 18.827-18.842, 1997.

Noone, K.J., R.D. Schillawski, G.L. Kok, C.S. Bretherton and B.J. Huebert, Ozone in the marine atmosphere observed during the Atlantic Stratocumulus Transition Experiment/Marine Aerosol and Gas Exchange, *J. Geophys. Res.*, *101*, 4,485-4,499, 1996.

Olivier, J.G.J. *et al.*, Description of EGAR version 2.0: A set of global emission inventories of greenhouse gases and ozone depleting substances for all anthropogenic and most natural sources on a per country basis on 1°× 1° grid, *RIVM rep. 771060 002/TNO MEP rep. R96/199,* National Institute for Public health and the Environment, Bilthoven, The Netherlands, 1996.

Oltmans, S.J., Surface ozone measurements in clean air, *J. Geophys. Res., 86*, 1,174-1,180, 1981.

Oltmans, S.J. and H. Levy II, Surface ozone measurements from a global network, *Atmos. Env., 28*, 9-24, 1994.

Paluch, I.R., D.H. Lenschow, S. Siems, S. McKeen, G.L. Kok and R.D. Schillawski, Evolution of the subtropical MBL: comparison of sounding over the eastern Pacific from FIRE and HaRP, *J. Atmos. Sci., 51*, 1,465-1,479, 1994.

Paluch, I.R., S. McKeen, D.H. Lenschow, R.D. Schillawski and G.L. Kok, Evolution of the subtropical MBL: photochemical ozone loss, *J. Atmos. Sci.*, 52, 2967-2976, 1995.

Piketh, S.J., H.J. Annegarn and M.A. Kneen: Regional scale impacts of biomass burning emissions over South Africa, Biomass Burning and Global Change, J.S. Levine (ed.), Vol 1, pp. 320-326, MIT Press, Cambridge, Mass., 1996.

Piotrowicz, S.R., D.A. Boran and C.J. Fischer, ozone in the boundary layer of the equatorial Pacific Ocean, *J. Geophys. Res., 91,* 13113-13119, 1986.

Piotrowicz, S.R., R.A. Rasmussen, K.J. Hanson and C.J. Fischer, Ozone in the boundary layer of the equatorial Atlantic Ocean, *Tellus, 41B*, 314-322, 1989.

Piotrowicz, S.R., H.F.Bezdek, G.R. Harvey and M. Springer-Young, On the ozone minimum over the equatorial Pacific Ocean. *J. Geophys. Res., 96,* 18679-18687, 1991.

Price, C. and D. Rind, A simple lightning parameterization for calculating global lightning distributions, *J. Geophys. Res., 97*, 9919-9933, 1992.

Ramage, C.S., 1971: Monsoon Meteorology, Academic press, 296 pp.

Raman, S., D.S. Niyogi, and R. Sadourny, Marine boundary layer and land plume structure over the Indian Ocean during INDOEX, *Submitted to J. Geophys. Res., 2001.*

Rasch, P.J. and D. Williamson, Computational aspects of moisture transport in global models of the atmosphere. *Q. J. R. Meteorol. Soc., 116,* 1071-1090, 1990.

Rhoads, K.P., P. Kelley, R.R. Dickerson, T.P. Carsey, M. Farmer, .L. Savoie and J.M. Prospero, Composition of the troposphere of the Indian Ocean during the monsoonal transition, *J. Geophys. Res., 102,* 18981-18995, 1997.

Rockel, B., E. Raschke and B. Wyres, A parameterization of broad band radiative properties of water, ice and mixed clouds, *Beitr. Phys. Atmosph, 64*, 1-12, 1991.

Roeckner, E., K. Arpe, L. Bengtsson, M. Christoph, M. Claussen, L. Dümenil, M. Esch, M. Giorgetta, U. Schlese, and U. Schulzweida, The atmospheric general circulation model ECHAM-4: Model description and simulation of present-day climate, *Rep. 218*, Max-Planck-Institute for Meteorology, Hamburg. Germany, 1996.

Roeckner, E., T. Siebert, and J. Feichter, Climatic response to anthropogenic sulfate forcing simulated with a general circulation model, In: *Aerosol forcing of climate,* edited by R.J. Charlson and J. Heintzenberg, pp. 349-362, John Wiley and Sons, New York, 1995.

Roelofs, G.J. and J. Lelieveld, Distribution and budget of O_3 in the troposphere calculated with a chemistry - general circulation model, *J. Geophys. Res., 100*, 20,983-20,998, 1995.

Roelofs, G.J. and J. Lelieveld, Model study of the influence of cross-tropopause O_3 transports on tropospheric O_3 levels, *Tellus, 49B*, 38-55, 1997.

Roelofs, G.J., J. Lelieveld, H.G.J. Smit and D. Kley, Ozone production and transports in the tropical Atlantic region during the biomass burning season. *J. Geophys. Res., 102*, 10,637-10,651, 1997a.

Roelofs, G.J., J. Lelieveld and R. van Dorland, A three-dimensional chemistry/general circulation model simulation of anthropogenically derived ozone in the troposphere and its radiative climate forcing, *J. Geophys. Res., 102,* 23,389-23,401, 1997b.

Roelofs, G.J. and J. Lelieveld, Tropospheric ozone simulation with a Chemistry General Circulation model: Influence of Higher Hydrocarbon Chemistry, accepted by *J. Geophys. Res.,* 2000.

Routhier, F, R Dennett, D.D. Davis, A. Wartburg, P. Haagenson and A.C. Delany, Free tropospheric and boundary-layer airborne measurements of ozone over the latitude range of 58°S to 70°N, *J. Geophys. Res., 85,* 7307-7321, 1980.

Sander, R. and P.J. Crutzen, Model study indicating halogen activation and ozone destruction in polluted air masses transported to the sea, *J. Geophys. Res., 101*, 9,121-9,138, 1996.

Savoie, D.L., J.M. Prospero and R.T. Nees: Nitrate, non-sea-salt sulfate and mineral dust over the northwest Indian Ocean. *J. Geophys. Res.*, *91*, 933-942, 1987.

Scheele, M.P., P.C. Siegmund and P.F.J. van Velthoven: Sensitivity of trajectories to data resolution and its dependence on the starting point: in or outside a tropopause fold. *Meteorol. Appl.*, *3*, 267-273, 1996.

Schneider, J., V. Bürger, and F. Arnold, Methyl cyanide and hydrogen cyanide measurements in the lower stratosphere: Implications for methyl cyanide sources and sinks, *J. Geophys. Res., 102,* 25,501-25,506, 1997.

Singh, H.B., D. O'Hara, D. Herlth, W. Sachse, D.R. Blake, J.D. Bradshaw, M. Kanakidou, and P. Crutzen, Acetone in the atmosphere: Distribution, sources and sinks, *J. Geophys. Res., 99,* 1805-1819, 1994.

Singh, H.B., M. Kanakidou, P.J. Crutzen, and D.J. Jacob, High mixing ratios and photochemical fate of oxygenated hydrocarbons in the global troposphere, *Nature, 387,* 50-54, 1995.

Singh,H.B., G.L. Gregory, B. Anderson, E. Browell, G.W. Sachse, D.D. Davis, J. Crawford, J.D. Bradshaw, R. Talbot, D.R. Blake, D. Thornton, R. Newell and J. Merill, Low O3 in the marine boundary layer of the tropical Pacific Ocean: Photochemical loss, chlorine atoms and entrainment, *J. Geophys. Res., 101,* 1907-1917, 1996.

Singh, H.B., Y. Chen, A. Tabazadeh. Y. Fukui, I. Bey, R. Yanosca, D. Jacob, F. Arnold, K. Wohlform, E. Atlas, F. Flocke, D. Blake, N. Blake, B. Heikes, J. Snow, R. Talbot, G. Gregory, G. Sachse, S. Vay, and Y. Kondo, Distribution and fate of selected oxygenated organic species in the troposphere and lower stratosphere over the Atlantic, *J. Geophys. Res., 105*, 3795-3805, 2000

Sinha, C.S., S. Sinha, and V. Josh, Energy use in the rural areas of India: setting up a rural energy database, *Biomass and Bioenergy, 14*, 489-503, 1998.

Slingo, J.M., K.R. Sperber, J.S. Boyle, J-P. Ceron, M. Dix, B. Dugas, W. Ebisuzaki, J. Fyfe, D. Gregory, J-F. Gueremy, J. Hack, A. Harzallah, P. Inness, A. Kitoh, W.K-M. Lau, B. McAveney, R. Madden, A. Matthews, T.N. Palmer, C-K. Park, D. Randall and N. Renno, Intraseasonal oscillations in 15 atmospheric general circulation models: results from an AMIP diagnostic subproject, *Clim. Dyn., 12*, 325-357, 1996.

Smit, H.J., D. Kley, R. Cremer, and M. Zachariasse, Large scale distribution of O_3 and Humidity over the Indian Ocean between 15°N and 15°S during INDOXE: Evidence for large scale outflow of Indian pollution, *Submitted to J. Geophys. Res., 2001.*

Smith, K.R., R. Uma, V.V. Kishore, J. Zhang, V. Joshi and M. Khalil, Greenhouse Implications of Household Stoves, *Annu. Rev. Energy. Enrivon., 25*, 2000.

Stehr, J.W., W.P. Ball, R.R. Dickerson, B.G. Doddridge, C. Piety and J.E. Johnson, Latitudinal gradients in O_3 and CO during INDOEX 1999, *Submitted to J. Geophys. Res., 2001.*

Streets, D.G., and S.T. Waldhoff, Greenhouse-gas emissions from biofuel combustion in Asia, *Energy, 24*, 841-855, 1999.

Thompson, A.M. and D.H. Lenschow, Mean profiles of trace reactive species in the unpolluted marine surface layer, *J. Geophys. Res.*, *89*, 4,788-4,796, 1984.

Thompson, A.M., J.E. Johnson, A.L. Torres, T.S. Bates, K.C. Kelly, E. Atlas, J.P. Greenberg, N.M. Donahue, S.A. Yvon, E.S.Saltzman, B.G. Heikes, B.W. Mosher, A.A. Shashkov and V.I. Yegorov, Ozone observations and a model of MBL photochemistry during SAGA 3, *J. Geophys. Res., 98*, 16,955-16,968, 1993.

Tiedtke, M., A comprehensive mass flux scheme for cumulus parameterization in large-scale models, *Mon. Wea. Rev., 117,* 1779-1800, 1989.

Tuck, A.F., D. Baumgardner, K.R. Chan, J.E. Dye, J.W. Elkins, S.J. Hovde, K.K. Kelly, m. Loewenstein, J.J. Margitan, R.D. May, J.R. Podolske, M.H. Proffitt, K.H. Rosenlof, W.L. Smith, C.R. Webster, and J.C. Wilson, The Brewer-Dobson circulation in the light of high altitude *in situ* aircraft observations, *Q. J. R. Meteorol. Soc, 123*, 1-69, 1997.

Tyson, P.D., M. Garstang, R.J. Swap, E.V. Browell, R.D.Diab and A.M. Thompson: Transport and vertical structure of ozone and aerosol distributions over southern Africa, Biomass Burning and Global Change, J.S. Levine (ed.), Vol 1, pp. 403-421, MIT Press, Cambridge, Mass., 1996.

Tyson, P.D., M. Garstang, A.M. Thompson, P.D. Abreton, R.D. Diab and E.V. Browell: Atmospheric transport and photochemistry of ozone over south central southern africa during SAFARI, *J. Geophys. Res., 102,* 10,623-10,635, 1997.

Verver, G.H.L., D.R. Sikka, J.M. Lobert, G. Stossmeister and M. Zachariasse, Overview of the meteorological conditions and atmospheric transport processes during INDOEX 1999, *Submitted to J. Geophys. Res., 2001.*

Vilà-Guerau de Arellano, J. and P.G. Duynkerke, Exchange of chemical species between the atmospheric boundary layer and the reservoir layer: an analytical interpretation, *Bound. Met., 59.* 219-227, 1998.

Vogt, R., P.J. Crutzen and R. Sander: A mechanism for halogen release from sea-salt aerosol in the remote marine boundary layer. *Nature*, *383*, 327-329, 1996

Vreugdenhil, C.B., Computational hydraulics : an introduction. Springer Verlag, 1989, 182 pp.

Wang, Y., D.J. Jacob, and J.A. Logan, Global simulation of tropospheric O_3-NO_x - hydrocarbon chemistry. 1. Model formulation, *J. Geophys. Res., 103*, 10713-10725, 1998.

Webster, P. J., A. Moore, J. Loschnigg and M. Leban: Coupled ocean-atmopshere dynamics in the Indian Ocean during 1997-98, *Nature, 40*, 23 September, 356-360, 1999.

Webster, P. J., T. Palmer, M. Yanai, R. Tomas, V. Magana, J. Shukla and A. Yasunari: Monsoons: Processes, Predictability and the prospects for prediction, *J. Geophys. Res., 103*, 14,451-14,510, 1998.

Wesely, M.L., Parameterization of surface resistances to gaseous dry deposition in regional-scale numerical models, *Atmos. Environ., 23*, 1293-1304, 1989.

Williams, J., H. Fischer, S. Wong, R. Scheele, B. Scheeren and J. Lelieveld, Vertical profiles of CO and O_3 and relative humidity North and South of the ITCZ over the Indian Ocean during the winter monsoon: evidence of two mechanisms for the influx of O_3 rich air to the tropical upper troposphere and of interhemispheric exchange, *Submitted to J. Geophys. Res., 2001.*

Wisthaler, A., A. Hansel, R. Dickerson, and P.J. Crutzen, Organic trace gas measurements by PTR-MS during INDOEX 1999, *Submitted to J. Geophys. Res., 2001.*

WMO, Tropospheric OH: measurements, modeling, oxidizing capacity, in WMO Global Ozone Research and Monitoring Project, Report No 44 Scientific: Assessment of Ozone Depletion: 1998, 8.25-8.27.

Zachariasse, M., P.F.J. van Velthoven, H.G.J. Smit, J. Lelieveld, T.K. Mandal, and H. Kelder, Influence of stratosphere-troposphere exchange on tropospheric ozone over the tropical Indian Ocean during the winter monsoon, Accepted in *J. Geophys. Res.,* 2000.

Zhou, X. and K. Mopper, Photochemical production of low-molecular-weight carbonyl compounds in seawater and surface microlayer and their air-sea exchange, *Marine Chemistry, 56,* 201-213, 1997.

Yienger, J. J. and H. Levy II, Empirical model of global soil-biogenic NO_x emissions, *J. Geophys. Res., 100,* 11,447-11,464, 1995.

Samenvatting

Een belangrijk thema in het huidige klimaatonderzoek is het effect van luchtverontreiniging op het klimaat. In de afgelopen decennia is duidelijk geworden dat "de mens" in toenemende mate bezig is de atmosfeersamenstelling te veranderen (bv. zure regen, het gat in de ozonlaag). Deze veranderingen kunnen leiden tot klimaatveranderingen zoals bv. verschuivingen van klimaatzones, veranderingen in neerslagpatronen en een stijging van de zeespiegel als gevolg van het afsmelten van ijskappen. De veranderingen in de atmosfeersamenstelling wordt veroorzaakt door een toename van broeikasgassen maar ook door een toename van kleine deeltjes (aërosolen) in de atmosfeer. De toename van broeikasgassen leidt tot een stijging van de temperatuur. De toename van aërosolen leidt tot een daling van de temperatuur omdat ze kortgolvige straling (zonlicht) reflecteren. Daarnaast dienen aërosolen ook als condensatiekernen voor wolkendruppels. Een verandering in de hoeveelheid en het type aërosolen leidt tot een verandering van de stralingseigenschappen van wolken en indirect ook tot temperatuur- en klimaatveranderingen.

De brongebieden van luchtverontreiniging zijn echter niet uniform over de aarde verdeeld. De belangrijkste emissies vinden plaats op het noordelijk halfrond in de ontwikkelde westerse landen (Noord Amerika, Europa en oost Azie), maar in toenemende mate ook in ontwikkelingslanden. Het zuidelijk halfrond daarintegen is nog relatief schoon. Er bestaan grote lokale en regionale verschillen in emissies die grote lokale en regionale verschillen veroorzaken in de verandering van de atmosfeersamenstelling. De onderkenning van het broeikaseffect heeft inmiddels geleid tot emissiereducties in westerse landen. In de derde wereld en de zich ontwikkelende landen bestaat echter nog maar weinig aandacht voor dit probleem. Omdat deze landen dicht bij het zuidelijk halfrond liggen vormen deze potentieel een belangrijke bron van verontreiniging van het zuidelijk halfrond. Een gebied met grote emissies vormt India en zuidoost Azie. Het niveau van luchtverontreiniging in dit gebied is op het moment al ongeveer even hoog als in de westerse landen. De toename van de bevolking en de welvaart in India en zuidoost Azie zal in de komende jaren leiden tot een verdere toename van emissies. Hoe de verontreiniging vanuit India en zuidoost Azie zich globaal verspreidt en hoe het klimaat erdoor beinvloed wordt is echter nog onzeker.

Om een aantal van deze processen beter te begrijpen en een aantal onzekerheden weg te nemen werd beginjaren '90 de meetcampagne INDOEX (**IND**ische **O**ceaan **EX**periment) opgezet. INDOEX vond plaats te laten gedurende de wintermoesson (november-mei). De noordrand van de Indische Oceaan wordt begrensd door de landmassa's van India en Zuidoost Azië waar veel emissies plaatsvinden. Gedurende de wintermoessonperiod zorge hogedrukgebieden boven Azië voor een aflandige wind aan het aardoppervlak die de luchtverontreiniging vanuit India en Zuidoost Azië naar de Indische Oceaan transporteren. Tegelijkertijd zorgen de hogedrukgebieden voor dalende luchtbewegingen in de atmosfeer. Dalende luchtmassa's warmen op en drogen uit. De luchtlagen die in direct contact met het aardoppervlak staan (de grenslaag) blijven echter relatief koud en vochtig. Omdat warme, droge lucht lichter is dan koude, vochtige lucht, zal de warme lucht als een "deken" op de grenslaag blijven liggen. In zo'n situatie is er weinig uitwisseling tussen de grenslaag de atmosfeer erboven. Door de dalende luchtbewegingen wordt de vorming van diepe convectie (buien) onderdrukt. De

luchtmassa's in de grenslaag worden ongestoord over de oceaan getransporteerd. Omdat neerslag een belangrijk verwijderingsmechanisme van luchtverontreiniging is, en de oceaan slechts een kleine bron van verontreiniging is, worden de veronreinigde luchtmassa's tot diep in de zuidelijke Indische Oceaan getransporteerd. Uiteindelijk bereiken luchtmassa's de InterTropische Convergentie Zone (ITCZ), een gebied met diepe convectie en veel neerslag die de scheiding vormt tussen de luchtmassa's van het noordelijk en het zuidelijk halfrond. De continentale luchtmassa's die vanaf het Aziatische continent de oceaan op getransporteerd worden zijn erg droog. Naarmate ze een langere weg over zee afgelegd hebben neemt de vochtigheid toe en kunnen er wolken gevormd worden. De aanwezige luchtverontreiniging verandert de wolkeneigenschappen. Ten zuiden van de ITCZ doet zich een soortgelijke situatie voor, zij het dat de luchtmassa's op het zuidelijk halfrond veel schoner zijn. Uit de verschillen in wolkeneigenschappen tussen het noordelijk en het zuidelijk halfrond kan worden afgeleidt hoe de wolkeneigeschappen veranderen ten gevolge van luchtverontreiniging.

Een bijkomend voordeel van INDOEX is het meer kennis genereert over the wintermoesson in het INDOEX-gebied. De Indiase zomermoesson is een goed gedocumenteerd en veel bestudeerd fenomeen, in tegenstelling tot de wintermoesson. De wintermoesson is het droge seizoen in India. Voor de Indiërs en de Indiase economie is het veel belangrijker te weten hoeveel neerslag er tijdens de zomermoesson valt dan wat er gebeurt in de droge winter.

Het atmosfeeronderzoek maakt tegenwoordig veel gebruik van numerieke globale chemie-circulatie modellen (GCM), onder andere voor het bestuderen van atmosfeerprocessen en mogelijke toekomstscenarios. Hoe goed deze modellen in staat zijn het huidige klimaat te simuleren bepaald mede de waarde van modelstudies. De validatie van de modellen wordt gedaan door observaties het model te vergelijken. Et blijkt echter niet zo eenvoudig te zijn waarnemingen met modelresultaten te vergelijken. De atmosfeer is een chaotische systeem, hetgeen wil zeggen dat de ontwikkeling van de (model-) atmosfeer in de loop van de tijd sterk afhankelijk is van de begincondities. De begincondities zijn niet exact bekend. Er zijn grote gebieden op aarde waar maar zeer weinig waarnemingen gedaan worden. Bovendien hebben waarnemingen meetfouten die eveneens tot onzekerheden leiden. Ook de modelbeschrijving van atmosferische fysica en chemie niet perfect. Omwille van beperkte computerrekentijd en opslagruimte worden een aantal atmosferische processen in het model op sterk vereenvoudigde wijze gerepresenteerd. In een modelsimulatie zullen de begincondities afwijken ten opzichte van de "echte" atmosfeer. De afwijkingen, in combinatie met de onvolledige beschrijving van sommige atmosfeerprocessen, leiden tot een model-atmosfeer die op termijn afwijkt van de echte ontwikkeling van de atmosfeer. Dit proces is er mede verantwoordelijk voor dat het weer langer dan 1 tot 2 weken vooruit moeilijk te voorspellen valt. Dit betekent echter niet dat de gesimuleerde atmosfeerontwikkeling onjuist is. De grote afhankelijk van de begincondities zorgt ook voor dat in de "echte" atmosfeer nooit twee keer dezelfde situatie optreedt. De model-atmosfeer is een andere, min of meer reële oplossing van het systeem. Deze eigenschappen van de atmosfeer bemoeilijken het direct vergelijken van observaties met GCM-resultaten.

Om het model toch te evalueren kunnen andere, indirecte methoden gebruikt worden. Een mogelijkheid is gemiddelden van meetreeksen te vergelijken met gemodeleerde

gemiddelden. Zo'n vergelijking geeft aan of het model in staat is de gemiddelde toestand van het klimaat te simuleren, ervan uitgaande dat er zoiets als een gemiddelde atmosfeer bestaat. Helaas zijn er op het moment maar weinig van dit soort reeksen beschikbaar. Bovendien is de atmosfeer gemiddeld nooit precies hetzelfde is, zelfs van jaar tot jaar. Door het middelen van de observaties gaat ook nog eens informatie over de kortere tijdschalen verloren.

Een andere mogelijkheid is om specifieke processen die door het model gesimuleerd worden (denk bijvoorbeeld de ontwikkeling van een tropische cycloon) te vergelijken met waarnemingen van hetzelfde proces. Op deze wijze kan bestudeerd worden of een proces op de juiste wijze door het model gesimuleerd wordt. Ook op deze wijze is een directe vergelijking tussen het model en de waarnemingen niet mogelijk.

Om het probleem van de modelevaluatie op te lossen is een techniek ontwikkeld waarbij de het model aangestuurd wordt met behulp van analyses van het daadwerkelijk opgetreden weer. De weeranalyse wordt gemaakt met behulp van veel waarnemingen en kan ook dienen als beginsituatie van een weersvoorspelling. Het aansturen van een GCM zorgt ervoor dat het model het waargenomen weer blijft volgen. In dat geval is het mogelijk de chemische samenstelling van de atmosfeer op het moment van een waarneming te simuleren. Deze techniek is veelvuldig gebruikt bij het onderzoek dat heeft geleid tot dit proefschrift.

In hoofdstuk 1 van dit proefschrift wordt een inleiding gegeven over INDOEX (paragraaf 1.1), de wintermoesson circulatie (paragraaf 1.2), en de specifieke atmosferische chemie in het INDOEX gebied (paragraaf 1.3). Paragraaf 1.4 behandeld het globale chemie-circulatie model **ECHAM** (**E**uropees **C**entrum **HA**mburg **M**odel). In paragraaf 1.5 wordt de techniek waarmee de weeranalyses het model aansturen uitgelegd (ook wel "nudging" of "newtoniaanse relaxatie" genoemd) en tot slot volgen in paragraaf 1.6 de belangrijkste onderzoeksvragen die ten grondslag liggen aan dit proefschrift.

In hoofdstuk 2 wordt een vergelijking gemaakt tussen metingen gedaan tijdens de eerste pre-INDOEX cruise in 1995 aan boord van het Amerikaanse onderzoeksschip de "Malcolm Baldrige" en het ECHAM model. Dit schip voer in maart en april 1995 van Durban, Zuid Afrika naar Colombo, Sri Lanka. Gedurende deze reis zijn o.a. ballonsonde-metingen gedaan van O_3, oppervlakte metingen van O_3, CO, NO_x, windsnelheid en oppervlaktedruk. De vergelijking van het model met de metingen van zowel O_3, CO als de oppervlaktedruk toont aan dat het model goed in staat is om de deze metingen te simuleren. De modelanalyse de metingen laat zien dat de luchtmassa's in grenslaag boven de oostelijke Indische Oceaan betrekkelijk schoon zijn, maar dat de vrije troposfeer de sterk beïnvloedt wordt door emissies ten gevolge van grootschalige (bos-) branden in centraal Afrika. In de nabijheid van India worden ook de luchtmassa's in de grenslaag meer verontreinigd, hoewel met name de O_3 concentraties laag blijven. In de bovenste troposfeer werden dunne lagen met zeer lage O_3 concentraties gemeten. Deze lagen worden ook door het model gesimuleerd, ondanks het feit dat de lagen nauwelijks dikker zijn dan de verticale resolutie van het model. De modelanalyse laat zien dat verticaal transport van O_3-arme grenslaaglucht door tropische cyclonen verantwoordelijk is voor deze lagen.

In hoofdstuk 3 wordt gekeken naar de dagelijkse gang van O_3 in de marine grenslaag. Uit metingen van het klimaat observatorium Kaashidhoo op de Malediven, gedaan in

Februari en Maart 1998, bleek dat de dagelijkse gang een zeer specifiek verloop had. Gedurende de dag nam de O_3 concentratie af, terwijl 's nachts de O_3 concentratie weer opliep. Deze dagelijkse gang in O_3 wordt overigens op vrijwel alle marine meetstations waargenomen. De bestaande verklaring voor dit fenomeen was dat gedurende de dag O_3 onder invloed van licht wordt afgebroken, en 's nachts weer wordt aangevuld door verticaal transport van O_3-rijke lucht uit de vrije troposfeer. Het model blijkt deze typische dagelijkse gang ook de simuleren. Dit is opmerkelijk, aangezien het verticale transport van O_3 niet in het model zit. Dit is een belangrijke aanwijzing dat de huidige verklaring niet correct is. Vervolgens wordt aangetoond dat de bestaande verklaring ook als principe niet juist kan zijn. Een nieuwe verklaring wordt geformuleerd, waarin de nachtelijke toename het gevolg is van de advectie van een horizontale O_3 gradiënt in de marine grenslaag. Overdag zorgt de photodissociatie van O_3 voor een afname van O_3 concentraties. 's Nachts, wanneer er geen O_3 afbraak is vanwege het ontbreken van zonlicht, neemt O_3 weer toe als gevolg van de O_3 gradiënt en transport. Ook werd aangetoond dat de horizontale O_3 gradiënt weer een direct gevolg is van de O_3 afbraak gedurende de dag. Vervolgens wordt aangetoond dat dit ook de manier is waarop de dagelijkse gang in O_3 in het model wordt gesimuleerd, en tot slot wordt er uitgelegd dat deze verklaring beter in staat is om een aantal O_3 waarnemingen te verklaren dan de "oude" verklaring.

In hoofdstuk 4 worden CO metingen gedaan tijdens de IFP vergeleken met modelresultaten. Uit de vergelijking blijkt dat het model goed in staat is de gemeten variaties van CO concentraties te simuleren. Op kleine tijd- en ruimteschalen bestaan er met name op lage modelresolutie verschillen tussen de gemeten en gemodeleerde CO concentraties. De deze verschillen worden kleiner bij een hogere horizontale modelresolutie. Voor een specifiek gebied in het INDOEX-gebied is het model niet in staat de metingen te reproduceren, en verslechterd de modelsimulatie zelfs op hogere resolutie. Dit gebied ligt in de directe invloedsfeer van het zuiden en zuidwesten van India. In de modelsimulatie zijn de luchtmassa's in dit gebied direct afkomstig vanuit zuid en zuidwest India. Een mogelijke verklaring van de verschillen tussen de gemodeleerde en gemeten CO concentraties in dit gebied is de zeewindcirculatie die aanwezig aan de Indiase kusten. De zeewindcirculatie heeft een belangrijke invloed op de lokale circulatie en het transport van luchtvervuiling, maar is te kleinschalig om door het model gesimuleerd te worden. De zeewindcirculatie "tilt" de verontreinigde continental Indiase luchtmassa's op en transporteerd ze tot boven de marine grenslaag. Omdat het model de zeewindcirculatie niet kan simuleren, worden in het model de luchtmassa's rechtstreeks in de marine grenslaag getransporteerd.

De modelsimulatie toont aan dat biomassaverbranding in India de belangrijkste bron van CO in het INDOEX-gebied is. Globaal gezien zijn, naast biomass verbranding, ook natuurlijke CO-emissies, CO-productie als gevolg van de afbraak van koolwaterstoffen en emissies als gevolg van menselijke activiteit belangrijke CO-bronnen. Het INDOEX-gebied wijkt sterk af van dit globale beeld. Tevens blijkt dat, globaal gezien, het grootste gedeelte van CO in de vrije troposfeer afkomstig is van de afbraak van hogere koolwaterstoffen, ook boven de Indische Oceaan.

In hoofdstuk 5 worden metingen van koolwaterstoffen (met name aceton (CH_3COCH_3) en acetonitriel (CH_3CN) gedaan tijdens de IFP vergeleken met modelsimulaties. Aceton en acetonitriel komen in relatief hoge concentraties voor in de

grenslaag boven de noordelijke Indische Oceaan. Aceton komt vrij bij biomassaverbranding en als gevolg van de atmosferische afbraak van hogere koolwaterstoffen. Het wordt ook door planten geëmitteerd en komt, in mindere mate, ook vrij bij het gebruik van fossiele brandstoffen. Acetonitriel komt vrijwel alleen bij verbranding van biomassa vrij, en vormt een uitstekende indicator voor luchtverontreiniging afkomstig van biomassaverbranding.

Het model blijkt redelijk in staat de aceton metingen te simuleren. Het dient opgemerkt te worden dat het grootste gedeelte van de metingen gedaan werden in het gebied rondom de Malediven, waarvan in hoofdstuk 4 al was aangetoond dat het model niet goed instaat was om de metingen gedaan in dit gebied te simuleren. Echter, de gemodelleerde en gemeten CO-aceton relatie komt voor verontreinigde luchtmassa's goed overeen. Dit toont aan dat de productie en destructie van CO en aceton op juiste wijze gerepresenteerd zijn in het model. Het bevestigd dat de verschillen tussen model en metingen in het gebied rondom de Malediven veroorzaakt worden door andere processen (lees: zeewindcirculatie) dan atmosferische chemie. Voor lage CO concentraties is de aceton concentratie vrijwel constant, wat niet door het model gesimuleerd wordt. Een mogelijke verklaring is een oceanische bron van aceton, die niet in de model simulatie aanwezig was. Een modelsimulatie met een oceanische bron leidt tot een constante aceton concentratie voor lage CO concentraties. Volgens de modelsimulatie kan deze bron een bijdrage leveren van 25 tot 50 % aan de bekende aceton bronnen.

Het model blijkt niet goed in staat te zijn om gemeten acetonitriel concentraties en de CO-acetonitriel relatie te simuleren. Een mogelijke verklaring is verwijdering van acetonitriel uit de atmosfeer door opname in zeewater, hetgeen niet in het model was opgenomen. Hoewel acetonitriel matig oplosbaar is in water, kan dit proces toch een belangrijke bijdrage leveren aan de verwijdering van acetonitriel omdat andere atmosferische verwijderingsprocessen zeer traag verlopen. Een modelsimulatie met opname van acetonitriel in het zeewater leidt tot een betere vergelijking tussen gemeten en gemodelleerde CO-acetonitriel relatie.

In de vrije troposfeer zijn gemodeleerde acetonitriel concentraties hoger dan gemeten. Mogelijk speelt uitwisseling van luchtmassa's tussen de stratosfeer en troposfeer hier een rol. Acetonitriel wordt in de stratosfeer relatief snel afgebroken door reacties met het OH radicaal. Acetonitriel concentraties in de stratosfeer zijn daardoor lager dan in de troposfeer. Transport van stratosferische luchtmassa's naar de troposfeer kan leiden tot een verlaging van de troposferische acetontriel-concentraties. Omdat stratosferische afbraak van acetonitriel niet in het model aanwezig was, zijn de gemodelleerde acetonitriel concentraties in de vrije troposfeer te hoog.

Tot slot worden metingen van hogere koolwaterstoffen met modelresultaten vergeleken. Hoewel het aantal metingen beperkt was, blijkt dat het model grofweg in staat is de gemeten concentraties te reproduceren. Dit geeft enig vertrouwen in de emissie-scenario's die gebruikt werden in deze model studie.

In hoofdstuk 6 wordt gekeken naar de gemodelleerde oppervlakte CO-concentraties in de INDOEX regio gedurende een aantal verschillende maanden en jaren (Februari en Maart, van 1996 tot en met 1999). Uit vele waarnemingen bleek dat de hoeveelheid luchtverontreiniging in Februari en Maart 1999 veel hoger was dan in 1998. Dit blijkt ook door het model gesimuleerd te worden. Uit literatuur is bekend dat op de tijdschaal van maanden drie processen een rol spelen in de wintermoesson-circulatie. Om te

beginnen is er de normale jaarlijkse gang, die bepaald wordt door de sterkte van de zonnestraling. Daarnaast blijkt El Niño, indien actief, een grote invloed te hebben op het circulatiepatroon tijdens de wintermoesson. Het derde proces dat mede bepalend is voor de variaties in de wintermoessoncirculatie is de Madden-Julian oscillatie (MJO). De MJO bestaat voornamelijk uit afwisselend sterke en zwakke convectie in de ITCZ op een tijdschaal van 30-60 dagen. Uit de modelanalyse blijkt dat met deze drie processen het grootste gedeelte van de waargenomen variabiliteit verklaard kon worden.

In hoofdstuk 7 tot slot volgt een samenvatting en een kort discussie.

Dankwoord

Hoewel alleen mijn naam op de omslag van dit proefschrift prijkt, zijn vele mensen bij de tot standkoming van dit werk betrokken die ik niet onvermeld wil laten.

Als eerste wil ik een aantal naaste collegae van het IMAU bedanken. Om te beginnen GeertJan Roelofs, mijn steun en toeverlaat als het ging om het gebruik van ECHAM en de supercomputer in Amsterdam. Ook Ad (2x), Arthur, Bram, Bert, Frank, Laurens, Maarten, Miranda, Richard, Sander, Swen, Tasos en Wouter hebben hun duit in het zakje gedaan. Een speciaal bedankje is er ook voor Joost en Carsten, wier INDOEX meetdata ik in hoofdstuk 5 gebruikt heb.

Mentioning INDOEX, I also have to thank the entire INDOEX community, but a few members in particular. Prof. Dr. Russ Dickerson of Maryland University and his co-workers, for making a number of measurements available for me to use in a number of articles. I also have to thank him for letting me publish my second article (Chapter 3), even though the data that I used for a publications were actually not (yet) for use at that point in time. I also thank Armin Hansel of Innsbruck University and co-workers, for letting me use their data in Chapter 5. Also, I want to thank the MPI-Mainz people involved in INDOEX (Horst, Johnathan, Lutz, Marianne, Paul, Radek and Stephanie). Also Mark Lawrence from the MPI-Mainz, my INDOEX co-modeller whom I very much enjoyed discussing the matters of global atmospheric chemistry modelling with.

In het kader van INDOEX moet ik ook Mijke Zachariasse bedanken, de enige van mijn co-auteuren die, hoewel alle co-auteurs een belangrijke bijdrage hebben geleverd aan de respectievelijke artikelen, de enige is die een compleet onderdeel van een artikel heeft verzorgd (paragraaf 4.2 van hoofdstuk 2).

I also want to thank Nick Smith for making my during the summerschool in Grenoble, France, in Januari and Februari 1997 so enjoyable.

Tot slot wil ik mijn promotor en directe begeleider Jos Lelieveld bedanken. Omdat mijn promotieonderzoek erg vlotjes verliep, zag ik Jos vooral op momenten dat ik weer iets nieuws gevonden of bedacht had. Hij was meestal enthousiast (soms zelfs heel erg) over mijn laatste ontdekking of visualisatie, en altijd bereid daarover van gedachten te wisselen. Bovendie had hij altijd wel ideeen en suggesties over wat we er nog meer mee konden doen. Even belangrijk was de vrijheid die hij mij gunde zelf ideeen te ontwikkelen en uit te werken (zie bijvoorbeeld hoofdstuk 3) en mij de kans te geven mijn eigen richting te zoeken (of mij in ieder geval het idee te geven ik dat deed), iets wat ik altijd als erg prettig heb ervaren. Bovendien diende hij als "lopende bibliotheek" om mijn eigen kennis over atmosferische chemie bij te spijkeren, omdat ik van huis uit nu eenmaal geen chemicus ben, en voor artikelen over de meest uiteenlopende onderwerpen. Het enige nadeel aan zijn begeleiding was dat we beiden dezelfde voornaam dragen, hetgeen af en toe wel eens tot wat verwarring leidde. Dat was ook de reden om mijn e-mails naar buitenlandse collegae te ondertekenen met Jos^2, hoewel me dat wel de opmerking opleverde dat het me nu wel heel hoog in de bol was geslagen, om mezelf in meervoudsvorm aan te duiden.

Jos, bedankt.

Curriculum Vitae

Ik ben geboren op 26 Juli 1973 te 's-Hertogenbosch, en ik ben opgegroeid op in het plaatsje Den Dungen onder de rook van 's-Hertogenbosch. In 1991 behaalde ik het VWO diploma aan het Sint Jans Lyceum te 's-Hertogenbosch, en besloot de studie meteorologie en fysische oceanografie te gaan volgen aan de Universiteit Utrecht, toentertijd een bovenbouwstudie van de studierichting Natuur & Sterrenkunde. Deze studie wist ik succesvol af te ronden in Augustus 1996. In die zomer beraadde ik mij over mijn toekomstmogelijkheden. Hoewel ik tijdens mijn studie nooit erg geïnteresseerd was in een carrière als promovendus (onderbetaald, ondergewaardeerd etcetera), deed zich die zomer de mogelijkheid voor om een promotieonderzoek te gaan doen bij Prof. Dr. Jos Lelieveld, toentertijd net aangesteld in Utrecht als nieuwe hoogleraar atmosferische chemie. Al snel kwam ik tot de conclusie dat dit vakgebied me intrigeerde, omdat het op dat moment met de Nobelprijs voor Paul Crutzen volop in de belangstelling stond, terwijl er tijdens de studie relatief weinig aandacht aan werd besteed. Omdat je een gegeven paard niet in de bek moet kijken, en omdat ik meer over het onderwerp wilde weten, begon ik half oktober 1996 met mijn promotieonderzoek. Het centrale thema van mijn onderzoek was het INDische Oceaan Experiment (INDOEX). Een belangrijk deel van mijn onderzoek betrof het analyseren en vergelijken van zowel metingen als resultaten van een globaal chemie-klimaat model. Tijdens mijn promotie heb ik o.a. een summerschool gevolgd in het Franse Grenoble in Januari en Februari 1997, en heb tijdens de belangrijkste fase van INDOEX in Februari en Maart 1999 een maand doorgebracht in de Indische Oceaan op de Malediven. Het eindresultaat van dit onderzoek ligt voor u.